Ultrafast Pulsed-Laser Applications for Semiconductor Thin Film Deposition and Graphite Photoexfoliation

by

Ibrahim Malek Oraiqat

A dissertation submitted in partial fulfillment
of the requirements for the degree of
Doctor of Philosophy
(Applied Physics)
in the University of Michigan
2016

Doctoral Committee:

Professor Roy Clarke, Chair
Professor Cagliyan Kurdak
Associate Professor Vanessa Sih
Professor Katsuyo S Thornton

To Roy Clarke,
for the opportunity,
for his mentorship, and for his patience

TABLE OF CONTENTS

LIST OF FIGURES

LIST OF TABLES

ABSTRACT

This thesis focuses on the application of ultrafast lasers in nanomaterial synthesis. Two techniques are investigated: Ultrafast Pulsed Laser Deposition (UFPLD) of semiconductor nanoparticle thin films and ultrafast laser scanning for the photoexfoliation of graphite to synthesize graphene. The importance of the work is its demonstration that the process of making nanoparticles with ultrafast lasers is extremely versatile and can be applied to practically any material and substrate. Moreover, the process is scalable to large areas: by scanning the laser with appropriate optics it is possible to coat square meters of materials (e.g., battery electrodes) quickly and inexpensively with nanoparticles. With UFPLD we have shown there is a nanoparticle size dependence on the laser fluence and the optical emission spectrum of the plume can be used to determine a fluence that favors smaller nanoparticles, in the range of 10-20 nm diameter and 3-5 nm in height. We have also demonstrated there are two structural types of particles: amorphous and crystalline, as verified with XRD and Raman spectroscopy. When deposited as a coating, the nanoparticles can behave as a quasi-continuous thin film with very promising carrier mobilities, 5-52 cm^2/Vs, substantially higher than for other spray-coated thin film technologies and orders of magnitude larger than those of colloidal quantum dot (QD) films.

Scanning an ultrafast laser over the surface of graphite was shown to produce both filamentary structures and sheets which are semi-transparent to the secondary-electron beam in SEM. These sheets resemble layers of graphene produced by exfoliation. An ultrafast laser "printing" configuration was also identified by coating a thin, transparent substrate with graphite

particles and irradiating the back of the film for a forward transfer of material onto a receiving substrate. A promising application of laser-irradiated graphene coatings was investigated, namely to improve the charge acceptance of lead-acid battery electrodes. We demonstrated improvements of 63 % in the cycle lifetime and 23 % in the electrode charging conductance.

CHAPTER 1

Introduction

With the advent of the ultrafast laser, new ways of materials processing have been discovered. This thesis will focus on the application of ultrafast lasers in nanomaterial synthesis. Two techniques are investigated: Ultrafast Pulsed Laser Deposition (UFPLD) of semiconductor nanoparticle thin films and ultrafast laser scanning for the photoexfoliation of graphite to synthesize graphene.

1.1 Ultrafast Optics

The field of Ultrafast Optics centers around pulsed laser technology with pulse durations on the order of picoseconds and below [1]. Ultra short pulses have several characteristics that make them useful for a plethora of applications such as fast time resolution, high spatial resolution, high bandwidth, and the potential for high intensities. Some common applications include:

- Ultrafast spectroscopy – time-resolved spectroscopy benefits from the high temporal resolution provided by femtosecond laser pulses to probe characteristics and material processes that happen on short times scales (fs to ps). Examples are pump-probe experiments to study electronic and vibrational dynamics in solids [2-5]

- Laboratory extreme physics – lasers with 10^{13} W/cm^2 and above, directed onto solid targets, allow the study of physics at extreme conditions, such as probing nonlinear quantum electrodynamics on a table top [6]; intensities in excess of 10^{22} W/cm^2 have been achieved [7]
- Biomedical applications – ultrafast lasers have become important in ophthalmological applications on account of their reduced collateral tissue damage during surgical procedures, such as LASIK [8, 9]
- Materials processing – ultrafast lasers are widely used for micromachining, exhibiting superior performance, due again to causing less damage to surrounding material [10]; ultrafast lasers have also been demonstrated to produce nanomaterials, such as laser induced periodic structures (LIPS) [11, 12] and nanoparticles [13-21]

While a continuous, single-mode laser has a very narrow optical frequency, ultrashort pulses require a broad optical bandwidth, thus exhibiting multiple longitudinal modes. Forcing a large number of modes, hence a large bandwidth, to oscillate with a fixed phase relationship is the foundation of mode-locking. Once mode-locked (either actively or passively), the periodicity of the pulses, also known as the repetition rate, is given by $T = 1/\Delta f$, where Δf is the bandwidth. The pulse duration is given by $\Delta t = 1/(N\Delta f)$, where N is the number of modes, meaning the pulse duration is equal to the inverse of the total laser bandwidth [1].

Typically, mode-locked oscillators generate ultrafast pulse energies on the order of nJ, corresponding to peak powers on the order of kW and intensities on the order of 10^{12} W/cm^2 (assuming a 100 fs pulse at 100 MHz repetition rate focused near the diffraction limit) [22]. Amplification is required to achieve higher intensities, which is limited by the damage threshold

of the internal optics of the laser. The enabling step for extremely high power ultrafast lasers to achieve intensities beyond 10^{13} W/cm^2 is Chirped Pulse Amplification (CPA) developed by Gérard Mourou and co-workers in the 1980's [23]. CPA is broken down into three steps [22, 24], as seen in figure 1.1:

1. An initial seed pulse (from a fiber oscillator) is sent through a dispersive system (a pair of gratings), resulting in a highly chirped, stretched pulse. This stretching preserves the bandwidth while reducing the peak power by the stretching factor.
2. The stretched pulse then goes through a series of amplifiers to increase its power. Since the pulse is stretched and the peak power is reduced, nonlinear effects (such as self focusing) and optical damage, are significantly reduced. Without pulse stretching, the amplified pulse would damage the internal optics of the laser thus reducing the amount of amplification possible.
3. The amplified, stretched pulse goes through a second dispersive system that is opposite to the initial dispersive system resulting in the pulse being compressed to the bandwidth limit ensuring maximum peak power.

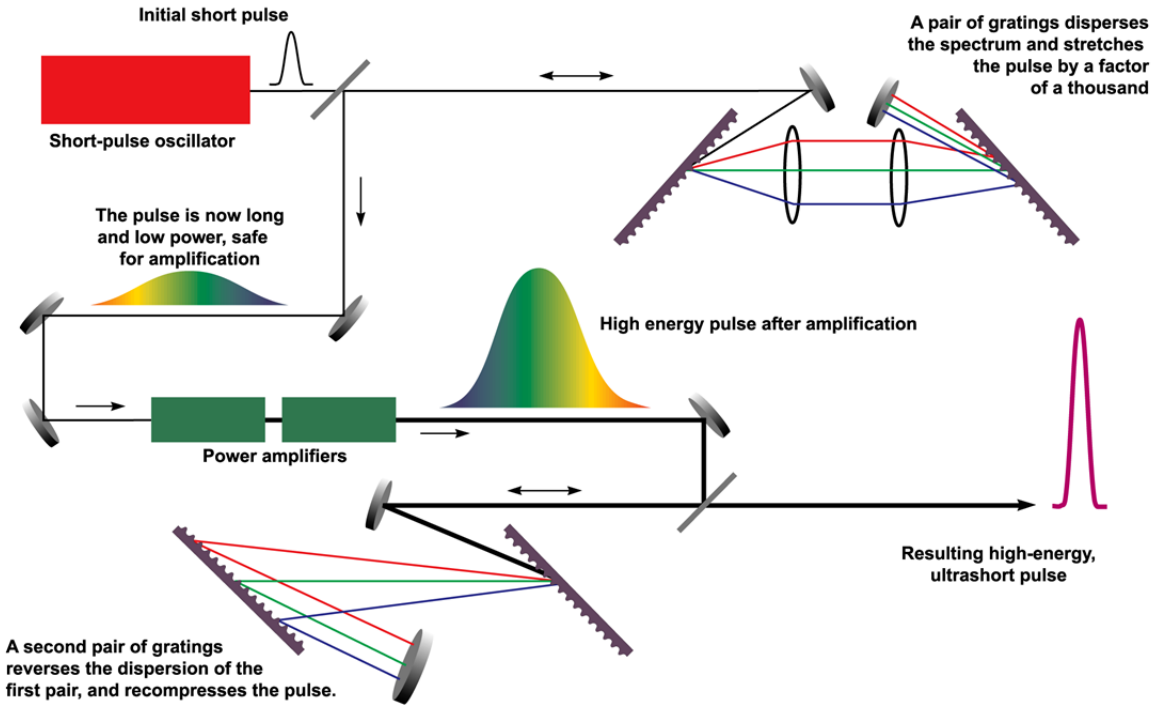

FIGURE 1.1: Schematic of CPA [24]

1.2 Ultrafast Pulsed Laser Deposition (UFPLD) of Semiconductor Nanoparticles

Pulsed Laser Deposition (PLD) conceptually is amongst the simplest thin-film deposition techniques. It consists of a target holder and a substrate holder housed in a vacuum chamber with a high powered pulsed laser as the external energy source to vaporize the target material and deposit thin films [25]. Excimer lasers are the primary laser source for PLD, with a pulse duration on the order of a nanosecond and a pulse energy on the order of a joule. Deposition can be done under vacuum or with a gas atmosphere of choice [26]. The basis of UFPLD is to replace the nanosecond excimer laser with a much shorter pulse (ultrafast) laser. In contrast to an excimer laser, which vaporizes or "ablates" material from a deep (~ micron) region below the irradiated target surface, UFPLD has been demonstrated to produce nanoparticles under vacuum

conditions [13-17, 20, 21, 27-30]. One of the aims of this dissertation is to use UFPLD for synthesizing semiconductor nanoparticle thin films of silicon and germanium.

1.2.1 Project Motivation

The fundamental motivation is to investigate the properties of semiconductor nanoparticle thin films produced by UFPLD. The goal is developing an electronically tunable quantum dot-based thin film material that has superior electronic mobility to current colloidal quantum dot thin films, which are on the order of 10^{-5}-10^{-3} cm^2/Vs [31].

1.2.2 Semiconductor Nanoparticle Properties

Nanoparticles are a relatively new form of matter with interesting optoelectronic properties different than those of bulk material. What is interesting about nanoparticles is their density of states distribution. When the particle is small enough, approaching the exciton Bohr radius, the electron wavefunction becomes confined in three dimensions and the density of states in that case becomes a delta functions, meaning there are only discreet energy levels, akin to those in an atom. For germanium and silicon, the Bohr exciton radii are 24.3 nm and 5 nm, respectively [32, 33]. The comparison of the density of states for various dimensionalities is shown in Figure 1.2 [34].

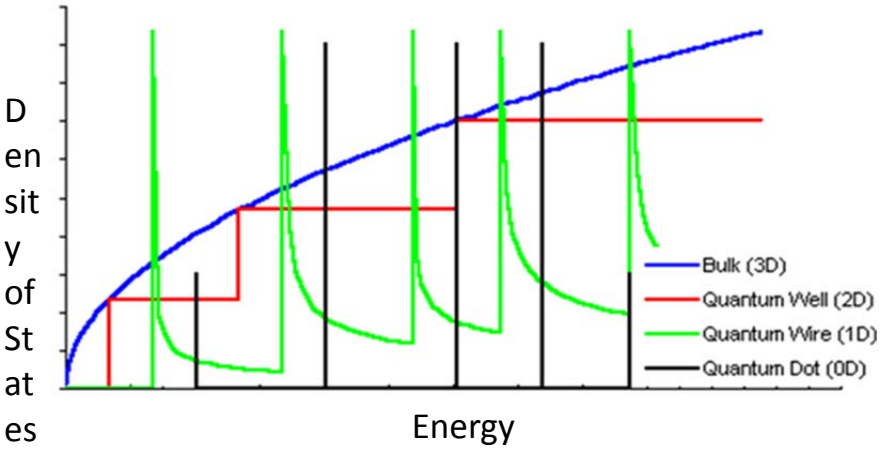

FIGURE 1.2. Density of states for 3D, 2D, 1D, and 0D structures [34]

For semiconductors with dimensions on the order of the Bohr exciton radius and smaller, the energy states begin to be size-dependent, and the bandgap itself gets larger as expressed in equation 1.1 [35] below:

$$E_g^{QD} \cong E_g + \frac{\hbar^2\pi^2}{2R^2}\left[\frac{1}{m_e} + \frac{1}{m_h}\right] - \frac{1.8e^2}{\epsilon R} + smaller\ terms \qquad 1.1$$

Where E_g is the bulk bandgap, R is the particle size, m_e and m_h are the electron and hole effective masses. This quantum confinement effect has been confirmed experimentally through photoluminescence, where silicon nanocrystals with diameters between 2.5 and 8nm were measured [36]. The smaller the nanoparticle, the larger the energy level spacing which gives better absorption at the shorter wavelengths. An interesting application of such nanoparticles would be for photovoltaic use. Having this enhanced absorption in the shorter wavelengths (UV/blue) has been shown to increase the photo-response of polycrystalline silicon solar cells.

This can be achieved by using an ultra-thin layer of silicon nanoparticles. Large photovoltaic enhancements of up to 60% have been seen in the UV/blue range [37].

Bulk semiconductors such as silicon or germanium have a limited range of absorption determined by their band gap. To maximize the absorption of solar radiation it is necessary to tailor the band gap to the solar spectrum. This is obviously not possible for a single-layer crystalline solar cell. Figure 1.3 shows the spectral response for various semiconductors [38] (on the left) and a diagram of a band gap (on the right), if the energy of the incident photon is less than the band gap, no absorption would occur and no electron/hole pair is created [39]. If the energy of the incident photon is higher than the band gap, the excited electron relaxes to the conduction band edge and the excess energy is lost as heat. This is the basis of the Shockley-Queisser limit on the maximum efficiency of a single-cell photovoltaic material (about ~30% for Silicon with a band gap of 1.1 eV)

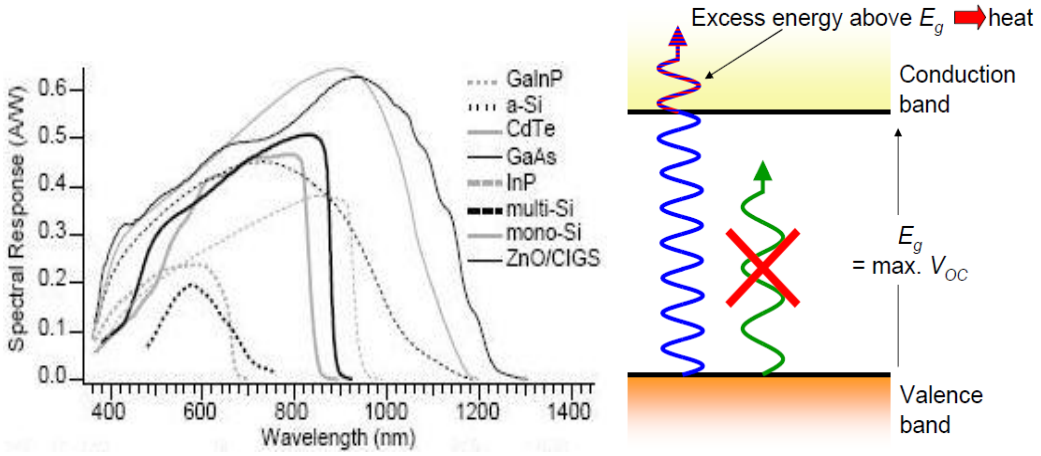

FIGURE 1.3. Spectral response for commonly used semiconductors [38] (left); and a diagram of the photovoltaic effect [39] (right)

Since there is a relationship between the confinement size of a semiconductor system and its band gap, having a distribution of various sizes also yields a range of band gaps. Being able

to control the distribution of particle sizes allows for fine-tuning of the absorption and thus the possibility of optimization over larger spectral ranges. For example, building a photovoltaic device using thin films of semiconductor nanoparticles could enhance the sensitivity to the entire solar spectrum, possibly increasing solar cell efficiency.

1.2.3 UFPLD Nanoparticle Formation Mechanisms

While the formation mechanism for nanoparticles is not well understood for UFPLD, At least two possibilities exist for nanoparticle generation in femtosecond ablation: direct cluster ejection from the target or collisional sticking and aggregation within the ablation plume [20]; a third possibility has been considered, which is condensation from a hot dense plasma [20, 40]. Since nanoparticles can form in vacuum with a femtosecond laser [13-16], the formation mechanism is quite different compared to condensation due to a background gas, as seen with nanosecond PLD [20]. Small clusters are attributed to collision-induced condensation within dense regions of the ablation plume. This is unlikely to be the formation mechanism of larger droplets due to the unrealistically high number of collisions required. The large droplets are a result of target stress confinement, when the pulse duration is shorter than the time needed for mechanical equilibrium of the target causing cavitation and disruption of a liquid surface region or mechanical spallation of the solid regions [40]. Evidence for nanoparticle condensation is seen time resolved optical emission spectroscopy of the ablation plume, showing an initial atomic emission dominated spectrum, changing into a blackbody dominated plume after a few μs indicating a plume dominated by nanoclusters [15, 20]. Figure 1.4 shows the time-resolved emission spectrum for silicon [15].

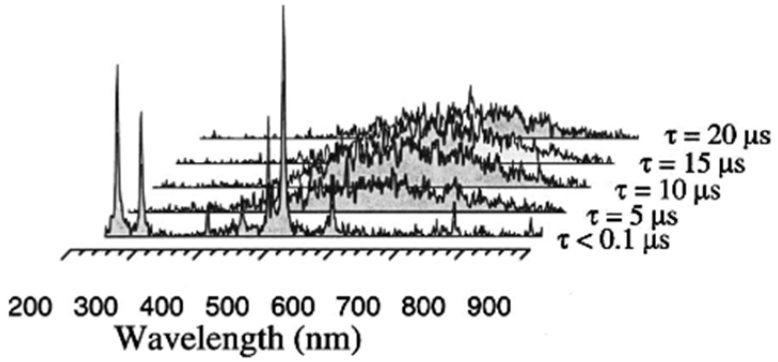

FIGURE 1.4. Time-resolved emission spectrum of the silicon ablation plume, initially showing atomic emission, evolving into a blackbody spectrum of hot nanoparticles [15]

A fluence dependence on the type of deposited matter has been seen by Perrière [20]: fluences higher than 15 J/cm^2 favors larger droplet formation (with reduced nanoparticle generation), which is likely from target stress confinement [40], leading to the following relationship for laser fluence [20]:

$$F_{atomic} \approx F_{nanocluster} < F_{droplet}$$

One of the mechanisms of nanoparticle and droplet condensation is from the adiabatic expansion of the ablation plume, with the initial region confined due to self-generating magnetic fields confining the plume immediately above the surface. The confining magnetic fields become weaker as distance from the surface increases until the outward pointing radial pressure exceeds the magnetic field confinement pressure and begins to quickly expand [30]. This is analogous to a rapidly expanding jet leaving a nozzle where clusters of gas and metal vapors also form [20, 41, 42], as seen in figure 1.5.

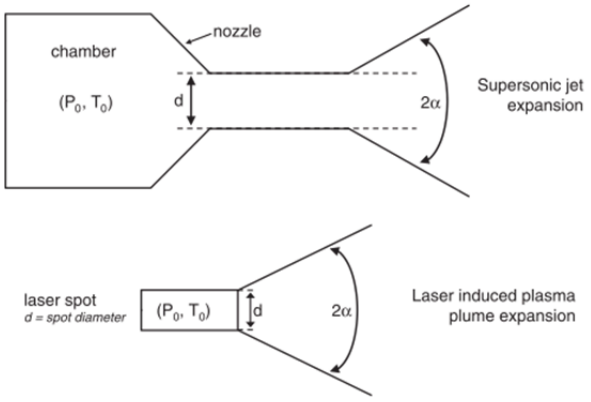

FIGURE 1.5. Schematic of a supersonic jet (top) and laser plume expansion (bottom) [20]

Appropriate flow conditions for cluster formation can be expressed by a scaling factor, Γ^*, given by the empirical equation 1.2 [41],

$$\Gamma^* = \frac{k\left[\left(\frac{d}{\tan\alpha}\right)^{0.85} P_o\right]}{T^{2.29}} \qquad 1.2$$

where k is a material dependent constant, P_o and T_0 are the initial gas pressure and temperature, d is the jet throat diameter (or laser spot size), and α is the jet expansion half angle as seen in figure **1.5** above. Clusters begin to form when Γ^* exceeds 300 [42]. Previous work [20] has shown that larger expansion angles, α, which correspond to smaller laser spot size and higher fluence correlates with droplet formation while smaller angles correspond to nanoparticle-favored growth. A comparison is shown in figure 1.6

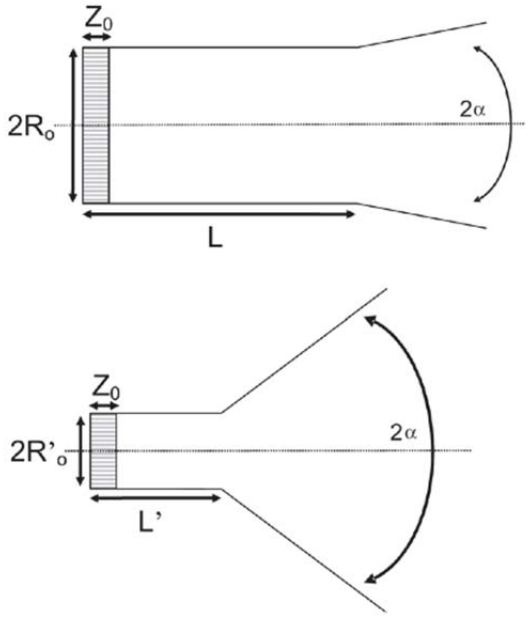

FIGURE 1.6. A comparison of the adiabatic expansion of the ablation plume at larger spot sizes (top) and smaller spot sizes (bottom) [20]

1.3 Ultrafast Photoexfoliation of Graphite

In addition to nanoparticle laser deposition, ultrafast lasers also have a potential for materials processing at the nanoscale. In the second part of this thesis, we scanned an ultrafast laser over a film of graphite particles that had been chemically intercalated with sulfate ions to form a new surface of graphitic aggregates. This method, developed here for the first time, is shown to lead to graphene-like carbon sheets.

1.3.1 Project Motivation

The project motivation is to synthesize a film of graphene nanosheets with ultrafast laser irradiation to be used in energy storage applications, especially for high capacitance supercapacitors. Supercapacitors are a very attractive energy storage device; they have very high charge and discharge at rates, long cycle life (far higher than battery cells), and high energy

efficiency [43]. One of the main limitations of supercapacitors is their limited energy density (typically 5-10 Wh/kg), which is lower than that of lead-acid (20-35 Wh/kg), nickel metal hydride (40-100 Wh/kg), and lithium-ion cells (120-170 Wh/kg) [44]. The use of graphene-based electrodes has become quintessential with pushing the boundary of energy density in supercapacitors [44-57].

1.3.2 Graphene Properties

Graphene is a material of high current interest due to its very interesting physical characteristics. One is the very high carrier mobility, observed to be in excess of 15,000 cm^2/Vs, leading to very low values of the electrical resistivity of 10^{-6} Ω-cm, which is about 35% lower than copper at room temperature, and high in-plane thermal conductivities of 5,300 W/mK [58-60]. Another interesting property is the very high specific surface area of 2,600 m^2/g, even exceeding those of activated carbon and carbon fiber cloth: 1,200 and 1,630 m^2/g, respectively [58, 61].

1.3.3 Ultrafast Laser Irradiated Graphite Formation Mechanisms

First, we discuss the scientific basis of the laser-induced exfoliation process. We discuss the process using a simple analysis of the interaction between two neighboring graphene sheets in the graphite structure which is widely acknowledged to be governed by the balance between van der Waals-like attractive forces and repulsive molecular orbital interactions.

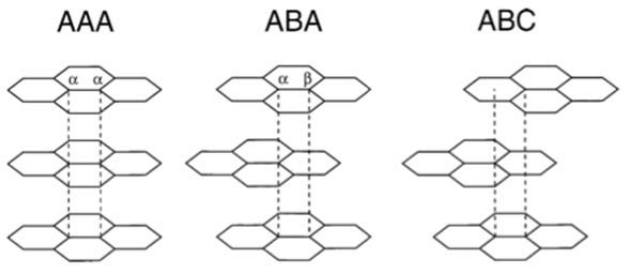

FIGURE 1.7. Graphite interplanar stacking arrangements [62]

Palser [62] has modeled the interlayer interactions using the following potential of equation 1.3:

$$V(r) = \frac{C}{r^6}\left[1 - \sum_{n=0}^{6} \frac{(\alpha r)^n}{n!} e^{-\alpha r}\right] \quad (1.3)$$

Where the adjustable parameters C (11.0 meV $Å^6$) and α (2.7 $Å^{-1}$) are determined by requiring that the model return the correct experimentally determined interplanar cohesive energy for graphite ABA stacking of 42.6 meV per atom and the equilibrium interplanar spacing of 0.335nm [62], as seen in figure 1.8. Note here that the interlayer cohesive energy is vastly weaker than the *in-plane* cohesive energy which is several eV per atom (set by the strength of the covalent sp^2 bond). This disparity between in-plane and out-of-plane bonding is what makes this exfoliation process possible. The interaction of the femtosecond laser pulse with the graphite nanoflakes, then, supplies the necessary energy to overcome the interlayer cohesion, without disrupting the in-plane bonding, consequently producing graphene nanoplatelets.

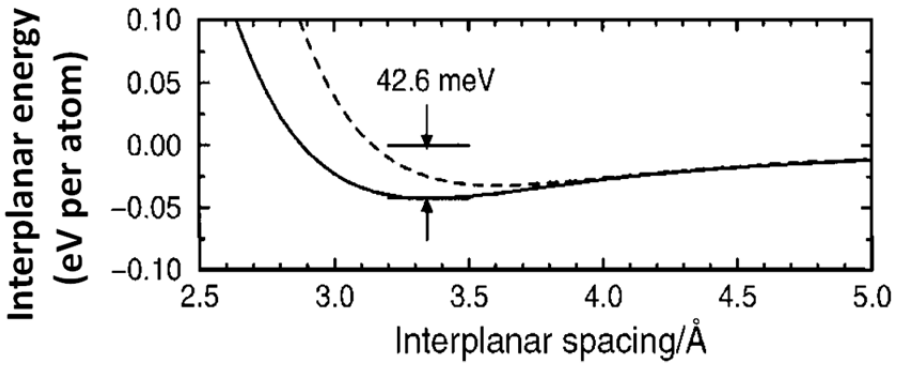

FIGURE 1.8. Interplanar interaction energy for different graphene plane stacking as a function of interplanar spacing; the solid and dashed lines refer to ABA (graphite) and AAA (simple hexagonal) stacking types [62]

It is important to point out here that the laser fluence must be adjusted to an optimum level above the threshold for separating the interlayer bond, yet well below the fluence required to affect the in-plane bond.

It has been proposed and calculated, using time-dependent density functional theory for the electrons and molecular dynamics for the ions, that an ultrafast laser may be able to directly photoexfoliate one graphene layer at a time, with pulses being on the order of 45 fs, longer pulses would ablate multi-layered graphene [63]. In previous work [64], it has been observed by ultrafast electron crystallography that when graphite is excited by an ultrafast laser pulse, excited carriers (which reach equilibrium in less than a picosecond) transfers their heat to strongly coupled optical phonons. Initially the crystal undergoes a contraction, followed by large expansion. The as the fluence increases, the contraction velocity increases causing a larger expansion, leading to ablation of entire graphene layers at a sufficiently high fluence.

One approach to make this process more energetically favorable, perhaps allowing photoexfoliation at longer pulse durations, is to oxidize graphite into graphite oxide to increase the interplanar distance [65], followed by a means of exfoliation, followed by a chemical reduction of the graphite oxide sheets into graphene. Exfoliation can be done with heat or mechanical means (such as ultrasonification) [58, 66]. Recent work has shown that lasers, both continuous and femtosecond, are able to exfoliate and reduce graphene oxide (photoexfoliation and photoreduction) in a single step [63, 67-70]. Here we investigate the photoexfoliation process both in intercalated samples, as well as direct photoexfoliation of pristine (non-intercalated) nanoparticles.

1.4 Supercapacitors

The energy that can be stored in a supercapacitor is given by equation 1.4:

$$E = \frac{1}{2} C V^2 \qquad 1.4$$

Stored energy, E, is proportional to the capacitance, C, and the square of the voltage, V. Ideally, the best way to get the most energy out of a capacitor is to increase the voltage, but some applications, especially those requiring large energy densities, limit the amount of voltage that can be used. For example, electric cars have battery packs typically on the order of 350 V, due to safety reasons [71]. In practice, the voltage is really limited by the dielectric breakdown potential of the materials used to make the supercapacitor. The next strategy would be to increase the capacitance of the system, which is given by equation 1.5:

$$C = \frac{\varepsilon_r \varepsilon_o A}{D} \qquad 1.5$$

Capacitance, C, is proportional to the permittivity of free space, ε_o, relative permittivity, ε_r, and electrode area, A, while being inversely proportional to electrode separation, D. The strategy to increase capacitance is to increase the surface area of the electrodes, which is a fundamental design parameter in modern electrochemical supercapacitors [43]. A supercapacitor consists of two electrodes (positive and negative) with a separator sandwiched between. The separator is electrically insulating but allows ion transport to allow the electrodes to be as close as possible while preventing short circuits. The electrodes are submerged into an electrolyte solution, either with aqueous or organic solvents with a dissociated ionic species. Charge is stored by the dissociated ionic species adsorbing onto the surface of the electrode when under bias, which is known as electric double-layer capacitance [43] as seen in figure 1.9 below.

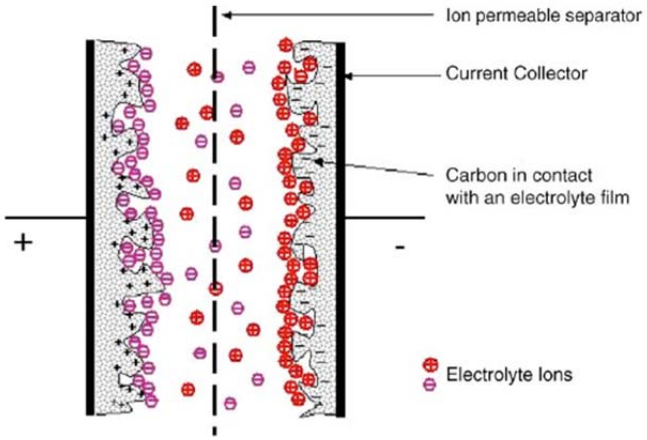

FIGURE 1.9. Schematic of electric double layer capacitance [43]

In an asymmetrical supercapacitor, one electrode capacitance contribution is from double-layer capacitance while the other electrode utilizes pseudocapacitance [43], which involves fast and reversible redox reactions as seen in figure 1.10.

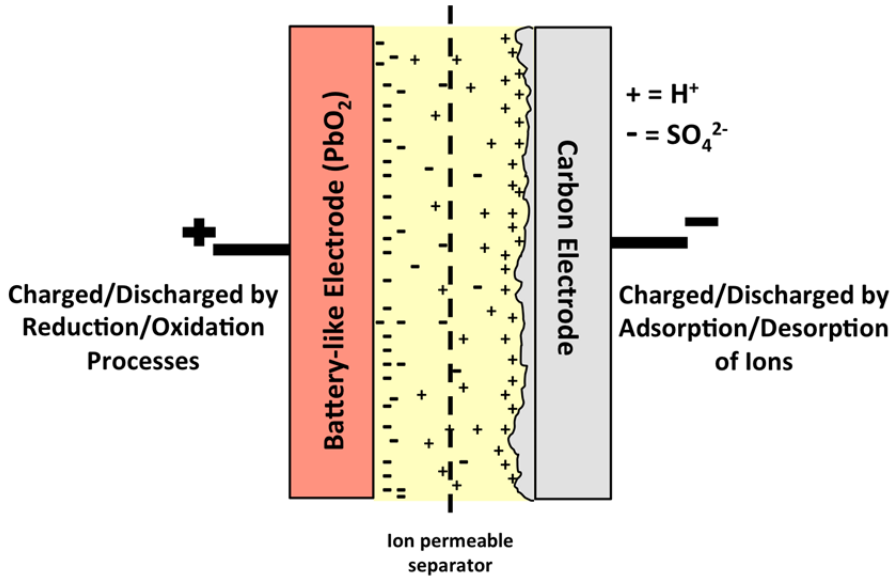

FIGURE 1.10. Schematic of a charged PbO_2/Carbon asymmetrical supercapacitor

On the positive plate, the same half reaction that lead-acid batteries are based on takes place:

$$PbO_2 + 4H^+ + {SO_4}^{2-} + 2e^- \rightleftharpoons PbSO_4 + 2H_2O$$

On the negative plate, instead of having a lead counter electrode that reacts with the sulfate in the electrolyte, a high surface area carbon is used for double-layer capacitance. Here the negative electrode acts to adsorb and desorb H^+ ions in the electrolyte:

$$n{C_6}^{x-}(H^+)_x \rightleftharpoons n{C_6}^{(x-2)-}(H^+)_{x-2} + 2H^+ + 2e^-$$

Prototypes based on asymmetric PbO_2/Activated Carbon systems have shown equivalent series resistance (ESR) as low as 0.12 Ω cm^2 and an RC time constant of 0.36 seconds [72]. These values are comparable to those of activated carbon based symmetrical supercapacitors, implying very high charge and discharge rates. The advantage that the asymmetrical system has is superior energy density. Mathematical modeling of asymmetric PbO_2/Activated Carbon supercapacitors has predicted an energy density of 24 Wh/kg [73], approaching that of a conventional lead acid cell, which is typically 30-40 Wh/kg [74].

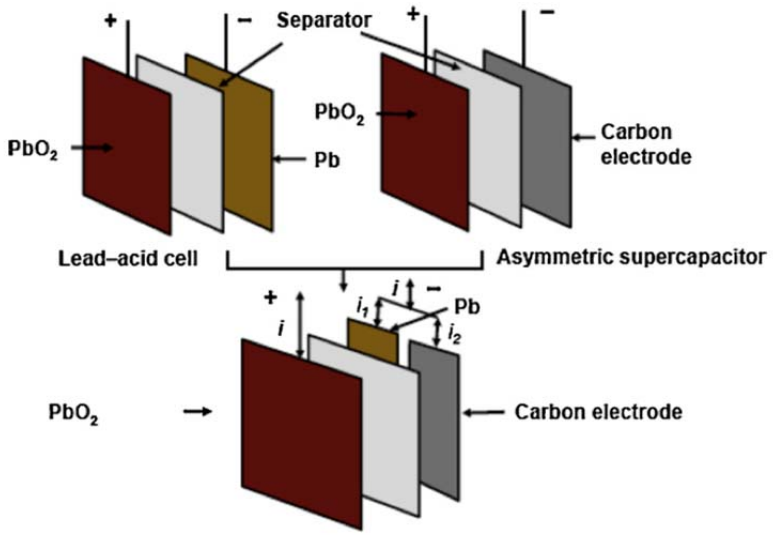

FIGURE 1.11. Schematic of an ultrabattery, combining a PbA battery cell with a PbO2/Carbon asymmetrical supercapacitor [75]

Figure 1.11 above is an example of the ultrabattery, which is a hybrid between an asymmetrical supercapacitor and a lead acid battery cell where the negative plate consists of one carbon electrode and one lead electrode connected in parallel with a lead oxide positive counter electrode [75]. This cell is designed to use its supercapacitor aspects to better handle high pulsed currents while retain its battery aspect for larger energy density. Ultrabatteries have demonstrated 170k km of successful operation on a Honda Insight hybrid electric vehicle (HEV) exhibiting better cycling performance than a nickel metal hydride (NimH) battery pack [76].

1.5 Thesis Organization

This thesis project is an overview of material synthesis and processing using an ultrafast laser. The materials studied are germanium, silicon, and graphite. There are two facets to this project, one is the study of material that is removed off of a laser target during ablation, UFPLD, and the second is the effects of ultrafast laser irradiation on a material. The thesis is divided into six chapters, including this introduction. The second chapter is a description of the experimental apparatus as well as characterization techniques used. The third chapter characterizes germanium and silicon nanoparticles and nanoparticle thin films produced by UFPLD. The fourth chapter is an investigation of ultrafast laser irradiation of graphite with the first section studying ejected graphitic nanostructures from a laser target using UFPLD as well as effects (such as photoexfoliation) from the ultrafast laser when scanned over a film of graphite particles, Ultrafast Laser Irradiated Graphite (ULIG). Chapter 5 focuses on a practical application of ULIG by using it as an electrode coating to improve the charging performance of lead acid

battery cells. Chapter 6 is the final chapter, summarizing the conclusions and suggesting future work that would pertain to this topic.

1.6 References

1. Weiner, A., *Introduction and Review*, in *Ultrafast Optics*. 2009, John Wiley & Sons: New Jersey, USA. p. 1-31.

2. Stoica, V., Y.-M. Sheu, D. Reis, and R. Clarke, *Wideband Detection of Transient Solid-State Dynamics Using Ultrafast Fiber Lasers and Asynchronous Optical Sampling.* Optics Express, 2008. **16**(4).

3. Elzinga, P., F. Lytle, Y. Jian, and G. Laurendeau, *Pump/Probe Spectroscopy by Asynchronous Optical Sampling.* Applied Spectroscopy, 1987. **41**(1): p. 2-4.

4. Perrin, B., *Investigation of Short-Time Heat Transfer Effects by an Optical Pump–Probe Method*, in *Microscale and Nanoscale Heat Transfer*. 2007, Springer: Berlin.

5. Nakajima, M., K. Mizoguchi, K. Morita, K. Itoh, H. Harima, and S. Nakashima, *Comparison of coherent and incoherent LO phonons in isotopic 70 Ge/ 74 Ge Superlattices.* Journal of Luminescence, 2000. **87**(89): p. 942-944.

6. Mourou, G.r.A., C.P.J. Barry, and M.D. Perry, *Ultrahigh-Intensity Lasers: Physics of the Extreme on a Tabletop.* Physics Today, 1998. **51**(1): p. 22.

7. Yanovsky, V., V. Chvykov, G. Kalinchenko, P. Rousseau, T. Planchon, T. Matsuoka, A. Maksimchuk, J. Nees, G. Cheriaux, G. Mourou, and K. Krushelnick, *Ultra-high intensity - 300-TW laser at 0.1 Hz repetition rate.* Optical Express 2008. **16**(3): p. 2109-2114.

8. Montes-Mico, R., A. Rodriguez-Galietero, and J.L. Alio, *Femtosecond laser versus mechanical keratome LASIK for myopia.* Ophthalmology, 2007. **114**(1): p. 62-8.

9. Vogel, A., T. Günther, M. Asiyo-Vogel, and R. Birngruber, *Factors determining the refractive effects of intrastromal photorefractive keratectomy with the picosecond laser.* Journal of Cataract & Refractive Surgery, 1997. **23**(9): p. 1301-1310.

10. Cerami, L., E. Mazur, S. Nolte, and C. Schaffer, *Femtosecond Laser Micromachining*, in *Ultrafast Nonlinear Optics*, R. Thomson and C. Leburn, Editors. 2013, Springer International Publishing.

11. Li, Y., V.A. Stoica, L. Endicott, G. Wang, H. Sun, K.P. Pipe, C. Uher, and R. Clarke, *Femtosecond laser-induced nanostructure formation in Sb2Te3.* Applied Physics Letters, 2011. **99**(12): p. 121903.

12. Huang, M., F. Zhao, Y. Cheng, N. Xu, and Z. Xu, *Mechanisms of ultrafast laser-induced deep-subwavelength gratings on graphite and diamond.* Physical Review B, 2009. **79**(12).

13. Oraiqat, I., J. Kennedy, J. Mathis, and R. Clarke, *Femtosecond laser deposition of semiconductor quantum dot films.* 2012: p. 402-417.

14. Amoruso, S., G. Ausanio, R. Bruzzese, L. Gragnaniello, L. Lanotte, M. Vitiello, and X. Wang, *Characterization of laser ablation of solid targets with near-infrared laser pulses of 100fs and 1ps duration.* Applied Surface Science, 2006. **252**(13): p. 4863-4870.

15. Amoruso, S., R. Bruzzese, N. Spinelli, R. Velotta, M. Vitiello, X. Wang, G. Ausanio, V. Iannotti, and L. Lanotte, *Generation of silicon nanoparticles via femtosecond laser ablation in vacuum.* Applied Physics Letters, 2004. **84**(22): p. 4502.

16. Ausanio, G., S. Amoruso, A.C. Barone, R. Bruzzese, V. Iannotti, L. Lanotte, and M. Vitiello, *Production of nanoparticles of different materials by means of ultrashort laser pulses.* Applied Surface Science, 2006. **252**(13): p. 4678-4684.

17. Rode, A.V., B. Luther-Davies, and E.G. Gamaly, *Ultrafast ablation with high-pulse-rate lasers. Part II: Experiments on laser deposition of amorphous carbon films.* Journal of Applied Physics, 1999. **85**(8): p. 4222.

18. Liu, B., Z. Hu, and Y. Che, *Ultrafast lasers produce nanoparticles.* Laser Focus World, 2007. **43**(9): p. 74-+.

19. Gamaly, E.G., N.R. Madsen, D. Golberg, and A.V. Rode, *Expansion-limited aggregation of nanoclusters in a single-pulse laser-produced plume.* Physical Review B, 2009. **80**(18).

20. Perrière, J., C. Boulmer-Leborgne, R. Benzerga, and S. Tricot, *Nanoparticle formation by femtosecond laser ablation.* Journal of Physics D: Applied Physics, 2007. **40**(22): p. 7069-7076.

21. Eliezer, S., N. Eliaz, E. Grossman, D. Fisher, I. Gouzman, Z. Henis, S. Pecker, Y. Horovitz, M. Fraenkel, S. Maman, and Y. Lereah, *Synthesis of nanoparticles with femtosecond laser pulses.* Physical Review B, 2004. **69**(14).

22. Weiner, A., *Manipulation of Ultrashort Pulses*, in *Ultrafast Optics*. 2009, John Wiley & Sons: New Jersey, USA. p. 362-420.

23. Maine, P., D. Strickland, P. Bado, M. Pessot, and G. Mourou, *Generation of Ultrahigh Peak Power Pulses by Chirped Pulse Amplification* IEEE Journal of Quantum Electronics, 1988. **24**(2): p. 398-403.

24. Perry, M., *Multilayer Dielectric Gratings: Increasing the Power of Light.* Science & Technology Review, Lawrence Livermore National Lab, 1995.

25. Cheung, J., *History and Fundamentals of Pulsed Laser Deposition*, in *Pulsed Laser Deposition of Thin Films*, D. Chrisey and G. Hubler, Editors. 1994, John Wiley & Sons: United States. p. 1-19.

26. Green, S., A. Pique, K. Harshavardhan, and J. Bernstein, *Equipment*, in *Pulsed Laser Deposition of Thin Films*, D. Chrisey and G. Hubler, Editors. 1994, John Wiley & Sons: USA. p. 23-54.

27. Senadheera, S., B. Tan, and K. Venkatakrishnan, *Critical Time to Nucleation: Graphite and Silicon Nanoparticle Generation by Laser Ablation.* Journal of Nanotechnology, 2009. **2009**: p. 1-6.

28. Moore, A.R., *Electron and hole drift mobility in amorphous silicon.* Applied Physics Letters, 1977. **31**(11): p. 762.

29. Zhang, Z., *Characteristics of Ultrafast Laser Produced Plamsa and its Application in Thin Film Deposition*, in *Electrical Engineering*. 2003, University of Michigan.

30. Rompay, P.A.V., *Mass Separation for Ions in Ultrafast Ablation Plumes*. 2003, University of Michigan.

31. Konstantatos, G. and E.H. Sargent, *Nanostructured materials for photon detection.* Nat Nanotechnol, 2010. **5**(6): p. 391-400.

32. Maeda, Y., N. Tsukamoto, Y. Yazawa, Y. Kanemitsu, and Y. Masumoto, *Visible photoluminescence of Ge microcrystals embedded in SiO2 glassy matrices.* Applied Physics Letters, 1991. **59**(24): p. 3168.

33. Cullis, A.G., L.T. Canham, and P.D.J. Calcott, *The structural and luminescence properties of porous silicon.* Journal of Applied Physics, 1997. **82**(3): p. 909.

34. *Semiconductor Physics: Density of States*. Available from: http://britneyspears.ac/physics/dos/dos.htm.

35. Brus, L., *Electronic Wave Functions in Semiconductor Clusters: Experiment and Theory* Journal of Physical Chemistry 1986. **90**: p. 2555-2560.

36. Ledoux, G., J. Gong, F. Huisken, O. Guillois, and C. Reynaud, *Photoluminescence of size-separated silicon nanocrystals: Confirmation of quantum confinement.* Applied Physics Letters, 2002. **80**(25): p. 4834.

37. Stupca, M., M. Alsalhi, T. Al Saud, A. Almuhanna, and M.H. Nayfeh, *Enhancement of polycrystalline silicon solar cells using ultrathin films of silicon nanoparticle.* Applied Physics Letters, 2007. **91**(6): p. 063107.

38. *Solar Cell Spectral Response Measurement Errors Related to Spectral Band Width and Chopped Light Waveform*. NREL/CP-530-22969 1997; Available from: http://www.nrel.gov/docs/legosti/fy97/22969.pdf.

39. Hudelson, S., P. Bermel, and T. Heidel. *Energy 101: Solar*. Available from: http://www.mitenergyclub.org/assets/2008/11/6/Solar101-Oct2008.pdf.

40. Zhigilei, L.V., *Dynamics of the plume formation and parameters of the ejected clusters in short-pulse laser ablation.* Applied Physics A: Materials Science & Processing, 2003. **76**(3): p. 339-350.

41. Hagena, O.F., *Cluster ion sources (invited).* Review of Scientific Instruments, 1992. **63**(4): p. 2374.

42. Ditmire, T., T. Donnelly, A.M. Rubenchik, R.W. Falcone, and M.D. Perry, *Interaction of intense laser pulses with atomic clusters.* Physical Review A, 1996. **53**(5).

43. Pandolfo, T., V. Ruiz, S. Sivakkumar, and J. Nerkar, *General Properties of Electrochemical Capacitors*, in *Supercapacitors Materials, Systems, and Applications*, F. Béguin and E. Frąckowiak, Editors. 2013, Wiley-VCH. p. 69-110.

44. Liu, C., Z. Yu, D. Neff, A. Zhamu, and B.Z. Jang, *Graphene-based supercapacitor with an ultrahigh energy density.* Nano Lett, 2010. **10**(12): p. 4863-8.

45. Brownson, D.A. and C.E. Banks, *Fabricating graphene supercapacitors: highlighting the impact of surfactants and moieties.* Chem Commun (Camb), 2012. **48**(10): p. 1425-7.

46. Kim, T., G. Jung, S. Yoo, K.S. Suh, and R.S. Ruoff, *Activated Graphene-Based Carbons as Supercapacitor Electrodes with Macro- and Mesopores.* Acs Nano, 2013. **7**(8): p. 6899-6905.

47. Kim, T.Y., H.W. Lee, M. Stoller, D.R. Dreyer, C.W. Bielawski, R.S. Ruoff, and K.S. Suh, *High-Performance Supercapacitors Based on Poly(ionic liquid)-Modified Graphene Electrodes.* Acs Nano, 2011. **5**(1): p. 436-442.

48. Ku, K., B. Kim, H. Chung, and W. Kim, *Characterization of graphene-based supercapacitors fabricated on Al foils using Au or Pd thin films as interlayers.* Synthetic Metals, 2010. **160**(23-24): p. 2613-2617.

49. Vivekchand, S.R.C., C.S. Rout, K.S. Subrahmanyam, A. Govindaraj, and C.N.R. Rao, *Graphene-based electrochemical supercapacitors.* Journal of Chemical Sciences, 2008. **120**(1): p. 9-13.

50. Wang, K., L.W. Li, and X.Z. Wu, *Synthesis of Graphene and Electrochemical Performance.* International Journal of Electrochemical Science, 2013. **8**(5): p. 6763-6766.

51. Wang, Y., Z. Shi, Y. Huang, Y. Ma, C. Wang, M. Chen, and Y. Chen, *Supercapacitor Devices Based on Graphene Materials.* Journal of Physical Chemistry C, 2009. **113**(30): p. 13103-13107.

52. Yan, J., Z. Fan, T. Wei, W. Qian, M. Zhang, and F. Wei, *Fast and reversible surface redox reaction of graphene–MnO2 composites as supercapacitor electrodes.* Carbon, 2010. **48**(13): p. 3825-3833.

53. Yoo, J.J., K. Balakrishnan, J. Huang, V. Meunier, B.G. Sumpter, A. Srivastava, M. Conway, A.L. Reddy, J. Yu, R. Vajtai, and P.M. Ajayan, *Ultrathin planar graphene supercapacitors.* Nano Lett, 2011. **11**(4): p. 1423-7.

54. Zhang, F., T.F. Zhang, X. Yang, L. Zhang, K. Leng, Y. Huang, and Y.S. Chen, *A high-performance supercapacitor-battery hybrid energy storage device based on graphene-enhanced electrode materials with ultrahigh energy density.* Energy & Environmental Science, 2013. **6**(5): p. 1623-1632.

55. Zhang, L.L., R. Zhou, and X.S. Zhao, *Graphene-based materials as supercapacitor electrodes.* Journal of Materials Chemistry, 2010. **20**(29): p. 5983.

56. Zhang, Y., H. Li, L. Pan, T. Lu, and Z. Sun, *Capacitive behavior of graphene–ZnO composite film for supercapacitors.* Journal of Electroanalytical Chemistry, 2009. **634**(1): p. 68-71.

57. Zhu, Y., S. Murali, M.D. Stoller, K.J. Ganesh, W. Cai, P.J. Ferreira, A. Pirkle, R.M. Wallace, K.A. Cychosz, M. Thommes, D. Su, E.A. Stach, and R.S. Ruoff, *Carbon-based supercapacitors produced by activation of graphene.* Science, 2011. **332**(6037): p. 1537-41.

58. Rao, C., U. Maitra, and H. Matte, *Synthesis, Characterization, and Selected Properties of Graphene*, in *Graphene Synthesis, Properties, and Phenomena*, C. Rao and A. Sood, Editors. 2013, Wiley-VCH.

59. Maryland, U.o. *Electrons Can Travel Over 100 Times Faster In Graphene Than In Silicon, Physicists Show*. 2008; Available from: http://www.sciencedaily.com/releases/2008/03/080324094514.htm.

60. Novoselov, K.S., A.K. Geim, S.V. Morozov, D. Jiang, M.I. Katsnelson, I.V. Grigorieva, S.V. Dubonos, and A.A. Firsov, *Two-dimensional gas of massless Dirac fermions in graphene.* Nature, 2005. **438**(7065): p. 197-200.

61. Pandolfo, A.G. and A.F. Hollenkamp, *Carbon properties and their role in supercapacitors.* Journal of Power Sources, 2006. **157**(1): p. 11-27.

62. Palser, A.H.R., *Interlayer interactions in graphite and carbon nanotubes.* Physical Chemistry Chemical Physics, 1999. **1**: p. 4459-4464.

63. Miyamoto, Y., H. Zhang, and D. Tománek, *Photoexfoliation of Graphene from Graphite: An Ab Initio Study.* Physical Review Letters, 2010. **104**(20).

64. Carbone, F., P. Baum, P. Rudolf, and A. Zewail, *Structural Preablation Dynamics of Graphite Observed by Ultrafast Electron Crystallography.* Physical Review Letters, 2008. **100**(3).

65. Hummer, W.S. and R.E. Offema, *Preparation of Graphitic Oxide* Journal of the American Chemical Society, 1958. **80**(6): p. 1339.

66. Stankovich, S., D.A. Dikin, R.D. Piner, K.A. Kohlhaas, A. Kleinhammes, Y. Jia, Y. Wu, S.T. Nguyen, and R.S. Ruoff, *Synthesis of graphene-based nanosheets via chemical reduction of exfoliated graphite oxide.* Carbon, 2007. **45**(7): p. 1558-1565.

67. El-Kady, M.F., V. Strong, S. Dubin, and R.B. Kaner, *Laser Scribing of High-Performance and Flexible Graphene-Based Electrochemical Capacitors.* Science, 2012. **335**(6074): p. 1326-1330.

68. Trusovas, R., K. Ratautas, G. Račiukaitis, J. Barkauskas, I. Stankevičienė, G. Niaura, and R. Mažeikienė, *Reduction of graphite oxide to graphene with laser irradiation.* Carbon, 2013. **52**: p. 574-582.

69. Mukherjee, R., A. Varghese, Thomas, A. Krishnamurthy, and N. Koratkar, *Photothermally Reduced Graphene as High-Power Anodes for Lithium-Ion Batteries.* American Chemical Society Nano 2012. **6**(9): p. 7867-7878.

70. Sokolov, D.A., K.R. Shepperd, and T.M. Orlando, *Formation of Graphene Features from Direct Laser-Induced Reduction of Graphite Oxide.* Journal of Physical Chemistry Letters, 2010. **1**(18): p. 2633-2636.

71. Corrigan, D. and A. Masias, *Batteries for Electric and Hybrid Vehicles* in *Linden's Handbook of Batteries*, T. Reddy and D. Linden, Editors. 2011, McGraw-Hill.

72. Burke, A., *R&D considerations for the performance and application of electrochemical capacitors.* Electrochimica Acta, 2007. **53**(3): p. 1083-1091.

73. Kazaryan, S.A., S.N. Razumov, S.V. Litvinenko, G.G. Kharisov, and V.I. Kogan, *Mathematical Model of Heterogeneous Electrochemical Capacitors and Calculation of Their Parameters.* Journal of The Electrochemical Society, 2006. **153**(9).

74. Salkind, A. and G. Zguris, *Lead-Acid Batteries*, in *Linden's Handbook of Batteries*, T. Reddy and D. Linden, Editors. 2011, McGraw-Hill.

75. Cooper, A., J. Furakawa, L. Lam, and M. Kellaway, *The UltraBattery—A new battery design for a new beginning in hybrid electric vehicle energy storage.* Journal of Power Sources, 2009. **188**(2): p. 642-649.

76. Furukawa, J., T. Takada, D. Monma, and L.T. Lam, *Further demonstration of the VRLA-type UltraBattery under medium-HEV duty and development of the flooded-type UltraBattery for micro-HEV applications.* Journal of Power Sources, 2010. **195**(4): p. 1241-1245.

CHAPTER 2

Experimental Set Up

2.1 Laser Source and Optics

The laser used for all the experiments in this thesis is the Clark MXR CPA2001. This laser is a solid state Ti:Sapphire ultrafast laser with a fundamental wavelength of 780 nm and a pulse duration of 150 fs with a beam diameter of 5mm. The repetition rate is 1 kHz with an 800 μJ pulse energy and an average power of 800 mW. The resulting peak power is 5 GW.

All the optical elements in the various experimental arrangements using this laser are chosen specifically for the CPA2001 laser. In a normal dispersion medium, the higher frequencies travel slower than the lower frequencies resulting in the pulse being stretched with an up-chirp which is known as Group Velocity Dispersion (GVD). All lens material is fused silica to minimize GVD due to its low dispersion. All mirrors are dielectric coated with maximum reflectance at 780nm and minimal GVD. Two sets of optics were used to obtain two different spot sizes for subsequent experiments. The first set of focusing optics consist of a beam expander, consisting of a -100 mm focal length negative plano-concave lens and a 550 mm plano-convex with a resulting magnification factor of 5.5x. The expanded beam is focused with a 750 mm lens into a spot calculated to be 27 μm in diameter. The second set of optics consists of a single fused silica lens with a focal length of 681 mm giving a spot size of 135 μm [1, 2]. For higher fluence experiments, the first set of optics is used.

2.2 Ultrafast Pulsed Laser Deposition Apparatus

Figure 2.1 shows the experimental set up for Ultrafast Pulsed Laser Deposition (UFPLD). The ultrafast laser beam first goes through a set of focusing optics to be focused down onto the target of choice (in this project the materials are germanium, silicon, and graphite) to ablate material and create the plasma plume. The nanoparticles that are generated are collected on a substrate of either glass or holey carbon coated TEM grids. Since the laser beam is incident at 45^{o} from the target normal, the focused laser spot forms an ellipse. Taking in account the change in laser spot geometry, the peak intensity and fluence for the first set of optics (using a beam expander) is 6.5 x 10^{14} W/cm^2 and 98 J/cm^2, respectively. The second set of optics, using a single lens for focusing, gives a peak intensity and fluence of 2.6 x 10^{13} W/cm^2 and 3.9 J/cm^2. The deposition process is housed a vacuum chamber operating with a background pressure of about 4 x 10^{-7} torr. The substrate holder contains a quartz-halogen filament heater capable of heating the substrate up to 800° C if necessary [3].

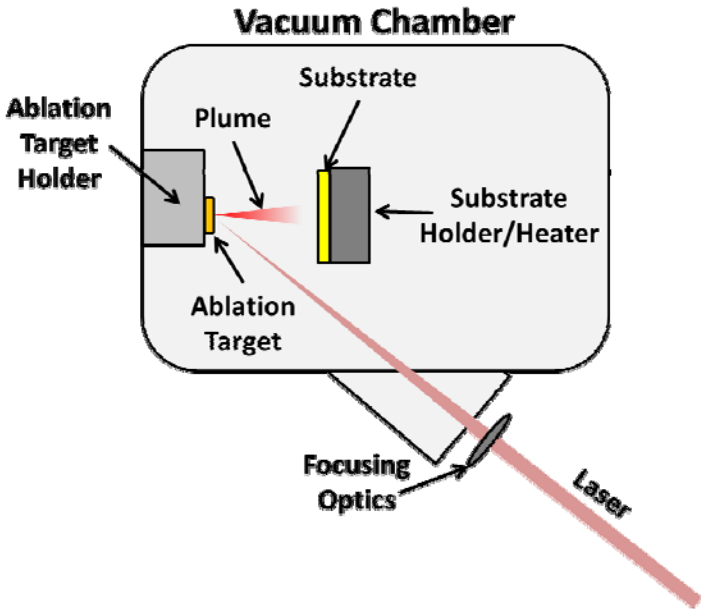

FIGURE 2.1. Schematic of the UFPLD chamber experimental set up [3]

The glass substrates are either borosilicate glass or quartz of dimensions 25mm x 50mm in size and are about 1mm thick. Figure 2.2 shows the plasma plume produced in this set up for silicon, germanium, and aluminum.

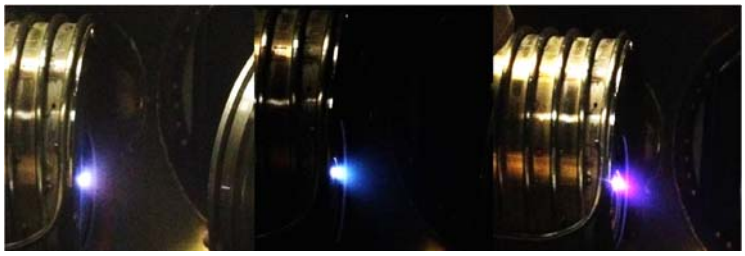

FIGURE 2.2. Images of the plasma plume, from left to right: Silicon, Germanium, and Aluminum. The laser fluence in each case is 98 J/cm^2 [3].

2.3 Ultrafast Laser Irradiated Graphite Apparatus

The experimental set-up for the ultrafast irradiation consists of three main components: the ultrafast laser, the optics, and a two-dimensional translation stage. The optics consists of an attenuating neutral density filter (Thor Labs Part No. NDC-100C-4), a fused silica plano-convex cylindrical lens (f=100 mm, Thor Labs Part no. LJ4395), and a two-dimensional servo motor translation stage (Thor Labs Part no. MTS50-Z8).

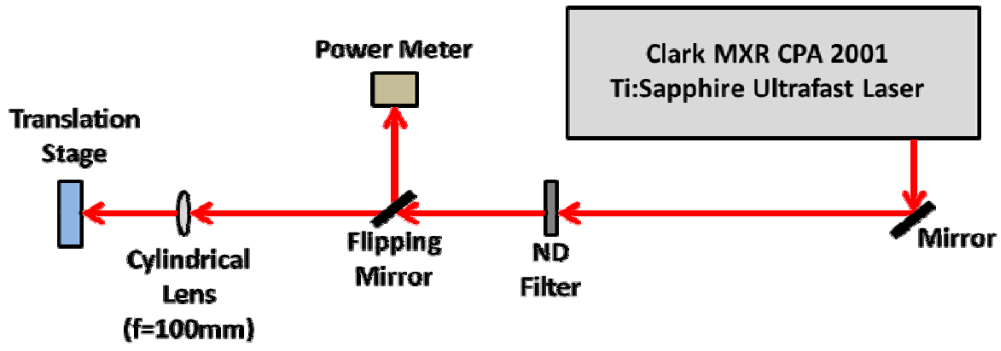

FIGURE 2.3. Schematic of the ultrafast irradiation set up

As shown in Figure 2.3, the laser first goes through a variable neutral density filter to control the incident laser power. Before the laser is allowed to pass to the cylindrical lens, a flipping mirror is placed to intercept the beam and send it to a power meter where measurements are made while adjusting the neutral density filter to a desired setting.

2.3.1 Direct Laser Scribing

Once the beam is attenuated through the neutral density filter, it passes to the cylindrical plano-convex lens to focus a line (of approximately 5 mm in length) onto the sample, which is placed on the translation stage. A close up is seen in Figure 2.4.

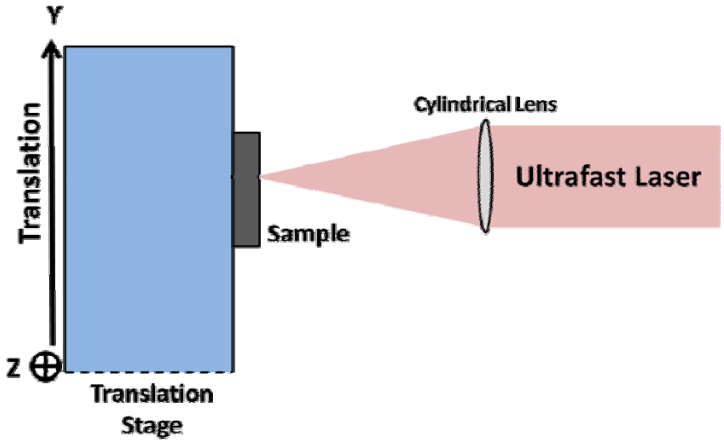

FIGURE 2.4. Close up of the translation set up

As the translation stage moves, the focused line scans the sample (at a rate of 0.1 mm/s.), allowing a larger area of coverage compared to using a convex lens, which focuses into a spot, as seen in Figure 2.5.

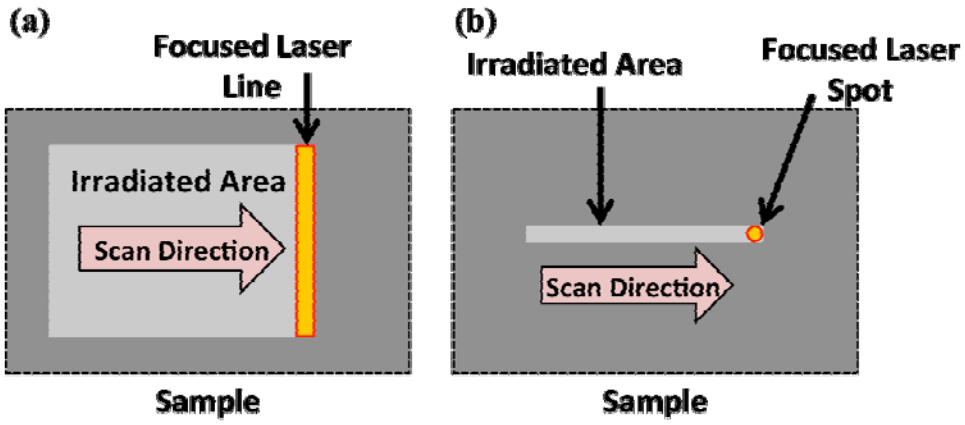

FIGURE 2.5. Diagram of the scanning profile, (a) using a cylindrical plano-convex lens, (b) using a standard plano- convex lens

2.3.2 Irradiation from Rear of the Film

The experimental set up in figure 2.6 allows the ultrafast laser to be focused onto the backside of a film that is confined by a glass substrate in order to induce a shockwave to transfer material onto a substrate. This type of laser printing has been used in previous work by Yalisove et al. as means to deposit nanoparticles by irradiating the back of a continuous metal thin film [4]. This arrangement again uses a cylindrical lens to focus a line on the sample in order to improve throughput. Instead of a metallic thin film, a graphite coating is applied to a thin, transparent microscope coverslip (Corning, 0.13-16 mm thick). Material is deposited on a receiving substrate (a Si wafer to be SEM friendly) that is kept at a distance 0.13-0.16 mm from the target with spacers (also coverslips). The laser focus line is stationary and scanning is done by moving the translation stage.

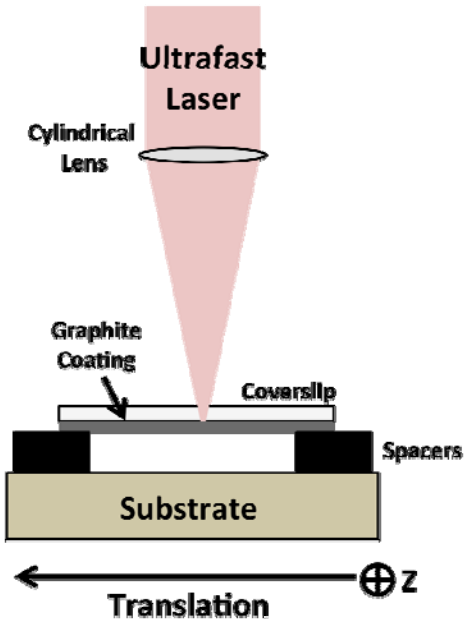

FIGURE 2.6. Diagram of the scanning set up for irradiation from the rear of the film, using a cylindrical plano-convex lens

2.4 Material Characterization Techniques

During this project, a plethora of characterization tools were necessary. The following sections list and briefly explain the tools and techniques used.

2.4.1 Optical Emission Spectroscopy

One of the ways to characterize what is in the ultrafast ablation plume is to measure its emission spectrum. Figure 2.7 shows a schematic of how the spectrum is recorded. An imaging lens is used to couple an image of the plume into a fiber that is fed into a spectrometer and is attached to one of the viewports on the vacuum chamber where there is a clear view of the plume. A shortpass filter at 760 nm is used to reject the laser signal and protect the detector in the spectrometer. The spectrometer is a Control Development model 2DCCD array spectrometer with a spectral range of 305-1000 nm.

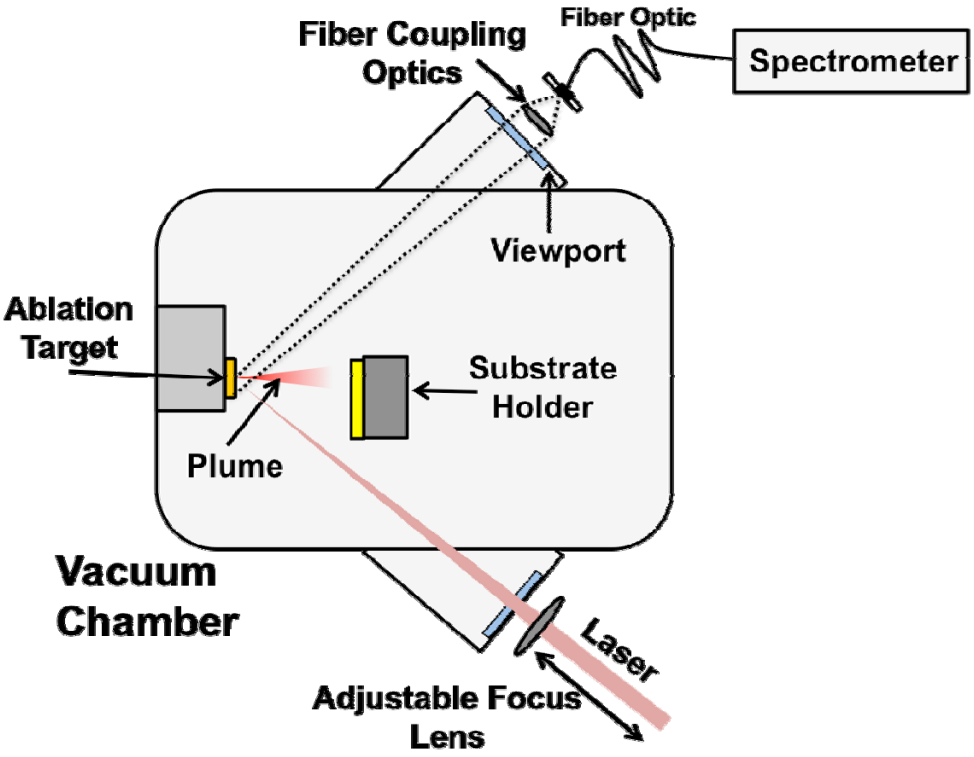

FIGURE 2.7. Optical Spectroscopy set up to measure ablation plume spectrum as a function of focusing conditions.

2.4.2 Scanning Electron Microscopy

Scanning Electron Microscopy (SEM) is useful for studying overall sample morphologies. Since the features in this thesis are on the nanometer scale, a high resolution field emission SEM is required. The instrument used for all of the images in this thesis is the FEI Nova 200 Nanolab SEM/FIB located at the Michigan Center for Materials Characterization. The resolution of this instrument is ~2nm.

2.4.3 Transmission Electron Microscopy

Transmission Electron Microscopy (TEM) is useful when extreme resolution (atomic scale) is required and is also important when studying nanoparticle size distributions when high resolution, 2-D images with good contrast at the edge of features is highly desirable. The instrument used for all of the TEM images in this thesis is the JEOL 3011 High Resolution Electron Microscope located at the Michigan Center for Materials Characterization.

2.4.4 Atomic Force Microscopy

Atomic Force Microscopy (AFM) is useful not only for high resolution lateral imaging, but also for extracting accurate height information from nanoscale features that is not possible with other microscopy techniques. The AFM used is the Veeco Dimension, located at the Michigan Center for Materials Characterization. Tapping mode with Bruker TESP-SS super sharp silicon tips are used for the work in this thesis.

2.4.5 X-ray Diffraction

X-Ray diffraction (XRD) is used to probe the crystal structure of thin film nanoparticle films produced by UFPLD by studying Bragg peak positions from constructive interference in a crystalline solid giving insight into the internal structure of the material. The Rigaku Ultima IV with the thin film attachment is used and is located at the Central Campus Electron Microscopy Analysis Lab.

2.4.6 Raman Spectroscopy

Raman spectroscopy gives molecular vibrational information of a material from studying inelastic scattering from a laser excitation source. This tool becomes is important when studying

material nanostructure effects on phonons. The Renishaw inVia Raman Microscope at excitation wavelengths of 514 and 633 nm are used for this project. This instrument is located in the Department of Chemistry, University of Michigan.

2.4.7 Optical Spectroscopy

Optical spectroscopy of thin film semiconductors can give insight towards their electronic structure by measuring in what wavelengths they are transparent or opaque. For example, optical absorption edges can give information about the optical band gap of the material. For this project a broadband light source (quartz halogen lamp with a blackbody spectrum of 3200 K) was used to shine light though a sample, the spectrometer used to measure the optical transmission spectrum is the Control Development 2DCCD model with a spectral range of 305-1000 nm.

2.4.8 Fourier-Transform Infrared Spectroscopy (FTIR)

FTIR spectroscopy is a technique used to obtain an infrared spectrum from a material. Dispersive spectroscopy, as mentioned in section 2.4.7, becomes difficult to do in the IR range. An FTIR consists of a Michelson interferometer with a motorized mirror to vary the optical path length to generate an interferogram that is converted into a spectrum by Fourier transformation. The Perkin-Elmer Spectrum GX, with a range of 4000 to 700 cm^{-1} is used.

2.4.9 Hall Measurement

For measuring the mobility, carrier concentration, and conductivity, electronic transport measurements were performed on germanium nanoparticle films produced by UFPLD at various

temperatures. A Hall-bar configuration was used, as illustrated in figure 2.8, prepared in the Lurie Nanofabrication Facility (LNF) with the help of the Kurdak Group in the Physics Department. The prepared Hall bars were wired manually onto to a 16-pin dip header using 25-μm Cu wires and In solder. The samples were then inserted into a liquid He cryostat with a superconducting magnet, as seen in figure 2.9. The cryostat functioned in heating mode, allowing for measurements at temperatures ranging from 4.2 K to near room temperature. The superconducting magnet produces magnetic fields of -8 to 8 Tesla. Two Stanford SR830 lock-in amplifiers are used to simultaneously measure the longitudinal (V_{xx}) and transverse (V_{xy}) voltages, as seen in figure 2.8.

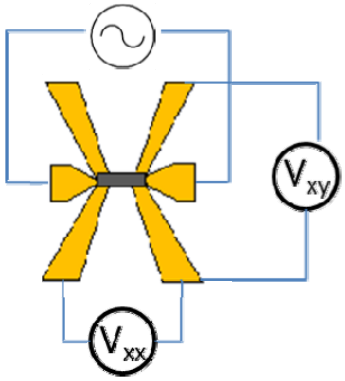

FIGURE 2.8. Hall-bar configuration used for transport measurements [5].

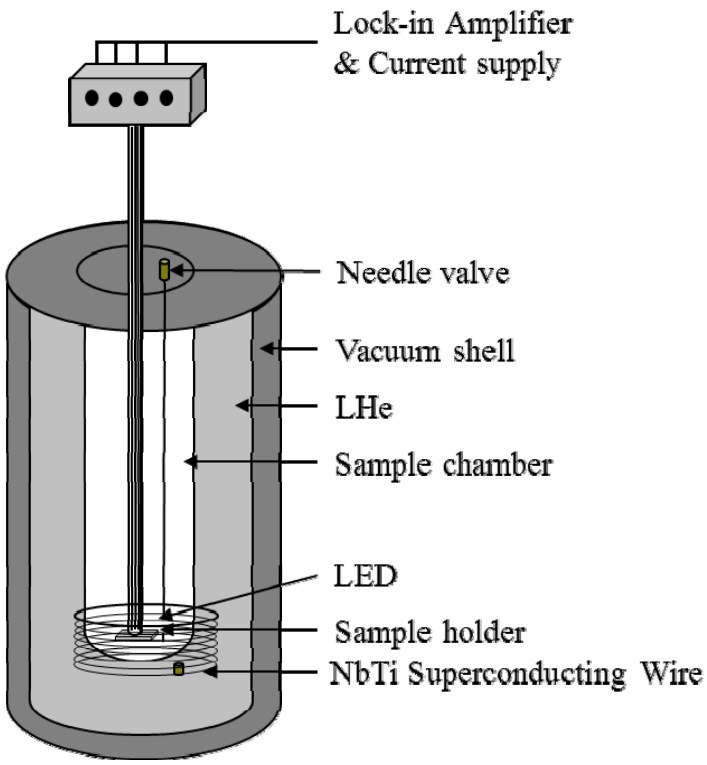

FIGURE 2.9. Hall measurement apparatus [5]

2.4.10 Asynchronous Optical Sampling (ASOPS)

Ultrafast Pump-Probe measurements can give insights into laser induced dynamics of a solid material. Taking time resolved snap shots requires the probe pulse to be delivered at various time delays. ASOPS allows time resolved data without the use of a mechanical delay system allowing a large temporal measurement window (up to 10 ns). The method was devised and patented by the Clarke Group [6]. Menlo Systems GmbH produces a commercial version of the system used. Figure 2.10 shows the experimental set up.

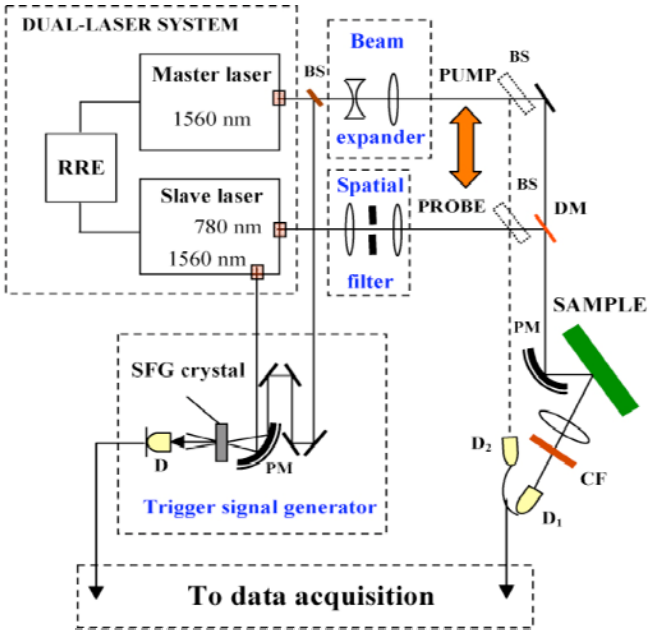

FIGURE 2.10. Schematic of the ASOPS system [7]

2.5 Battery Cell Characterization

The commercial battery cells used for this project were small 0.85 amp-hr AGM lead acid battery cells supplied by Electrodes and More. Commercially available 1.265 specific gravity (s.g.) sulfuric acid was used for the electrolyte. Cell electrochemical measurements were performed with a commercial battery cell analyzer, the MTI Corporation 8-Channel Battery Analyzer (BST8-3), capable of 6-3000 mA of current with voltages up to 5 V.

2.6 References

1. Fowles, G., *Introduction to Modern Optics*. 1975, New York: Holt, Rinehart and Winston.

2. *Gaussian Beam Optics*. 11/01/2015]; Available from: http://www.newport.com/Gaussian-Beam-Optics/144899/1033/content.aspx.

3. Oraiqat, I., J. Kennedy, J. Mathis, and R. Clarke, *Femtosecond laser deposition of semiconductor quantum dot films.* 2012: p. 402-417.

4. Murphy, R.D., M.J. Abere, K.J. Schrider, B. Torralva, and S.M. Yalisove, *Nanoparticle size and morphology control using ultrafast laser induced forward transfer of Ni thin films.* Applied Physics Letters, 2013. **103**(9): p. 093113.

5. Field, R., *Growth and Electronic Properties of GaAsN and GaAsBi Alloys*, in *Physics Department*. University of Michigan.

6. Stoica, V. and R. Clarke, *Method and system for measuring at least one property including a magnetic property of a material using pulsed laser sources* 2012, The Regents of The University of Michigan: United States of America.

7. Stoica, V., Y.-M. Sheu, D. Reis, and R. Clarke, *Wideband Detection of Transient Solid-State Dynamics Using Ultrafast Fiber Lasers and Asynchronous Optical Sampling.* Optics Express, 2008. **16**(4).

CHAPTER 3

Ultrafast Pulsed Laser Deposition (UFPLD) of Semiconductor Films

3.1 Overview

UFPLD is a deposition technique using an ultrafast laser to ablate a target of any given material to produce a thin film (a detailed description of the deposition set up is given in Chapter 2). With UFPLD, instead of having a continuous thin film, the deposited films consist of a large number of nanoparticles that are generated in the ultrafast laser ablation plume [1-5] and are collected and tightly packed on a substrate. Here we should point out that the substrate captures the nanoparticles that have condensed from the high-density plasma which expands and cools as it emanates from the ablation target. The focus of this chapter is the characterization of Group IV (silicon and germanium) semiconductor nanoparticle thin films produced using UFPLD, treated as continuous thin films.

The substrates used were borosilicate and SiO_2 glass 1 mm thick. These films are grown at different substrate temperatures using the sample heater in the vacuum chamber. The ultrafast laser wavelength is 780 nm with 800 μJ of energy per pulse at a repetition rate of 1 kHz focused using a fused silica lens with a focal length of 681 mm at the laser wavelength [6, 7]. Unless otherwise noted, the pulse laser spot intensity is calculated to be 2.62 x 10^{13} W/cm^2 with a fluence of 3.94 J/cm^2 using Gaussian beam optics [8]. All samples were grown in vacuum conditions of 2-8 x 10^{-7} torr.

3.2 Ablation Plume Spectroscopy

One method to gain insight into nanoparticle growth mechanisms is through spectroscopy. From the spectrum, it can be determined whether the plume consists of a collection of heated nanoclusters or if the plume is predominately composed of ionized gas. Early on in the project, it was noticed that if the laser were sufficiently out of focus, the color of the plume would change. To collect this spectral data, an image of the plume was coupled into a fiber using a lens, feeding into the array spectrometer (as discussed in Chapter 2) during ultrafast laser ablation. The laser-focusing lens was moved at various distances from best focus to study how the plume changes spectrally as a function of focus spot size, effecting the intensity and fluence at the target. Gaussian beam optics [8] is used to calculate how the focus spot size changes as the lens is moved from focus. Figure 3.1 shows how intensity (W/cm^2) and fluence (J/cm^2) changes as a function of lens distance from focus.

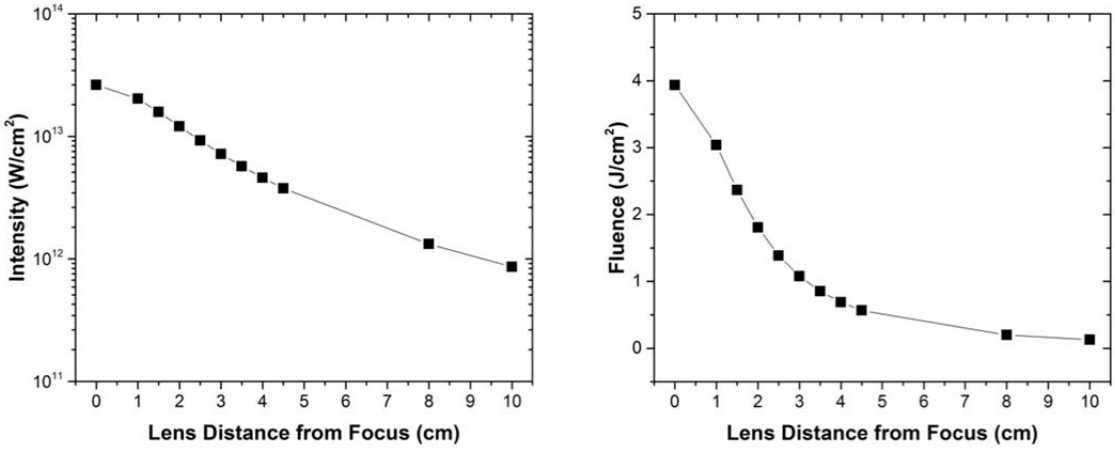

FIGURE 3.1. Intensity (left) and fluence (right) as a function of how far the focusing lens is positioned from best focus

Figure 3.2 shows the spectrum of the germanium ablation plume at best focus (laser focus spot intensity of 2.6 x 10^{13} W/cm^2 and a fluence of 3.9 J/cm^2) and the spectrum when the

focusing lens is 10 cm out of focus (laser focus spot intensity of 8.6 x 10^{11} W/cm^2 and a fluence of 0.13 J/cm^2). At best focus, the germanium plume spectrum consists predominately of atomic emission peaks while the spectrum becomes continuous when the lens is out of focus.

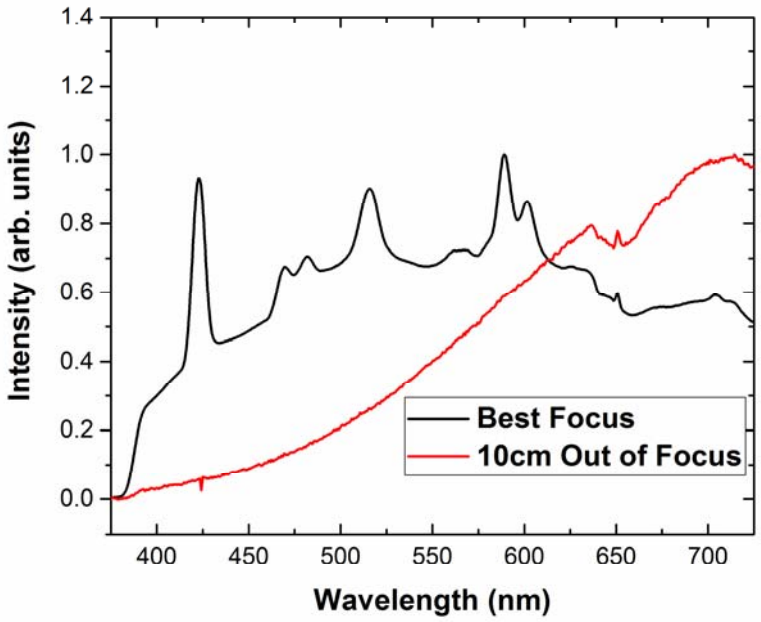

FIGURE 3.2. Spectrum of the Ge ablation plume at best focus (black line) and with the focusing lens placed 10cm out of focus (red line)

The emission peak locations were determined by finding the local maximum using the built-in peak finding algorithm in OriginPro 2015 and they agree well with the expected atomic emission lines of germanium. In table 3.1, the measured peaks are listed and compared with tabulated data from the National Institute of Standards and Technologies (NIST) website [9].

Measured Ge Peak Position (nm)	Ionic Species NIST	Tabulated Values (nm) NIST
422.8	Ge(I)	422.65625
469.4	Ge(II)	469.0023
481.8	Ge(II)	481.46084
516.0	Ge(II)	517.8460
562.4	Ge(I)	562.1428
567.6	Ge(I)	566.4844
589.0	Ge(II)	589.33886
601.8	Ge(II)	602.10414
626.6	Ge(II)	626.7141
703.4	Ge(II)	704.93694
712.2	Ge(I)	713.0117

TABLE 3.1. Measured peak positions of the germanium plume at best focus compared to tabulated values (as published) and corresponding ionization from NIST

Since there is a large difference in the spectrum between being in focus and 10 cm out of focus, it is important to capture what is happening during this transition. To capture this, a spectrum was recorded at various lens displacements from best focus. The chosen displacements were 1, 1.5, 2, 2.5, 3, 3.5, 4, 4.5, 8, and 10 cm. The lower range of 1cm was chosen since the depth of focus for the lens is 3.7 cm, so anything smaller than 1cm would essentially be at best focus and the upper limit of 10 cm was chosen due to the low intensity of the ablation plume. Figure 3.3 shows the spectrum change as a function of lens distance from best focus.

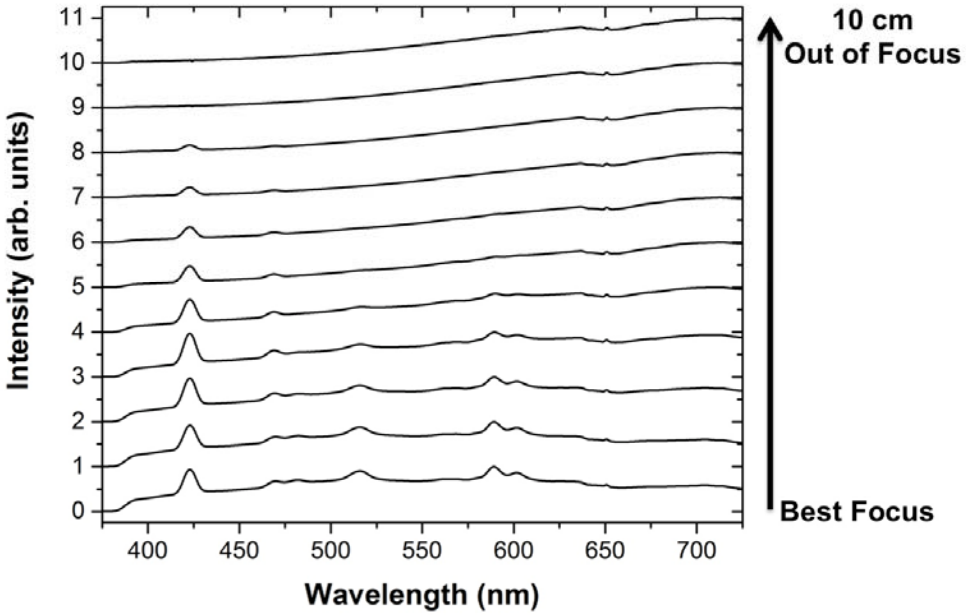

FIGURE 3.3. Spectrum of the Ge ablation plume at various focus positions (listed from the bottom going up): best focus, 1, 1.5, 2, 2.5, 3, 3.5, 4, 4.5, 8, and 10 cm

Not all of the emission peaks disappear at the same focus distance; the first peak to disappear is at 481.8 nm, Ge(II), at 2.5cm. The next peak to disappear is at 516.0 nm, Ge(II), at 3 cm followed by 562.4 and 567.6 nm at 3.5 cm. The rest of the peaks disappear before the lens reaches 8 cm, transitioning into the continuous spectrum. At first glance, the order of peak disappearance would seem to be attributed to initial relative peak intensities, except that initially 516.0, 589.0, and 601.8 nm peak positions have a higher relative intensity than the 469.4 nm peak which persists past the 4.5 cm lens position. It is interesting that in addition to the sharp emission lines characteristic of Ge there is a prominent continuum spectrum on which these sharp lines are sitting. We identify the continuum as being from black-body radiation from the hot plasma. Note that the peak wavelength of the continuum component (see Fig. 3.3) shifts from about 550 nm (corresponding to a temperature of ~5000K) to >700 nm in the most out of

focus condition (corresponding to a plume temperature of ~4000K). This red-shift in the Planck spectral distribution is consistent with the plasma expanding and cooling as it traverses from the laser target to the substrate. As the plasma cools, nanoparticles condense out of the plasma and travel towards the substrate where they then stick to the exposed surface by van der Waals attraction. The Plank spectral distribution is given by equation 1.1:

$$I(\nu, T) = \frac{2h\nu^3}{c^2} \frac{1}{e^{\frac{h\nu}{kT}} - 1} \qquad 1.1$$

where h is the Planck constant, c is the speed of light, k is the Boltzmann constant, ν is the frequency of light, and T is the temperature of the blackbody. The peak position red-shifts as the temperature of the body decreases and blue-shifts with increasing temperature.

The same experiment was conducted on the silicon ablation target. Figure 3.4 shows the ablation plume spectrum at best focus (laser focus spot intensity of 2.6 x 10^{13} W/cm^2 and a fluence of 3.9 J/cm^2) and with the lens 8 cm from focus (intensity of 1.3 x 10^{12} W/cm^2 and a fluence of 0.20 J/cm^2). A list of corresponding atomic peaks from NIST is shown in table 3.2. Again, the lower limit of 1 cm for the first lens displacement was used since the depth of focus of the optics is 3.7 cm and anything smaller than 1 cm would yield unnoticeable change. The upper limit was 8 cm, in contrast to the 10 cm for germanium, since the plume was not visible after that lens displacement. As with germanium, the silicon ablation plume spectrum was studied as a function of the lens displacement from best focus, as shown in figure 3.5. In contrast to germanium, the peaks reduced evenly and exhibited a new peak at 589.0 nm corresponding with the tabulated emission line of 589.879 nm, a Si(III) ion [9]. This peak appeared 4.5 cm out of focus and grew more intense at 8 cm out of focus, where the remainder of the spectrum is continuous.

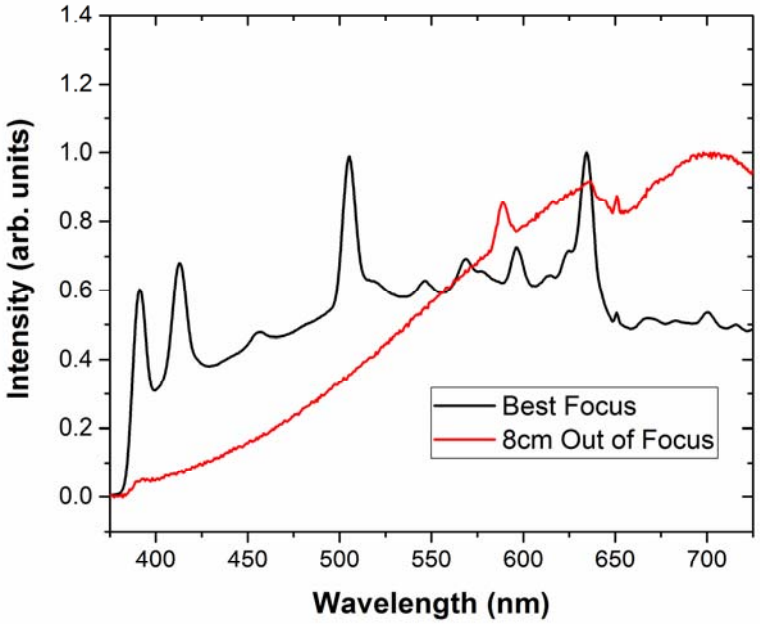

FIGURE 3.4. Spectrum of the Si ablation plume at best focus (black line) and with the focusing lens placed 8cm out of focus (red line)

Measured Si Peak Position (nm)	Ionic Species NIST	Tabulated Values (nm) NIST
391.2	Si(I)	390.5523
412.8	Si(II)	412.807
457.2	Si(III)	457.476
505.2	Si(II)	505.598
518.2	Si(II)	518.190
546.6	Si(II)	546.643
568.6	Si(I)	568.4484
576.8	Si(I)	576.2977
596.6	Si(II)	595.756
614.8	Si(I)	614.5015
625.2	Si(I)	625.4188
634.4	Si(II)	634.710
650.8	Si(III)	652.436
668.8	Si(II)	667.188
700.4	Si(IV)	704.794
716.0	Si(I)	716.469
727.0	Si(I)	727.5294
740.6	Si(I)	740.5774

TABLE 3.2. Measured peak positions of the silicon plume at best focus compared to tabulated values and corresponding ionization from NIST

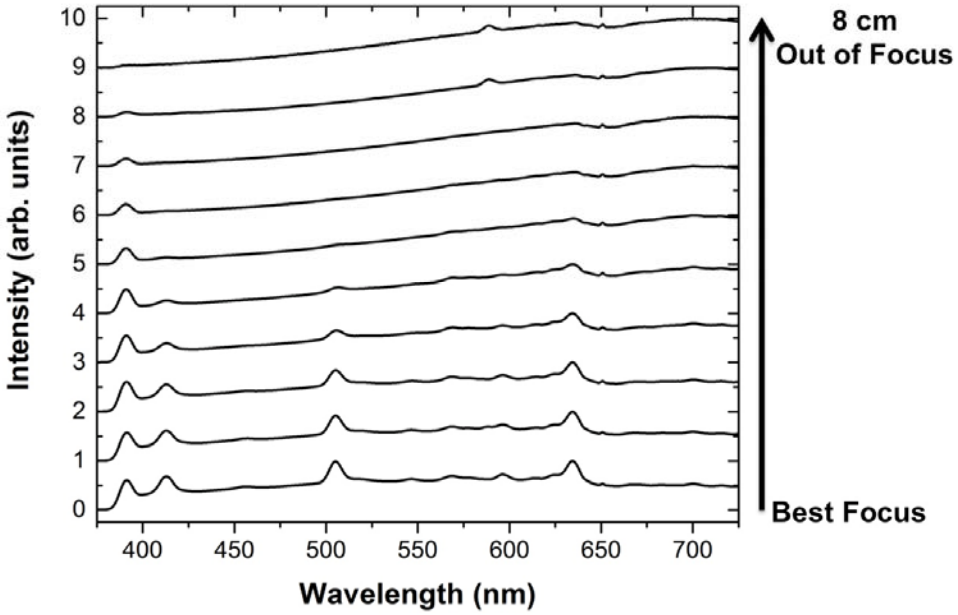

FIGURE 3.5. Spectrum of the Si ablation plume at various focus positions (listed from the bottom going up): best focus, 1, 1.5, 2, 2.5, 3, 3.5, 4, 4.5, and 8 cm

3.3 Size Distribution and Morphology

The particle size distributions were examined for silicon and germanium nanoparticles produced with UFPLD. The nanoparticles were deposited directly on holey carbon coated copper TEM grids. The deposition time for each sample was 30s for germanium and 45s for silicon at a chamber background pressure of 4 X 10^{-7} torr. Since there was a dramatic difference in the spectrum of the ablation plume that depends on focus, two samples of each material were prepared, one at best focus and one with the focusing lens 4.5 cm out of focus. Transmission electron microscopy was used to generate the micrographs and the particle sizes were measured individually using ImageJ and analyzed using OriginPro 2015.

The particle size distribution for germanium exhibits a lognormal distribution that changes with focus. At best focus (as shown in figure 3.6), the average diameter is 29.5 nm with

a standard deviation of 41.2 nm and a standard error (SE) of the mean of 2.2 nm. The large standard deviation is attributed to larger particles (> 100 nm) being present. The total amount of particles measured was 349.

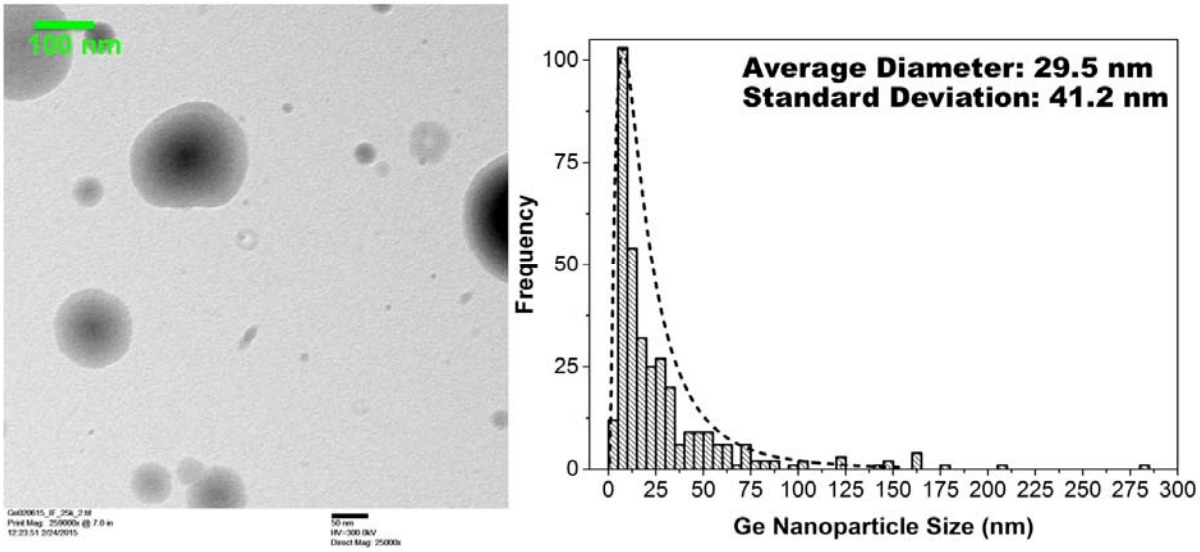

FIGURE 3.6. TEM micrograph (left) of germanium nanoparticles grown with UFPLD at best focus with corresponding particle size distribution (right), with the dash line following a lognormal distribution

With the lens 4.5 cm out of focus (as shown in figure 3.7), the average particle diameter shrinks by a factor of 2.3 to 12.9 nm with a standard deviation of 16.7 nm and an SE of the mean of 0.59 nm. The amount of particles measured was 832. This increase in the number of particles resulted in the decrease of the SE of the mean. The standard deviation is smaller due to a larger amount of smaller clusters with respect to larger particles (> 100 nm). The throughput of nanoparticles is almost 8 times higher when the lens is 4.5 cm out of focus than at best focus. When comparing the number of measured particles, three TEM micrographs were used to measure 349 particles for the samples deposited at best focus while only one TEM micrograph was required to capture 832 particles. Going back to figure 3.2, when the focusing lens was

sufficiently out of focus, the spectrum looked continuous, indicating a collection of hot bodies rather than a plume consisting of purely atomized species.

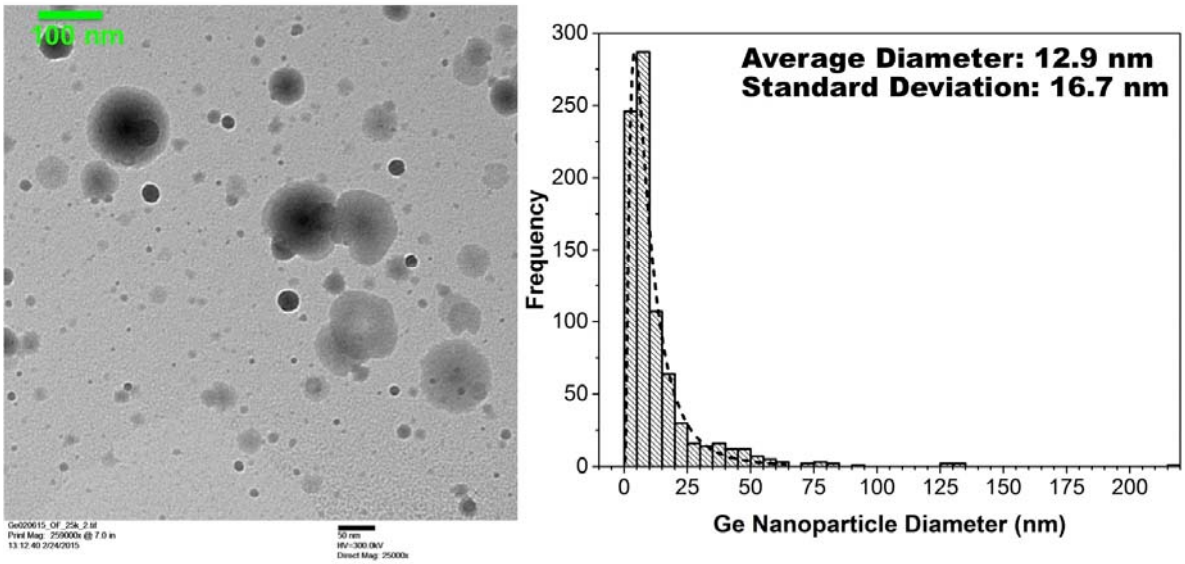

FIGURE 3.7. TEM micrograph (left) of germanium nanoparticles grown with UFPLD with the focus lens 4.5 cm from best focus with corresponding particle size distribution (right) with the dash line following a lognormal distribution

Similarly with silicon, the particle size distribution follows a lognormal distribution and has a larger average diameter and wider standard deviation at best focus compared to the focusing lens being 4.5 cm out of focus. At best focus (as seen in figure 3.8), the average, standard deviation, and SE of the mean are 19.7 nm, 27.3 nm, and 1.08 nm, respectively. At 4.5 cm out of focus (as seen in figure 3.9), the average, standard deviation, and SE of the mean are 9.8 nm, 13.4 nm, and 0.51 nm, respectively.

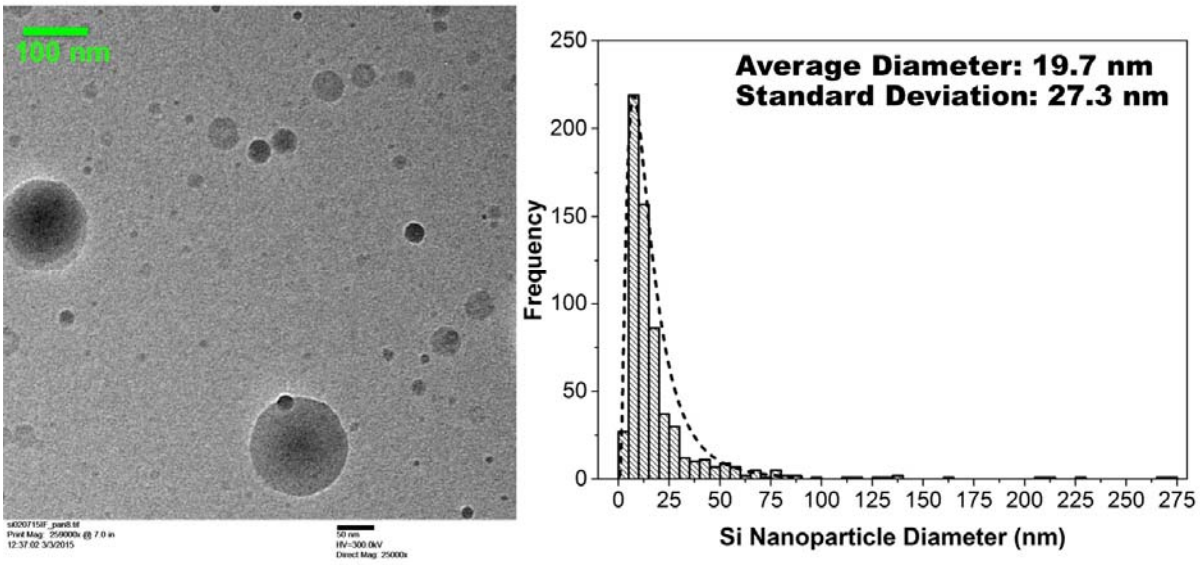

FIGURE 3.8. TEM micrograph (left) of silicon nanoparticles grown with UFPLD at best focus with corresponding particle size distribution (right) with the dash line following a lognormal distribution

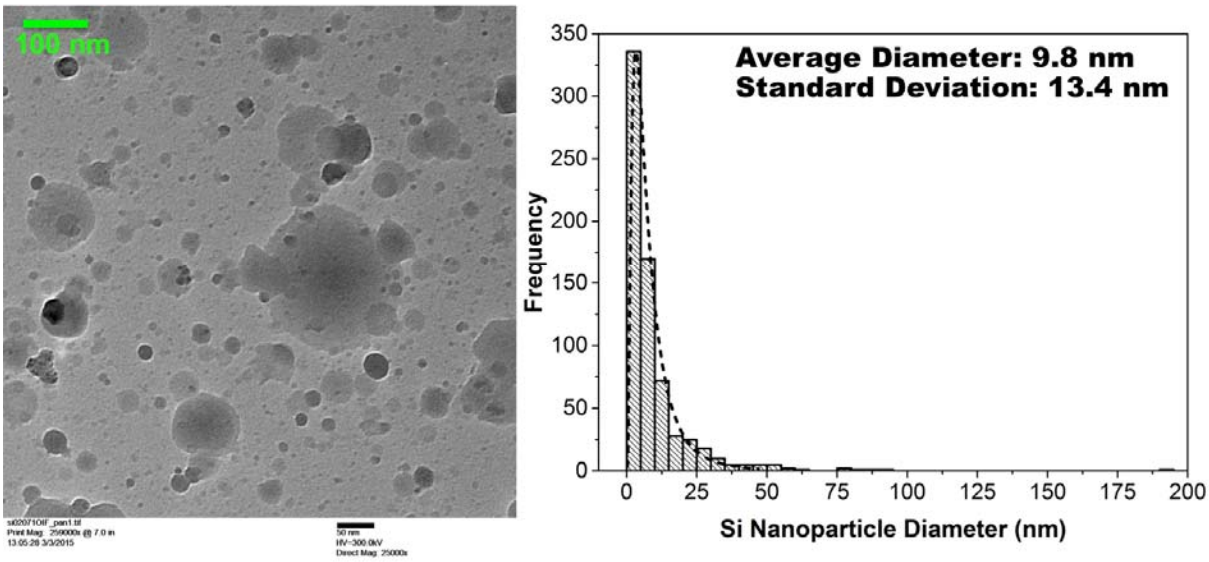

FIGURE 3.9. TEM micrograph (left) of silicon nanoparticles grown with UFPLD with the focus lens 4.5 cm from best focus with corresponding particle size distribution (right) with the dash line following a lognormal distribution

The trend is that lower fluences can be more conducive to nanoparticle growth, while at higher fluences, there would be less nanoparticle throughput with an increasing number of larger particles. This agrees with previous work identifying fluence regimes for nanoparticle

generation at smaller fluences and larger droplets at higher fluences [5]. Clearly, what we observe here is evidence for an optimum cooling rate such that the condensation of nanoparticles is maximized before the plasma plume reaches the substrate. If the initial temperature is too high, then most of the plasma is still in the vapor phase when it reaches the substrate.

AFM measurements provide height information in addition to measurements of the lateral dimensions. Figure 3.10 shows AFM images for both silicon (a) and germanium (b) grown at the higher intensity of 6.5 x 10^{14} W/cm^2 and a fluence of 98 J/cm^2. At this fluence, both the silicon and germanium sample show larger particles with a ring-like structure compared to the lower intensities and fluences above. In figure 3.10b, there is a feature that looks more like a droplet of molten germanium splashed onto the substrate. These types of large, molten droplets may be attributed to target stress confinement at such a high fluence [5, 10]. The evidence for molten droplets also indicates that the initial temperature of the plasma was so high that the droplets that condensed from it are still in the liquid phase when they arrive at the substrate rather than being solid condensates. With plume temperatures inferred from the black-body spectrum as high as 5000K, several cm from the laser target, it is not surprising that some of the nanoparticles are still liquid on arrival at the substrate.

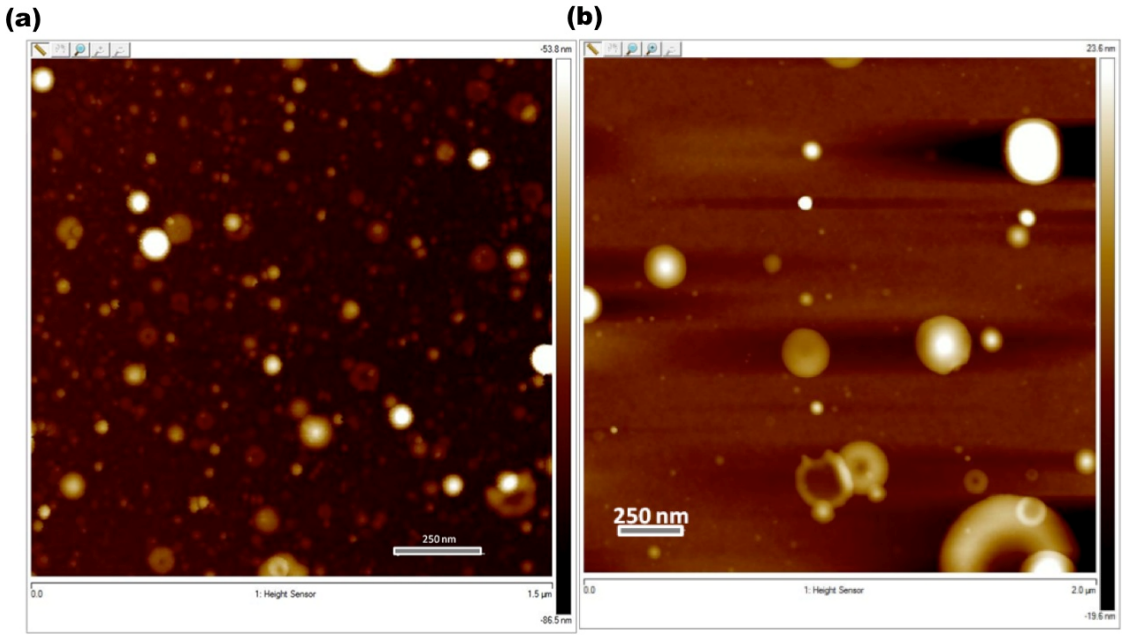

FIGURE 3.10. AFM micrograph of silicon (a) and germanium (b) nanoparticles deposited on glass using UFPLD at an intensity of 6.5 x 10^{14} W/cm^2 and a fluence of 98 J/cm^2

Measuring the height profiles with AFM revealed another interesting observation that the semiconductor nanoparticles are not spherical when deposited on the substrate, but rather are shaped more like platelets [1], as seen in figure 3.11. These type of oblate spheroid shapes has been seen in silicon and nickel in other previous work [4]. These may be attributed to particles that have not completely cooled and are slightly molten when reaching the substrate, akin to the pattern a raindrop makes when it splashes on a car windshield.

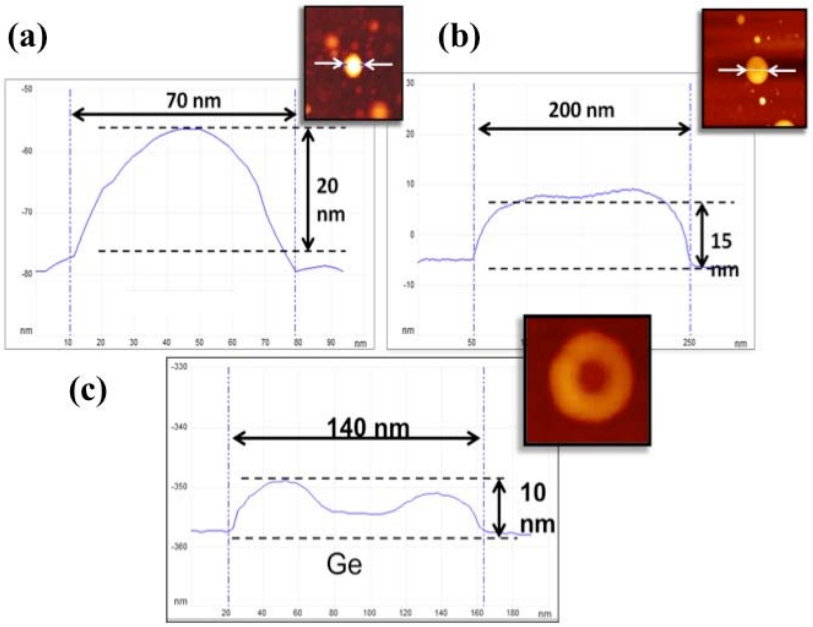

FIGURE 3.11. AFM height cross-sections for (a) silicon (b) germanium (c) ring-shaped germanium particle demonstrating an oblate spheroid-like shape

When the nanoparticles are allowed to collect on a substrate, a quasi-continuous film can be said to form on any given substrate. Since this process is not epitaxial, but rather a coating technique, these nanoparticles can be coated on any surface. The overall morphology of the resulting thin film appears to consist of a collection of nanoparticles that agglomerate into larger structures giving a seemingly fractal morphology. Each sample was deposited at different substrate temperatures for 3 hours. Figure 3.12 shows the morphology of germanium deposited on 25 x 25 x 1mm quartz substrate kept at room temperature (no heating). Figure 3.13-14 show the morphology of germanium films deposited at substrate temperatures of 250^{o} and 500^{o} C, respectively. The finer details begin to blur into the larger agglomerate structures, this may be attributed to a slight sintering effect as the smallest of particles are being absorbed into larger structures.

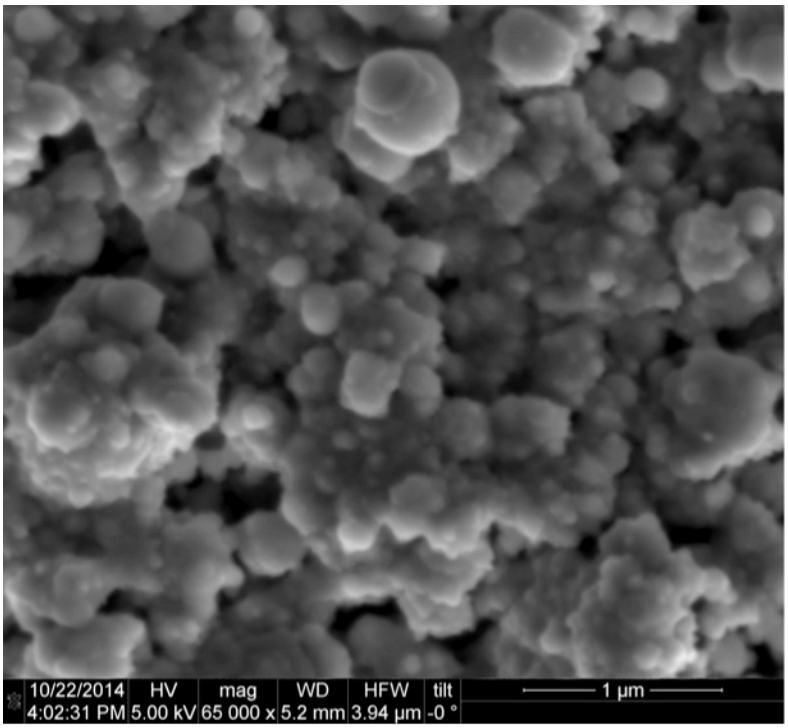

FIGURE 3.12. SEM micrograph of a germanium nanoparticle thin film grown with UFPLD at best focus with the substrate kept room temperature

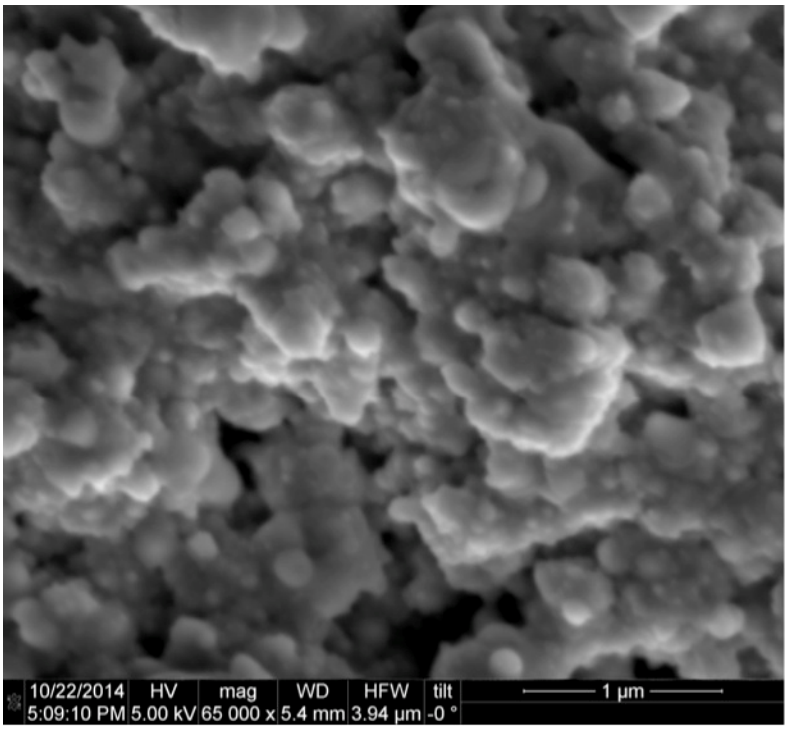

FIGURE 3.13. SEM micrograph of a germanium nanoparticle thin film grown with UFPLD at best focus with a substrate temperature of 250^{o} C

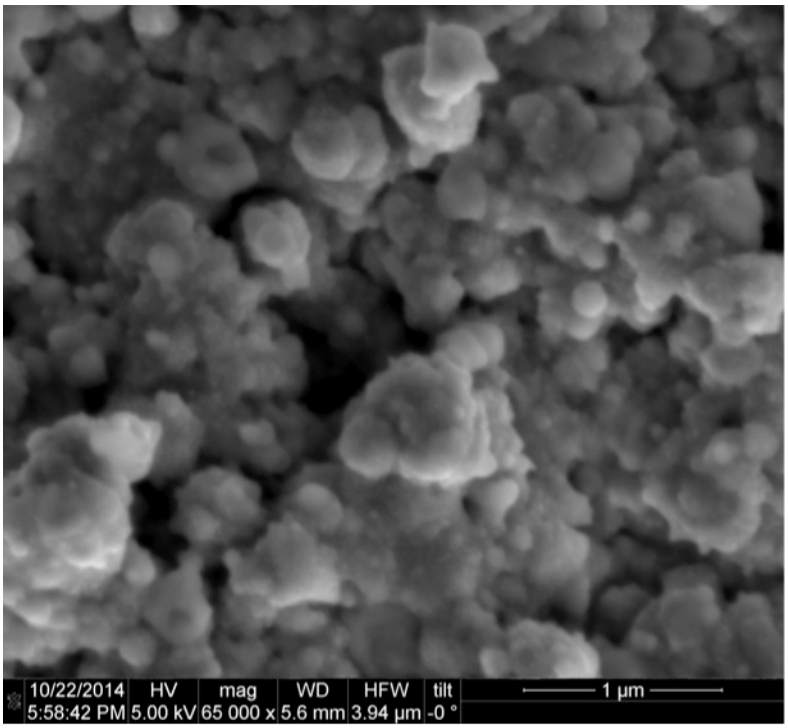

FIGURE 3.14. SEM micrograph of a germanium nanoparticle thin film grown with UFPLD at best focus with a substrate temperature of 500^{o} C

At the higher fluence of 98 J/cm^2 (intensity of 6.5 x 10^{14} W/cm^2), the film morphology appears more continuous, as seen in figure 3.15. This may be due to having larger droplets (as seen in figure 3.10b) that begin to sinter at the higher substrate temperature of 450^{o} C.

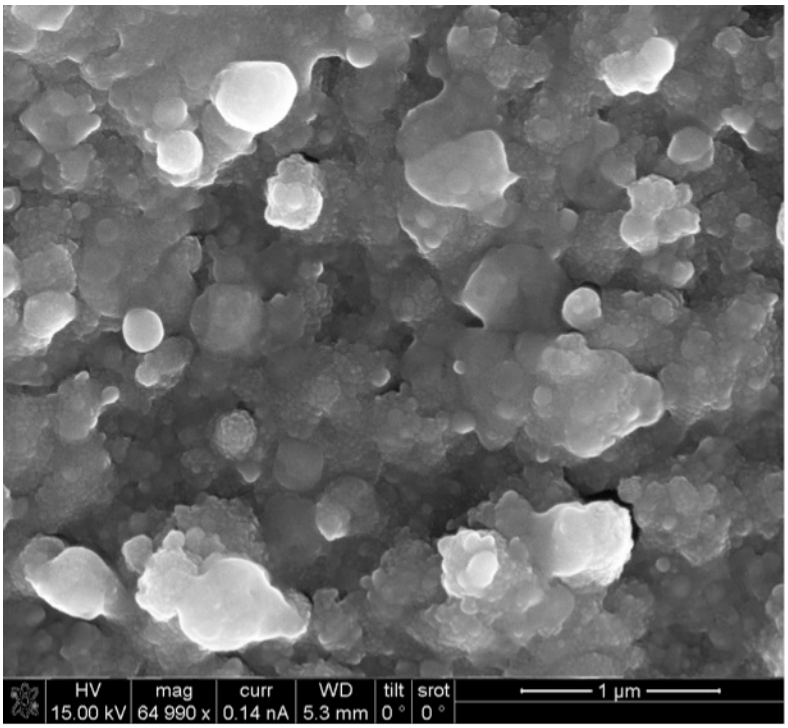

FIGURE 3.15. SEM micrograph of a germanium nanoparticle thin film grown with UFPLD at a higher intensity of 6.5 x 10^{14} W/cm^2 and fluence of 98 J/cm^2 with a substrate temperature of 450^o C

A similar morphology of nanoparticles agglomerating into larger structures is seen with silicon nanoparticle thin films. Figures 3.16-18 are SEM images taken of silicon nanoparticle films deposited at substrate temperatures of room temperature, 400^o C, and 650^o C at a fluence of 3.94 J/cm^2 and a laser spot intensity of 2.62 x 10^{13} W/cm^2. Again, as substrate temperature increases, smaller features appear to blend into the larger structures, which indicate sintering of the nanoparticles.

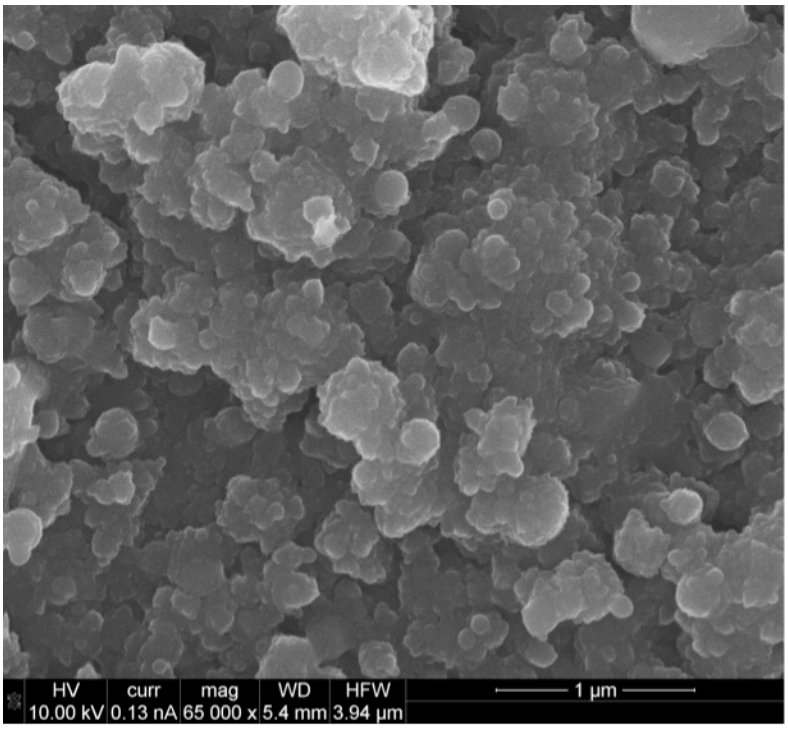

FIGURE 3.16. SEM micrograph of a silicon nanoparticle thin film grown with UFPLD at best focus with the substrate kept room temperature

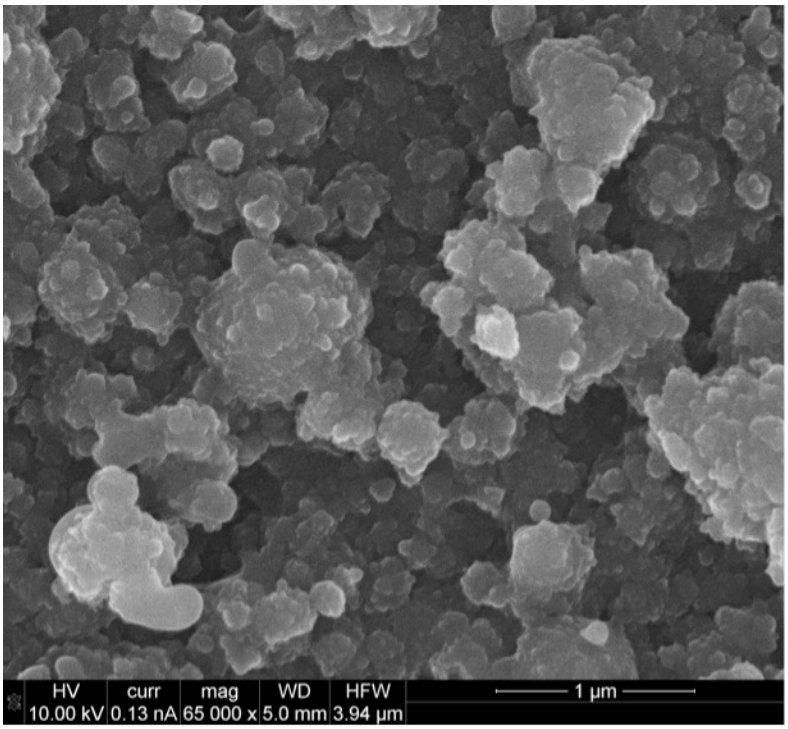

FIGURE 3.17. SEM micrograph of a silicon nanoparticle thin film grown with UFPLD at best focus with a substrate temperature of 400^{o} C

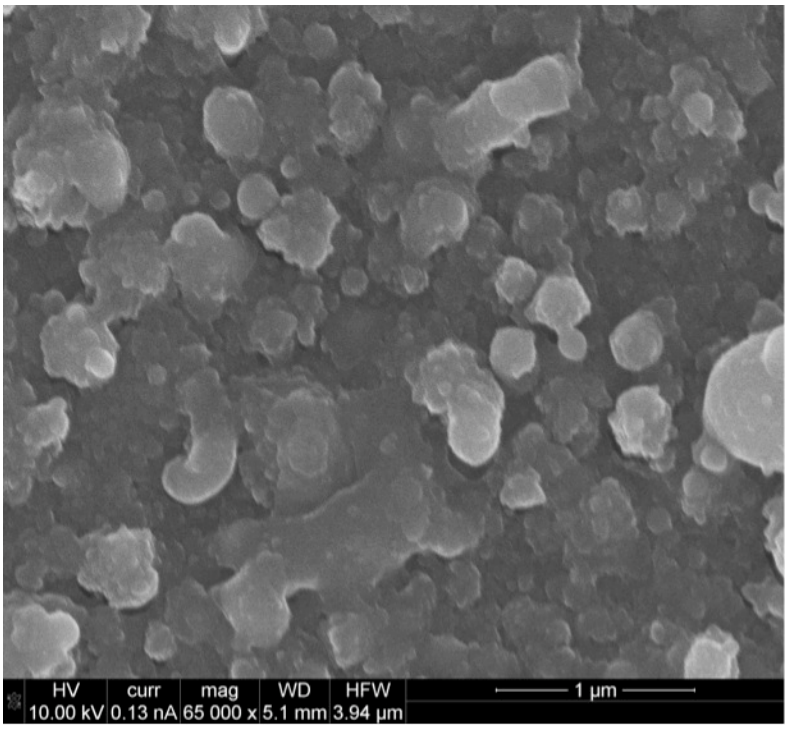

FIGURE 3.18. SEM micrograph of a silicon nanoparticle thin film grown with UFPLD at best focus with a substrate temperature of 650^{o} C

3.4 Crystal Structure

To primary tool to measure the crystal structure of the nanoparticle thin films is x-ray diffraction (XRD). Figure 3.19 shows an earlier 2Theta scan of germanium nanoparticles deposited on glass at various substrate temperatures at a laser focus intensity of 6.5 x 10^{14} W/cm^2 and a fluence of 98 J/cm^2 [1].

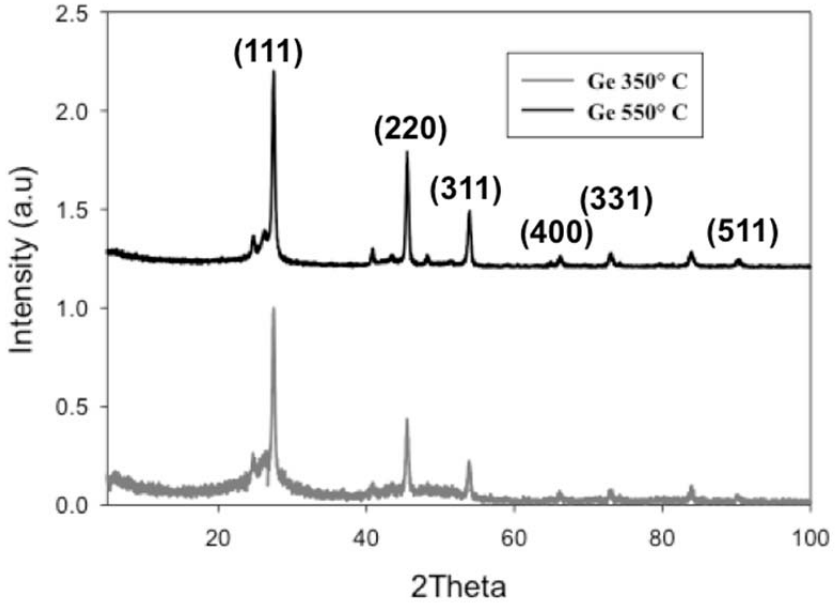

FIGURE 3.19. XRD scans of two germanium samples, one deposited at a substrate temperature of 350^{o} C and the other kept at 650^{o} C

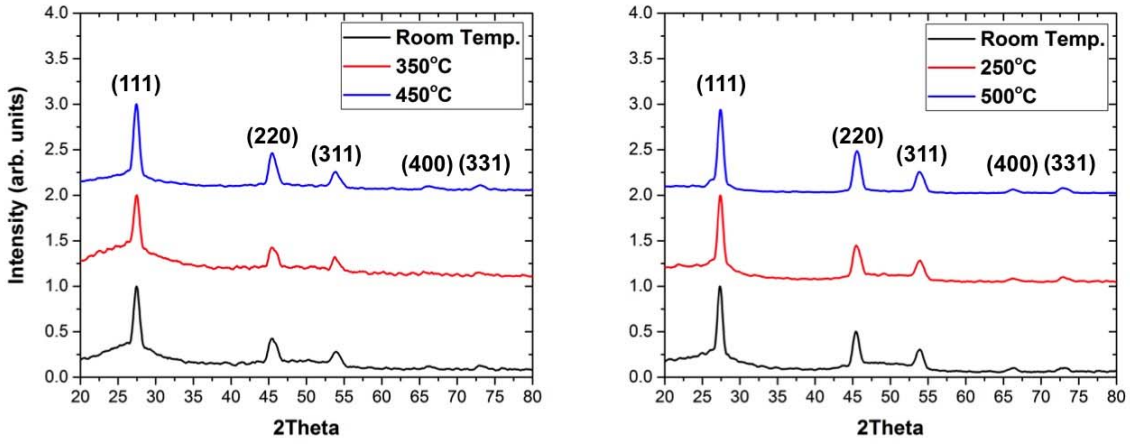

FIGURE 3.20. XRD scans of two sets of germanium samples, (left) deposited at a laser fluence of 98 J/cm^2 with an intensity of 6.5 x 10^{14} W/cm^2 and (right) deposited at 3.94 J/cm^2 and 2.62 x 10^{13} W/cm^2 at various substrate temperatures

Figure 3.20 shows an XRD 2Theta scan of germanium nanoparticle thin films on glass and two different fluence regimes deposited at various substrate temperatures. For the higher

fluence samples, the substrate temperatures were room temperature, 350^{o} C, and 500^{o} C. For the lower fluence samples, the temperatures were room temperature, 250^{o} C, and 500^{o} C. The XRD pattern at room temperature is a combination of an amorphous signal and a crystalline signal. One explanation is the amorphous character seen at room temperature is from the larger droplets formed during ablation that is molten or close to the melting temperature. When they hit the colder substrate, they are quenched into an amorphous state, as evidenced by the diffuse, continuous x-ray scattering background seen in Fig. 3.20. The smaller nanoparticles that condense in the plume are crystalline. As the substrate is held at a higher temperature, annealing begins to take place and the larger droplets begin to crystallize. When the laser spot is at the higher intensity of 6.5 x 10^{14} W/cm^2 and a fluence of 98 J/cm^2, this amorphous behavior is still seen when the substrate is held at 350^{o} C. At 250^{o} C with the sample deposited at a lower fluence (3.94 J/cm^2), this amorphous behavior is less evident in the XRD plot, indicating a higher concentration of crystalline nanoparticles relative to larger droplets. Again, this points towards a fluence dependence on the composition of what type of particles are in the plume, lower fluence regimes are predominately nanoparticles and higher fluences contain larger droplets in addition to nanoparticles [5].

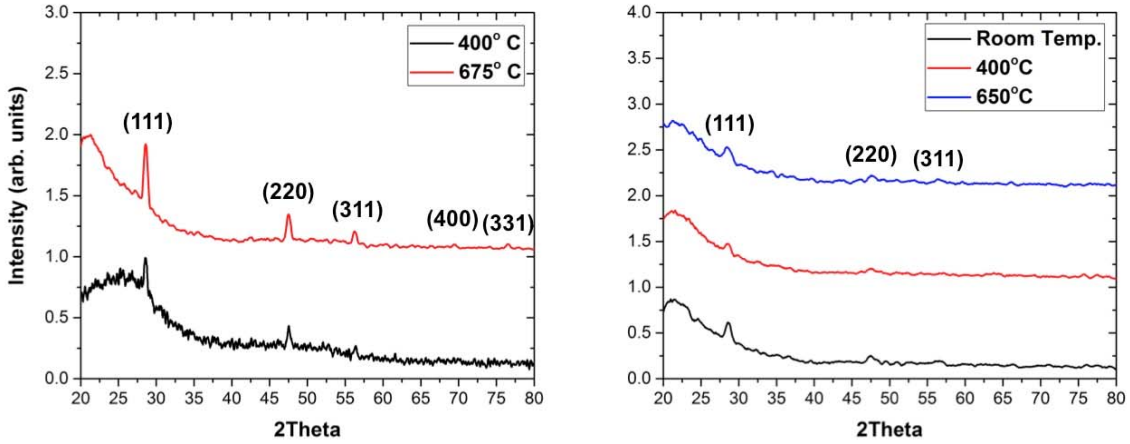

FIGURE 3.21. XRD scans of two sets of silicon samples, (left) deposited at a laser fluence of 98 J/cm^2 with an intensity of 6.5 x 10^{14} W/cm^2 and (right) deposited at 3.94 J/cm^2 and 2.62 x 10^{13} W/cm^2 at various substrate temperatures

Figure 3.21 shows a similar comparison with silicon, which at the conditions presented, the same conclusion cannot be drawn since both films show amorphous character at all substrate temperatures at both fluences. With the higher fluence case, as the substrate temperature increases, the Bragg peaks increase relative to the signal background due to annealing. A higher substrate temperature is required compared to germanium due to the higher melting point of silicon, 1412^o C compared to germanium's melting point of 937^o C [11].

3.5 Transmission Spectrum

The average size of germanium nanoparticles in a nanoparticle film deposited at a fluence of 3.94 J/cm^2 and a laser intensity of 2.62 x 10^{13} W/cm^2 has an average particle diameter of 29.5 nm with the histogram peak being centered between 5 and 10 nm. Since the Bohr exciton radius of germanium is 24.3 nm [12], particles around this size should start to experience a blue shift in the band gap of germanium due to quantum confinement. Even the samples with larger droplets that are deposited at the higher fluence of 98 J/cm^2 should exhibit confinement effects due to the

oblate spheroid geometry with heights on the order of the Bohr exciton radius (as shown in figure 3.11).

Figure 3.22 shows a comparison of the transmission spectrum between bulk germanium and a nanoparticle thin film deposited on glass at a higher fluence of 98 J/cm^2 and intensity of 6.5 x 10^{14} W/cm^2 at substrate temperatures of 350^o and 550^o C. This spectrum was obtained using optical spectroscopy with a continuous (incandescent) light source having a blackbody spectrum of 3200 K and a fiber coupled spectrometer with an InGaAs detector, (further details are in chapter 2). Due to the limited spectral range of the InGaAs detector, the direct gap region of germanium, 0.8 eV [11], could be measured. The germanium nanoparticle films deposited by UFPLD exhibit a shift of the transmission spectrum towards higher energy compared with the direct band edge seen with a germanium wafer. The nanoparticle film deposited with a substrate temperature of 350^o C shows a steeper transmission spectrum edge compared with the sample deposited at 500^o C. This spectral shift may be caused by the band gap increase of germanium nanoparticles due to quantum confinement. Since the entire film is a dense collection of nanoparticles, the film as a whole would have an increase of the band gap, as observed.

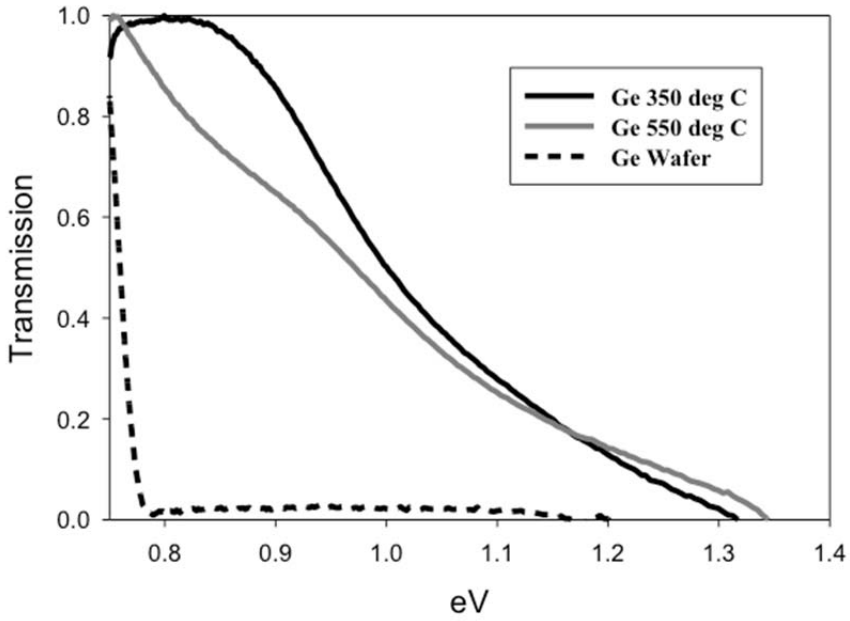

FIGURE 3.22. Transmission spectrum in the range of the germanium direct band gap comparing nanoparticle films deposited at 98 J/cm^2 laser fluence at 350^o C and 550^o C with bulk germanium

This measurement has also been done on a germanium nanoparticle film deposited at 500^o C at a fluence of 3.94 J/cm^2 and an intensity of 2.62 x 10^{13} W/cm^2. The spectrum, as shown in figure 3.23, was acquired using an FTIR (further details outlined in chapter 2) to capture the indirect band gap of germanium, 0.66 eV [11], which is deeper in the infrared. At energies less than 0.7 eV, there is some absorption from the thin (400 ± 50 nm) UFPLD germanium sample where the thicker (500 μm) bulk germanium wafer was transparent. This indicates there are additional energy states within the band gap of our nanoparticle germanium films. All spectra were obtained at room temperature.

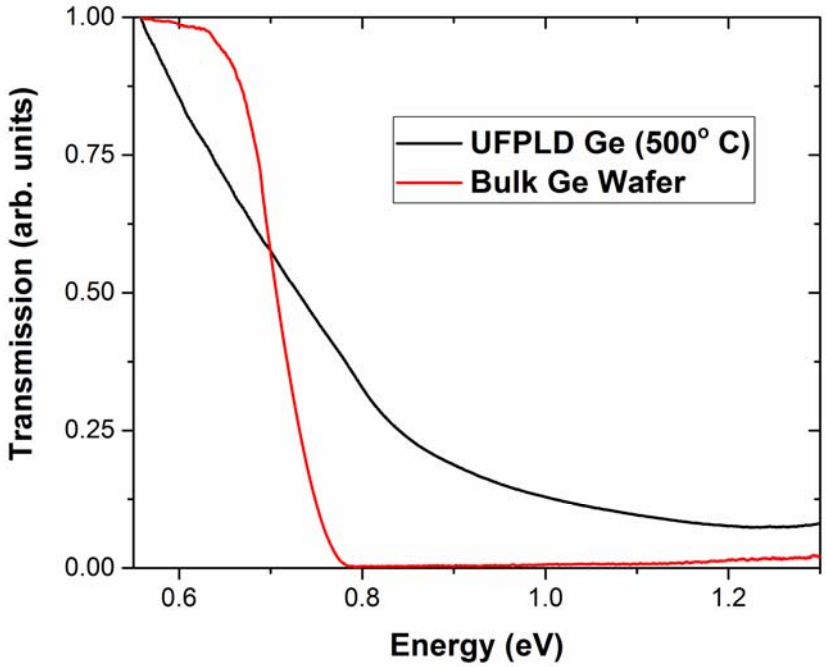

FIGURE 3.23. Transmission spectrum in the range of the indirect band gap of germanium comparing nanoparticle thin film deposited at a laser fluence of 3.94 J/cm^2 with a substrate temperature of 500^o C with bulk germanium

3.6 Photoluminescence

Though the average diameter of the germanium nanoparticles in our films is smaller than the Bohr exciton radius, attempts at detecting photoluminescence were not successful. One explanation is that the nanoparticle films consist of uncapped quantum dots which host non-radiative recombination sites at nanoparticle surfaces (due to dangling bonds, etc.). Previous work observing significant blue shifts of photoluminescence signals in germanium consisted of nanocrystals embedded in a SiO_2 matrix [12-15].

3.7 Raman Spectroscopy

All Raman measurements were taken at room temperature and an excitation wavelength of 633 nm. The UFPLD deposited nanoparticle thin films exhibit a shift towards the left (smaller

Raman shifts) of the bulk peak. Raman spectroscopy is sensitive to local atomic arrangements and vibrations within a crystal and a phonon confinement model can be used to characterize and interpret semiconductor nanostructures [16]. The model was initially proposed by Richter, Wang, and Ley [17] has been found to be useful to account for peak-position shift. The change in Raman shift as a function of nanoparticle size is given by equation 3.2 [18]:

$$\Delta\omega = -A\left(\frac{a}{L}\right)^{\gamma} \tag{3.2}$$

where $\Delta\omega$ is the shift in the Raman peak (cm^{-1}), L is the nanoparticle size (nm), and a is the lattice constant (nm). The parameters A and γ are used to describe vibrational confinement in the nanoparticles. In previous work [18], this equation was fitted to fixed silicon spheres and columns sizes to provide the parameter values shown in table 3.3. For the case of Ge nanoparticles, other previous work has been done to refit equation 1 for nanoparticles grown using nanosecond pulsed laser ablation (PLA) in acetone [19]. The refitted parameter values are also shown in table 3.3.

Geometry	**A (cm^{-1})**	**γ**
Spheres	47.41	1.44
Spheres (fitted for PLA Ge NPs)	47.41	1.25
Columns	20.92	1.08

TABLE 3.3. Fitted parameters for equation 3.1 from literature [18,19]

Figure 3.24 are plots showing Raman peak shift, $\Delta\omega$, as a function of particle sizes, L of both silicon and germanium. The column geometries are also investigated due to the spheroid oblate shapes of the UFPLD nanoparticles possibly behaving more like short columns.

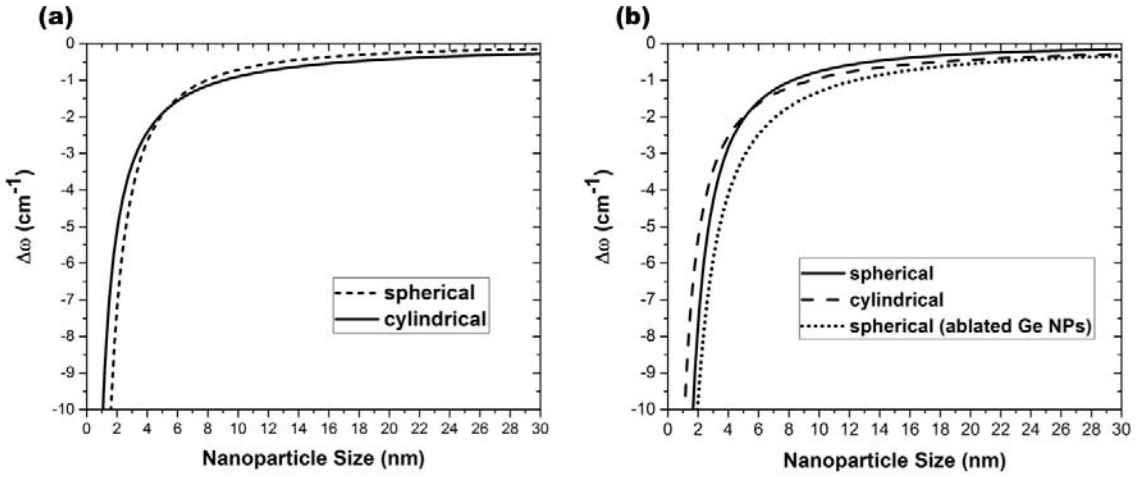

FIGURE 3.24. Plots of Raman peak shifts (Δω) vs. nanoparticle size with different geometries for (left) silicon and (right) germanium, using fitting parameters from past work [18,19]

Figure 3.25 shows the measured Raman spectrum for UFPLD germanium nanoparticle thin films with respect to a bulk Ge reference, centered at 300.8 cm^{-1} corresponding to the LTO phonon at $\Gamma_{25'}$ position at 300 K [11]. A polycrystalline germanium thin film grown on quartz via sputtering is included as another reference point. The broad peaks at the left are due to the amorphous component of germanium and reduce as substrate temperature increases for subsequent samples, confirming XRD analysis for evidence of nanoparticle crystallization from annealing. Figure 3.26 is a zoomed-in view focused around the main peak to highlight peak shifts. The peak shift was the strongest for samples deposited on substrates at room temperature, 250^o, and 400^o C. At the higher substrate temperature of 500^o C, the peak is closer to the bulk, approaching the sputtered film peak position. The reason is diminished phonon confinement, which is strong evidence for sintering of the nanoparticles at higher substrate temperatures, forming a more continuous thin film.

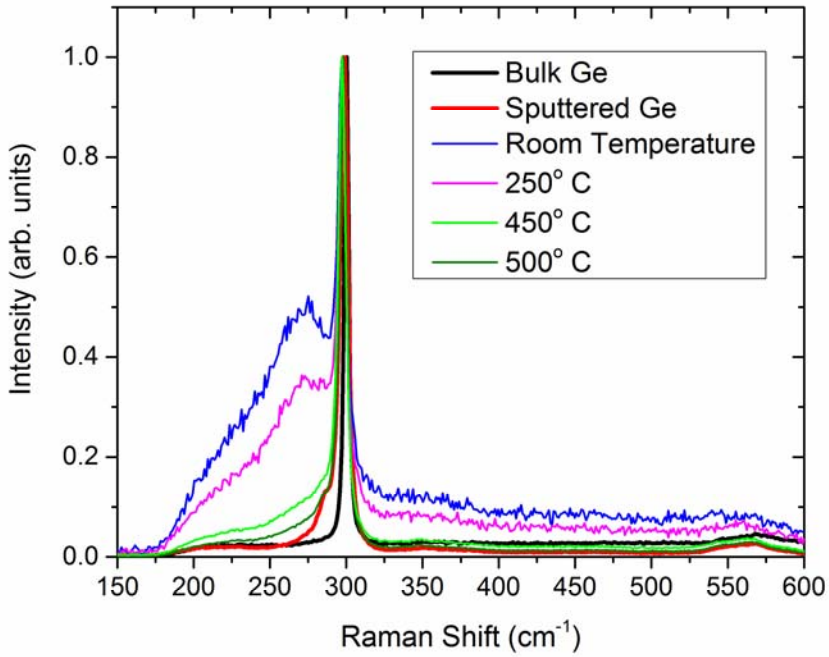

FIGURE 3.25. Raman spectra of various germanium samples including: bulk; sputtered germanium; UFPLD nanoparticle films are deposited at substrate temperatures of room temperature, 250° C, and 500° C; and a UFPLD film deposited at the higher fluence of 98 J/cm^2 and a substrate temperature of 450° C

Table 3.4 lists the Raman peak shift compared to particle size predictions using equation 3.1 with the various fitting parameters outlined in table 3.3 with the measured size distribution from TEM. Though the mean TEM particle diameter is much larger than what is predicted, the size distribution peak (centered between 5 and 10 nm) is more meaningful since more nanoparticles are in that size range where the mean is skewed by the much larger particles which have a much smaller population size. The closest predicted value is 4.8 nm for the spherical geometry with parameters fitted for PLA germanium in acetone, which is within the same order of magnitude and is close to the peak range of 5 – 10 nm. The furthest value is for the column geometry indicating that the particles have more of a spherical character. Table 3.4 lists the values in detail.

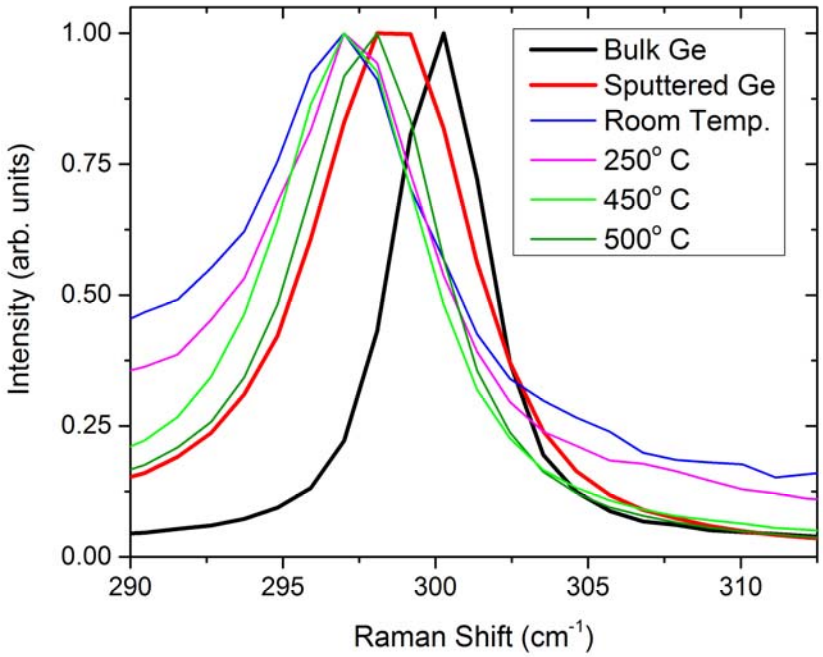

FIGURE 3.26. Zoom in of the main peaks at 300 cm^{-1}

Sample (Ge)	Δω (cm^{-1})	Spheres (nm)	Spheres-Ge NP (nm)	Columns (nm)	TEM Mean (nm)	TEM Histogram Peak (nm)
UFPLD - Rm. Temp.	-3.28	3.6	4.8	3.1	29.5	5-10
UFPLD - 250° C	-3.28	3.6	4.8	3.1	29.5	5-10
UFPLD - 450° C	-3.28	3.6	4.8	3.1	29.5	5-10

TABLE 3.4. Calculated Ge sphere and column diameters from measured Raman peak shifts compared with the nanoparticle diameter mean and the histogram bin range with the largest frequency as measured by TEM

Figure 3.27 shows the measured Raman spectrum for UFPLD silicon nanoparticle thin films with respect to a bulk Si reference, centered at 516.9 cm^{-1} corresponding to the LTO phonon at the $\Gamma_{25'}$ position at 300 K [11]. The broad peaks to the left of the main peak remain for all substrate temperatures measured, indicating the film remains mostly amorphous, which is verified by the XRD data in figure 3.21. Table 3.5 lists the predicted values compared to the

Raman peak shifts, the predictions are within an order of magnitude of the size distribution peak of silicon with the parameters for column geometries being further off, indicating that the particles are closer to being spherical.

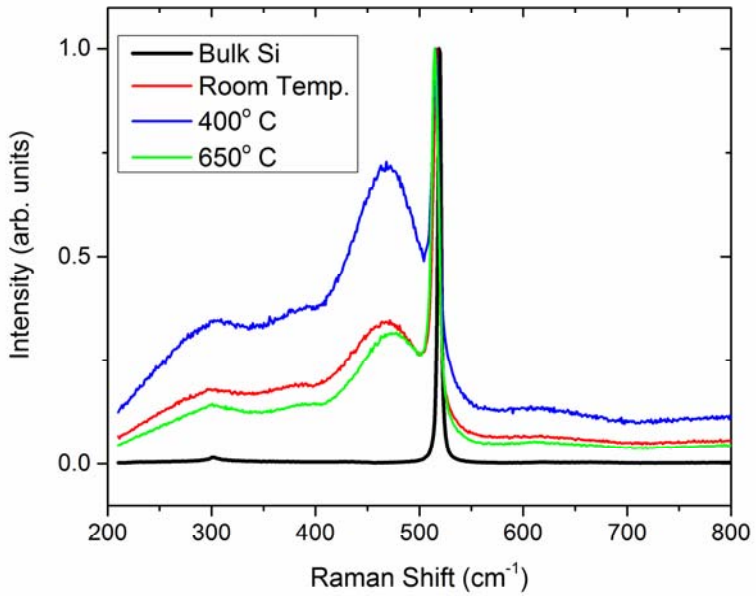

FIGURE 3.27. Raman spectra of various silicon samples including: bulk; UFPLD nanoparticle films deposited at substrate temperatures of room temperature, 400° C, and 650° C

Sample (Si)	Δω (cm^{-1})	Spheres	Columns	TEM Mean (nm)	TEM Histogram Peak (nm)
UFPLD - Rm. Temp.	-3.16	3.6	3.1	19.7	5-10
UFPLD - 400° C	-3.69	3.2	2.7	19.7	5-10
UFPLD - 650° C	-4.74	2.7	2.1	19.7	5-10

TABLE 3.5. Calculated Si sphere and column diameters from measured Raman peak shifts compared with the nanoparticle diameter mean and the histogram bin range with the largest frequency as measured by TEM

3.8 Asynchronous Optical Sampling (ASOPS) of Ge Nanoparticle Thin Films

Pump-probe measurements using ultrafast lasers are used to study laser-induced transient dynamics in solids. ASOPS is used to measure a larger timescale range compared to pump-probe systems using mechanical delay stages [20, 21]. With the current set up, the measurement ranges from picoseconds to nanoseconds, thus dynamics from both time scales are captured in a single measurement. Dual Er-doped fiber lasers are used with a pulse duration of 80 fs, pulse energy of 1.5 nJ, and a fundamental wavelength of 1560 nm. What is being measured is the reflectivity change as a function of time after the sample is perturbed by the pump laser. This can give insight into various transient effects taking place in the material, such as carrier generation and phonon effects [21, 22]. The sample set includes several UFPLD germanium nanoparticle thin films grown at various substrate temperatures and at two different fluences with a bulk Ge wafer and a polycrystalline Ge thin film grown on quartz using sputtering (substrate heated to 500^{o} C) as a reference signal. The two main fluencies used for nanoparticle deposition are 3.94 and 98 J/cm^2 and substrate temperature ranges from room temperature to 500^{o} C.

The following figures show the reflectivity change as a function of time with emphasis on various time scales of interest. Figure 3.28 shows a bulk Ge sample used as a reference to compare relaxation times. Figure 3.29 shows a thin film of sputtered polycrystalline Ge for a thin film reference. There are oscillating features, which are captured in figure 3.29(c) that show a coarse period of 1.63×10^{-10} s and a fine period of 1.78×10^{-11} s. Since these time oscillations carry on into the nanosecond time scale, they may be attributed to lattice vibration (phonons) reflections. Taking the speed of sound in germanium to be 5.36×10^{12} nm/s [11], the coarse structure time period corresponds to 682 nm of total distance traveled or 341 nm features which may be from the thickness of the thin film (the film is labeled as being 500 nm thick, but may not

have had uniform thickness). The vibrations travel through the thin film and are reflected back normal to the substrate. In the literature [23], these fine oscillations have been attributed to phonon modes. Converting the fine time period into a frequency leads to a frequency 5.6 x 10^{-10} Hz, which is smaller than LO phonon modes by two orders of magnitude (9.16 and 8.94 THz) [23]. Therefore we believe a more reasonable interpretation of these oscillations is in terms of transit time across the width of the nanostructure. In this interpretation, the fine structure time period corresponds to 95 nm traveled, or 47.5 nm feature, possibly being a grain boundary.

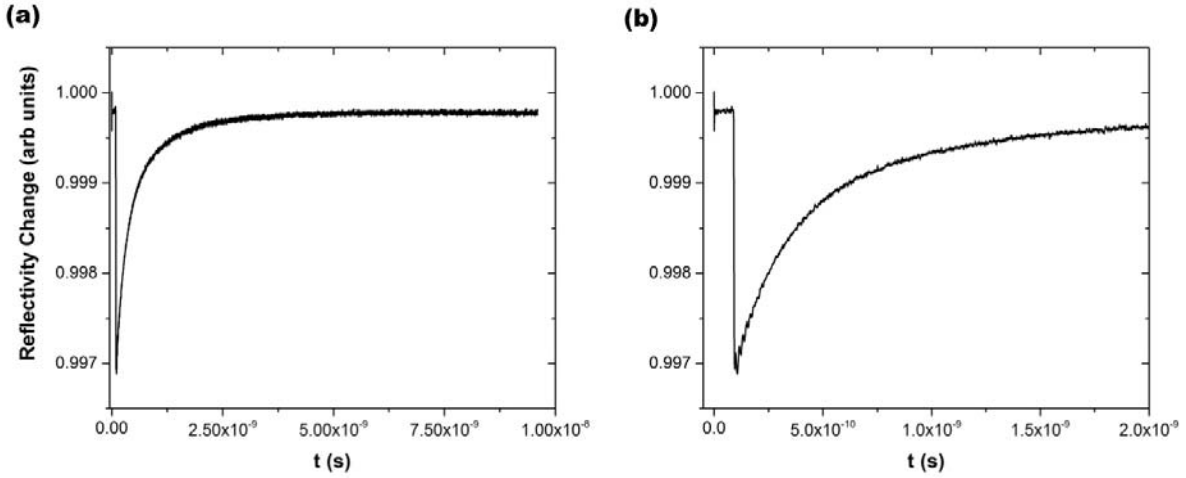

FIGURE 3.28. Reflectivity change as a function of time for bulk Ge, (a) shows the entire pump/probe scan and (b) is zoomed into the relaxation time scale

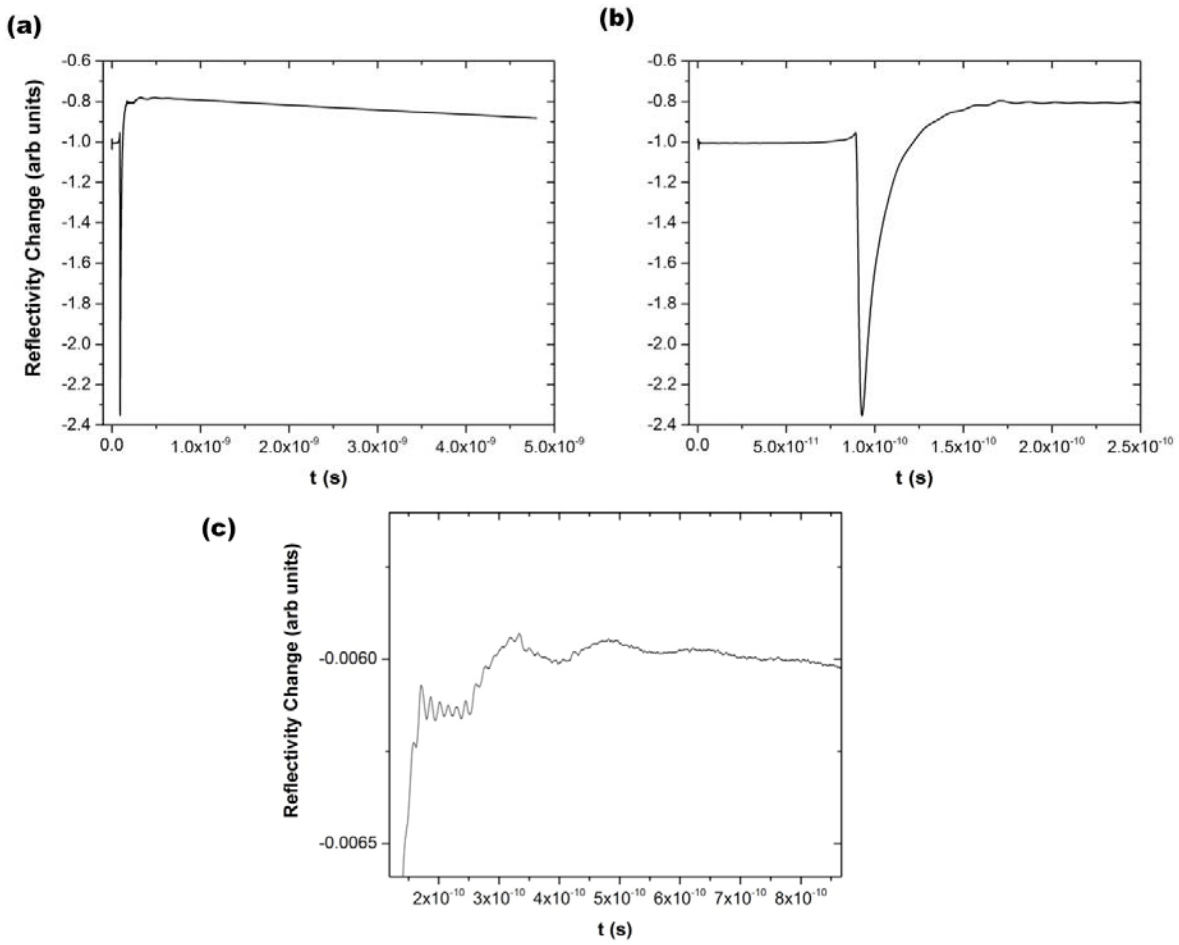

FIGURE 3.29. Reflectivity change as a function of time for sputtered Ge, (a) shows the entire pump/probe scan, (b) is zoomed into the relaxation time scale, and (c) zoomed into the scale showing the small oscillations

Figure 3.30 and 3.31 show UFPLD Ge nanoparticle films deposited at a fluence of 3.94 J/cm^2 at room temperature and at a substrate temperature of 250^o C, respectively. Oscillatory behavior is observed in both, with the more apparent oscillation at the room temperature sample. The signals were too noisy to pick out any fine oscillation but the time periods of the damped, coarse structure are measured to be 5.2 x 10^{-10} and 2.68 x 10^{-10} s, respectively. This translates into a reflection from a boundary that has a size of about 1,400 nm and 720 nm, which is much larger than the film thicknesses, which range between 300 – 400 nm, most likely indicating lateral vibrational modes of loosely bound nanoparticles.

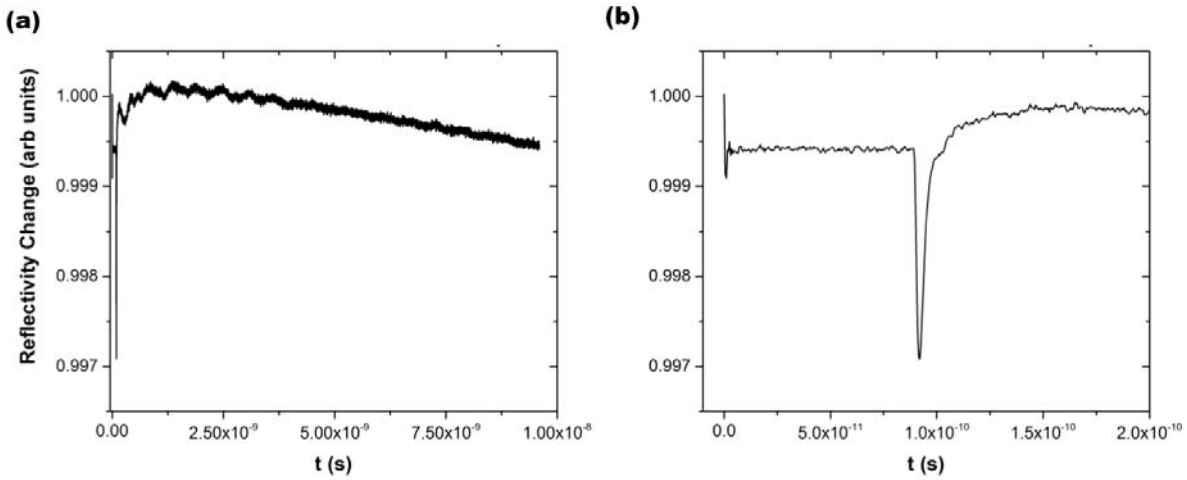

FIGURE 3.30. Reflectivity change as a function of time for UFPLD Ge nanoparticle film deposited at a fluence of 3.94 J/cm^2 with the substrate held at room temperature, (a) shows the entire pump/probe scan and (b) is zoomed into the relaxation time scale

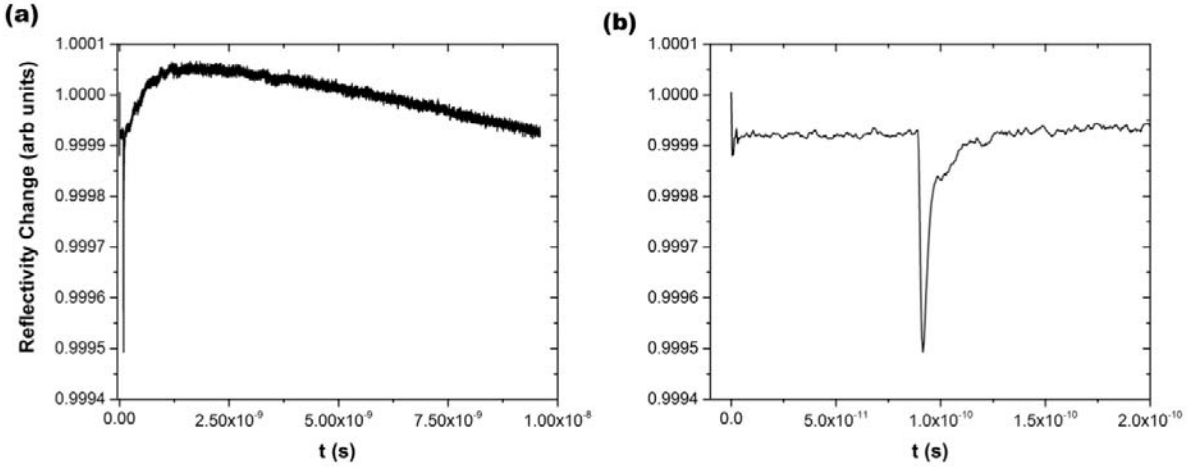

FIGURE 3.31. Reflectivity change as a function of time for UFPLD Ge nanoparticle film deposited at a fluence of 3.94 J/cm^2 with the substrate temperature of 250^o C, (a) shows the entire pump/probe scan and (b) is zoomed into the relaxation time scale

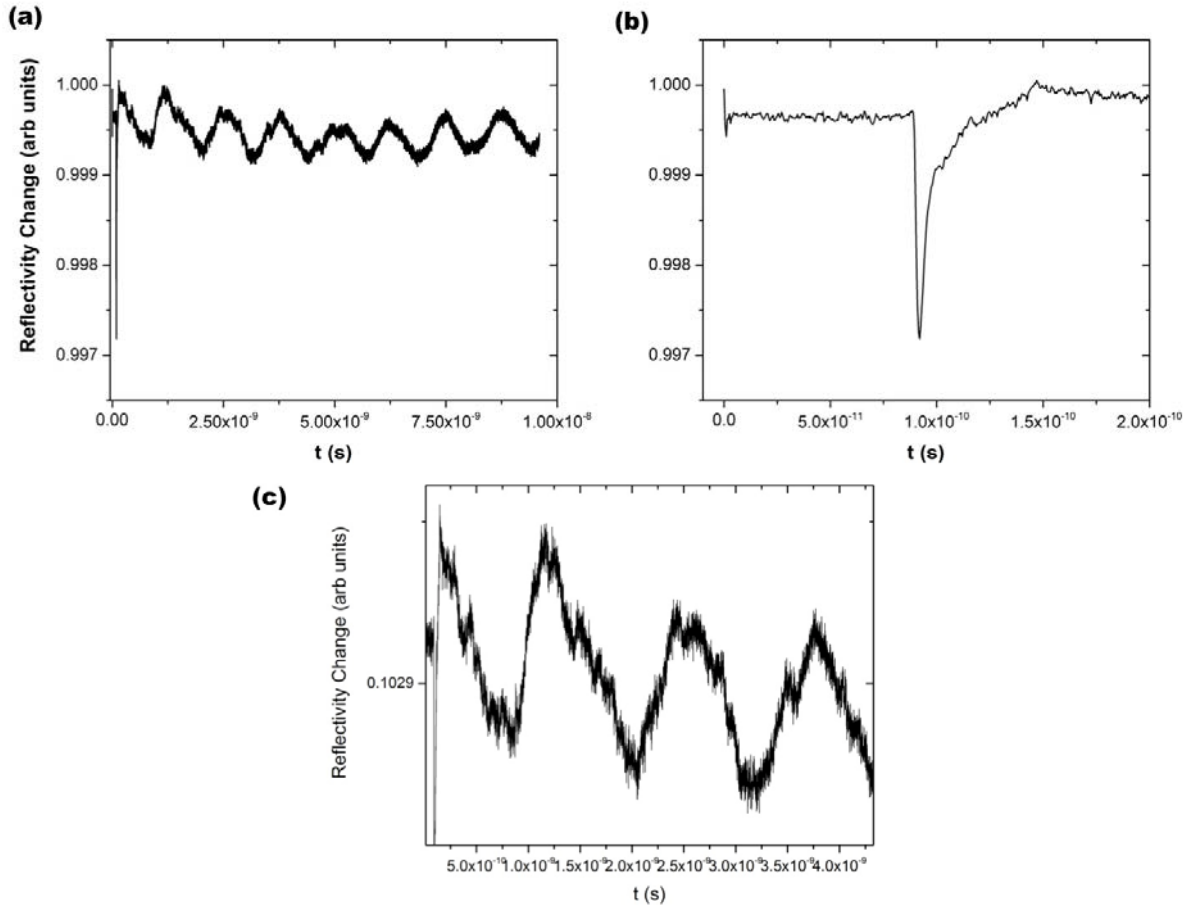

FIGURE 3.32. Reflectivity change as a function of time for UFPLD Ge nanoparticle film deposited at a fluence of 3.94 J/cm^2 with the substrate temperature of 500^o C, (a) shows the entire pump/probe scan, (b) is zoomed into the relaxation time scale, and (c) zoomed into the scale show the small oscillations

Figure 3.32 shows the reflectivity change as a function of time for the UFPLD Ge film deposited with a fluence of 3.94 J/cm^2 and a substrate temperature of 500^o C. This sample is peculiar in a sense that there is a strong oscillation with a period of 1.27 x 10^{-9} s, which is the largest period of all of the samples measured and this oscillation does not dampen over the time of the measurement (which is in between pump pulses). This oscillation corresponds to a feature of 3,400 nm, which again indicates nanoparticle vibrations in the lateral directions. This is the same sample of the SEM micrograph of figure 3.14 that has agglomerates of over 1 micron. At

the high substrate temperature of 500° C, these agglomerates may begin to combine with other agglomerates from sintering (which is also evident in Raman spectroscopy) and may allow the lateral phonons to travel a larger distance before getting reflected. Another explanation is the lateral vibrational reflections are coming from the laser spot size, which is less than 10 microns. Since the nanoparticles are small compared to the laser spot, they can provide an interface at the spot edges, similar to pixels capturing the edge of an image. These postulates still do not address why these large oscillations are not strongly damped. The fine oscillations have a period of 1 x 10^{-10} s.

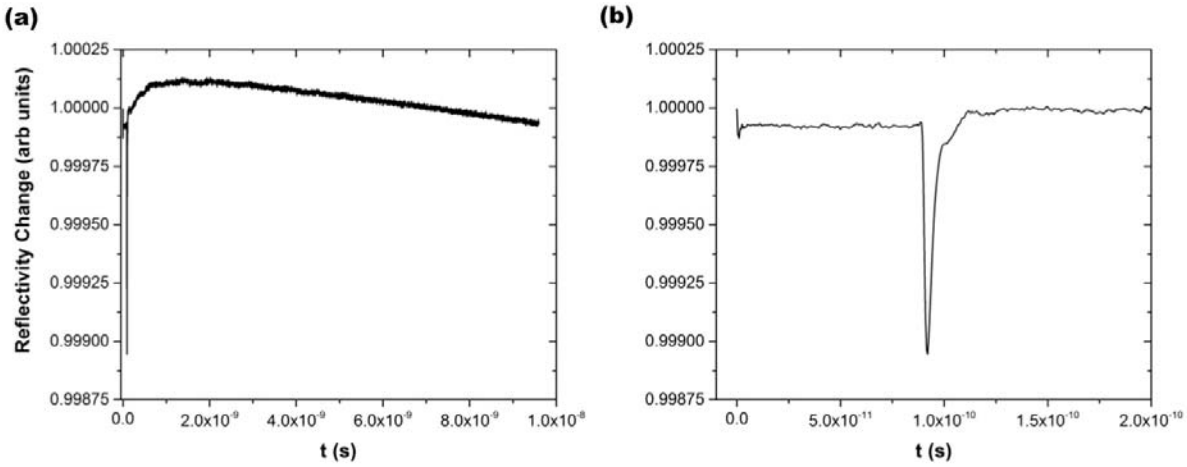

FIGURE 3.33. Reflectivity change as a function of time for UFPLD Ge nanoparticle film deposited at a fluence of 98 J/cm^2 with the substrate temperature of 450°C, (a) shows the entire pump/probe scan and (b) is zoomed into the relaxation time scale

A mean lifetime can be extracted from each nanoparticle film by fitting the data in Figure 3.28 to 3.33 with the simple exponential decay function (equation 3.2),

$$y(t) = y_0 + Ae^{-t/\tau} \tag{3.2}$$

where A and y_0 are constants and τ is the mean lifetime, which are shown in table 3.6 for each germanium sample, with a bulk Ge wafer and a polycrystalline Ge thin film on quartz as reference.

Sample (Ge)	**τ (s)**	**R^2**
Bulk	4.94×10^{-10}	0.982
Sputtered Thin Film	1.40×10^{-11}	0.993
UFPLD - Rm. Temp.	4.88×10^{-12}	0.969
UFPLD - 250° C	4.67×10^{-12}	0.941
UFPLD - 500° C	8.94×10^{-12}	0.944
UFPLD - 450° C (higher fluence)	3.70×10^{-12}	0.987

TABLE 3.6. Fitted mean lifetimes with corresponding R^2 values for each Ge sample

The reflectivity change at the shorter timescales may be related to carrier lifetimes at the surface of the measured sample. By comparing to the germanium wafer (bulk), the relative differences between carrier lifetimes can be identified. Relative to bulk germanium, the measured mean lifetime of the sputtered sample is an order of magnitude smaller and all of the nanoparticle thin films deposited by UFPLD are two orders of magnitude smaller than bulk. Between the samples deposited at a fluence of 3.94 J/cm^2, there is a trend of increasing mean lifetimes with increasing substrate temperatures. The sample deposited at the higher fluence of 98 J/cm^2 had an even shorter mean lifetime compared to samples grown at the lower fluence, though all are within the same order of magnitude. This shorter lifetime compared to bulk and sputtered Ge is attributed to surface recombination sites. For example, silicon photodetectors have short carrier lifetimes in the UV range due to the absorption depth being shallow and close to surface recombination sites [24]. The nanoparticle thin films appear to be mostly surface.

3.9 Transport

Transport measurements were made by the Kurdak group in the Physics Department at the University of Michigan. Two germanium nanoparticle film samples prepared by UFPLD were measured; one deposited at a substrate temperature of 450^{o} and the other at 550^{o} C at a fluence of 98 J/cm^{2} and an intensity of 6.5 x 10^{14} W/cm^{2}. This experiment was done to determine that the UFPLD nanoparticle films could act as an electrically continuous thin film. Figure 3.34 shows the mobility between the two Ge nanoparticle films as a function of temperature. There is a strong dependence of substrate temperature, the increase from 450^{o} to 550^{o} C resulted in an increase of almost 5 times at 5.2 K and almost 3 times larger at 269 K. A combination of further crystallization and sintering of the nanoparticles can explain this. The majority carriers are holes, as seen in figure 3.37 with a positive 2D Hall coefficient. This mobility is small compared to the bulk value for Ge of 1900 cm^{2}/Vs for holes [11] but is competitive with other thin film technologies, such as amorphous silicon with a hole mobility of around 5 x 10^{-4} cm^{2}/Vs [25], cadmium telluride thin films with a hole mobility of about 30 cm^{2}/Vs [26], organic semiconducting thin films with a mobility of about 9 x 10^{-2} cm^{2}/Vs [27], and orders of magnitude higher than colloidal quantum dot thin films [24].

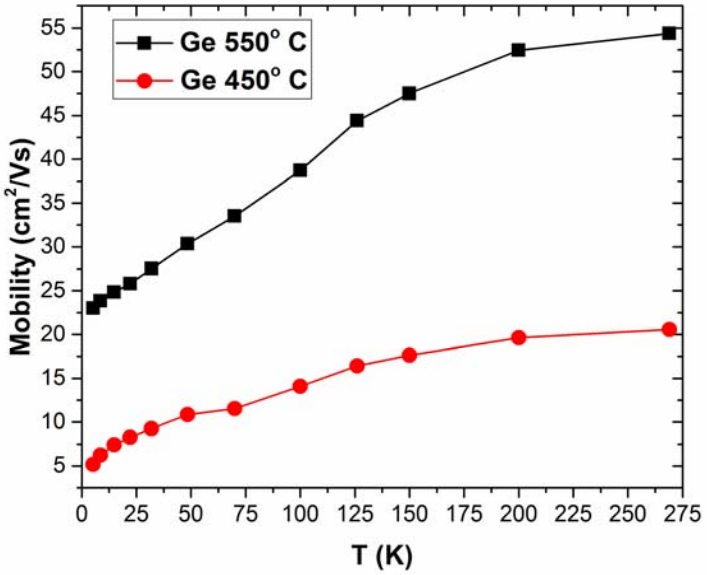

FIGURE 3.34. Mobility of the UFPLD Ge nanoparticle thin films deposited with a fluence of 98 J/cm^2 at substrate temperatures of 450^o and 550^o C

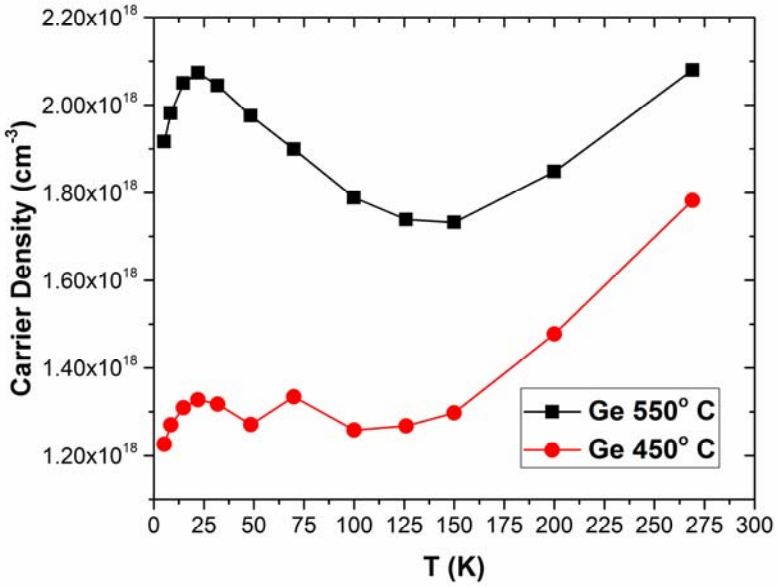

FIGURE 3.35. Carrier density of the UFPLD Ge nanoparticle thin films deposited with a fluence of 98 J/cm^2 at substrate temperatures of 450^o and 550^o C

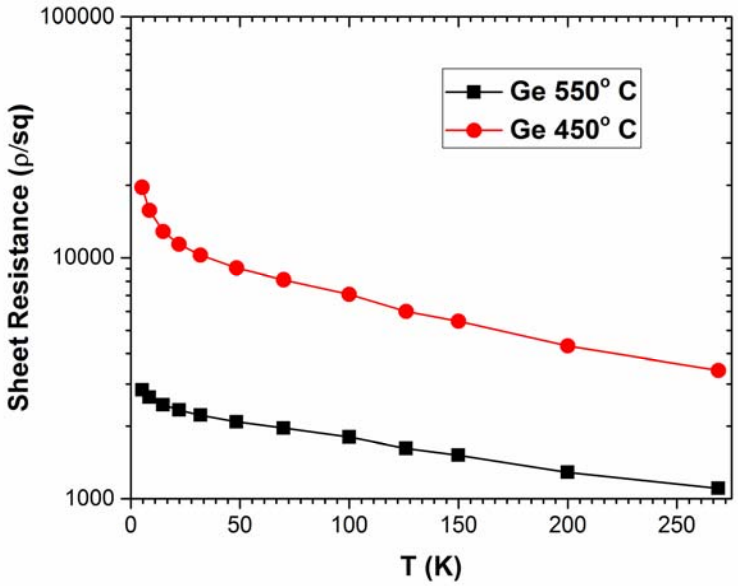

FIGURE 3.36. Sheet resistance of the UFPLD Ge nanoparticle thin films deposited with a fluence of 98 J/cm^2 at substrate temperatures of 450^o and 550^o C

Figures 3.35 and 3.36 show the carrier density and sheet resistance. As expected, the carrier density increases with increasing temperature and the sheet resistance decreases with increasing temperature.

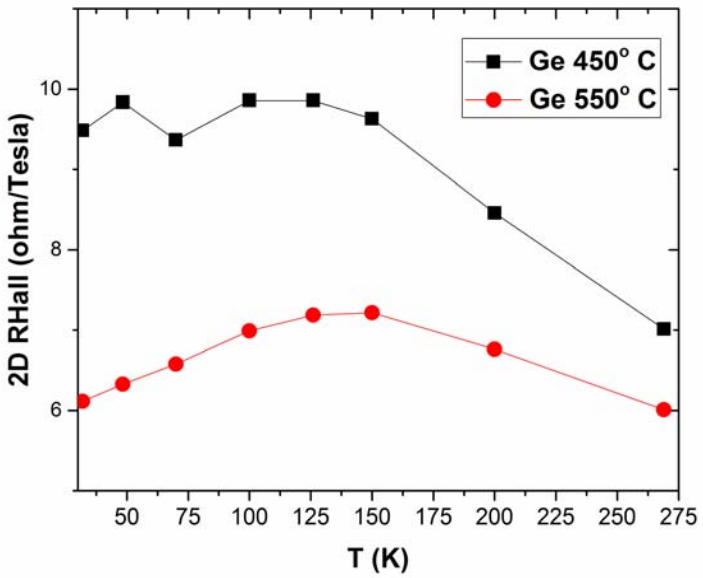

FIGURE 3.37. Two dimensional Hall coefficients of the UFPLD Ge nanoparticle thin films deposited with a fluence of 98 J/cm^2 at substrate temperatures of 450^o and 550^o C

3.10 References

1. Oraiqat, I., J. Kennedy, J. Mathis, and R. Clarke, *Femtosecond laser deposition of semiconductor quantum dot films.* 2012: p. 402-417.

2. Amoruso, S., R. Bruzzese, N. Spinelli, R. Velotta, M. Vitiello, X. Wang, G. Ausanio, V. Iannotti, and L. Lanotte, *Generation of silicon nanoparticles via femtosecond laser ablation in vacuum.* Applied Physics Letters, 2004. **84**(22): p. 4502.

3. Amoruso, S., G. Ausanio, R. Bruzzese, L. Gragnaniello, L. Lanotte, M. Vitiello, and X. Wang, *Characterization of laser ablation of solid targets with near-infrared laser pulses of 100fs and 1ps duration.* Applied Surface Science, 2006. **252**(13): p. 4863-4870.

4. Ausanio, G., S. Amoruso, A.C. Barone, R. Bruzzese, V. Iannotti, L. Lanotte, and M. Vitiello, *Production of nanoparticles of different materials by means of ultrashort laser pulses.* Applied Surface Science, 2006. **252**(13): p. 4678-4684.

5. Perrière, J., C. Boulmer-Leborgne, R. Benzerga, and S. Tricot, *Nanoparticle formation by femtosecond laser ablation.* Journal of Physics D: Applied Physics, 2007. **40**(22): p. 7069-7076.

6. Fowles, G., *Introduction to Modern Optics*. 1975, New York: Holt, Rinehart and Winston.

7. Malitson, I.H., *Interspecimen Comparison of the Refractive Index of Fused Silica.* Journal of the Optical Society of America, 1965. **55**(10): p. 1205-1209.

8. *Gaussian Beam Optics*. 11/01/2015]; Available from: http://www.newport.com/Gaussian-Beam-Optics/144899/1033/content.aspx.

9. Kramida, A., Y. Ralchenko, and J. Reader, *NIST Atomic Spectra Database (ver. 5.3)*. 2015: National Institute of Standards and Technology.

10. Zhigilei, L.V., *Dynamics of the plume formation and parameters of the ejected clusters in short-pulse laser ablation.* Applied Physics A: Materials Science & Processing, 2003. **76**(3): p. 339-350.

11. *Semiconductors on NSM*. Available from: http://www.ioffe.rssi.ru/SVA/NSM/Semicond/.

12. Maeda, Y., N. Tsukamoto, Y. Yazawa, Y. Kanemitsu, and Y. Masumoto, *Visible photoluminescence of Ge microcrystals embedded in SiO2 glassy matrices.* Applied Physics Letters, 1991. **59**(24): p. 3168.

13. Hayashi, R., M. Yamamoto, K. Tsunetomo, K. Kohno, Y. Osaka, and H. Nasu, *Preparation and Properties of Ge Microcrystals Embedded in SiO2 Glass Films.* Japanese Journal of Applied Physics, 1990. **29**(4): p. 756-759.

14. Shklyaev, A.A. and M. Ichikawa, *Visible photoluminescence of Ge dots embedded in Si/SiO[sub 2] matrices.* Applied Physics Letters, 2002. **80**(8): p. 1432.

15. Hernández-Hernández, A., V.T. Rangel-Kuoppa, T. Plach, F. De Moure-Flores, J.G. Quiñones-Galván, J. Santoyo-Salazar, M. Zapata-Torres, L.A. Hernández-Hernández, and M. Meléndez-Lira, *Synthesis of visible light emitting self assembled Ge nanocrystals embedded within a SiO2 matrix.* Journal of Applied Physics, 2012. **111**(4): p. 044327.

16. Zi, J., K. Zhang, and X. Xie, *Comparison of Models for Raman Spectra of Si Nanocrystals.* Physical Review B, 1996. **55**(15): p. 9263-9266.

17. Richter, H., Z.P. Wang, and L. Ley, *The one phonon Raman spectrum in microcrystalline silicon.* Solid State Communications, 1981. **39**(5): p. 625-629.

18. Zi, J., H. Büscher, C. Falter, W. Ludwig, K. Zhang, and X. Xie, *Raman shifts in Si nanocrystals.* Applied Physics Letters, 1996. **69**(2): p. 200.

19. Vadavalli, S., S. Valligatla, B. Neelamraju, M.H. Dar, A. Chiasera, M. Ferrari, and N.R. Desai, *Optical properties of germanium nanoparticles synthesized by pulsed laser ablation in acetone.* Frontiers in Physics, 2014. **2**.

20. Elzinga, P., F. Lytle, Y. Jian, and G. Laurendeau, *Pump/Probe Spectroscopy by Asynchronous Optical Sampling.* Applied Spectroscopy, 1987. **41**(1): p. 2-4.

21. Stoica, V., Y.-M. Sheu, D. Reis, and R. Clarke, *Wideband Detection of Transient Solid-State Dynamics Using Ultrafast Fiber Lasers and Asynchronous Optical Sampling.* Optics Express, 2008. **16**(4).

22. Perrin, B., *Investigation of Short-Time Heat Transfer Effects by an Optical Pump–Probe Method*, in *Microscale and Nanoscale Heat Transfer*. 2007, Springer: Berlin.

23. Nakajima, M., K. Mizoguchi, K. Morita, K. Itoh, H. Harima, and S. Nakashima, *Comparison of coherent and incoherent LO phonons in isotopic 70 Ge/ 74 Ge Superlattices.* Journal of Luminescence, 2000. **87**(89): p. 942-944.

24. Konstantatos, G. and E.H. Sargent, *Nanostructured materials for photon detection.* Nat Nanotechnol, 2010. **5**(6): p. 391-400.

25. Moore, A.R., *Electron and hole drift mobility in amorphous silicon.* Applied Physics Letters, 1977. **31**(11): p. 762.

26. Jenny, D.A. and R.H. Bube, *Semiconducting Cadmium Telluride.* Physical Review, 1954. **96**(5): p. 1190-1191.

27. Li, Y., R.G. Clevenger, L. Jin, K.V. Kilway, and Z. Peng, *Unusually high SCLC hole mobility in solution-processed thin films of a polycyclic thiophene-based small-molecule semiconductor.* Journal of Materials Chemistry C, 2014. **2**(35): p. 7180.

CHAPTER 4

Ultrafast Laser Irradiated Graphite (ULIG)

4.1 Overview

This chapter covers experiments to study ultrafast laser effects on graphitic carbon synthesis with the motivation to synthesize graphene directly, using the ultrafast laser to exfoliate the weakly bonded layers of graphite. Previous work involving laser production of graphene includes a chemical step to reduce to the graphite into graphite oxide, following with a laser (or ultrafast laser) as means for photoexfoliation and photoreduction [1-3]. It has been proposed, and calculated, that an ultrafast laser may be able to directly photoexfoliate one graphene layer at a time, with pulses being on the order of 45 fs; longer pulses would ablate multi-layered graphene [4].

The first method that we studied was direct deposition using an ultrafast laser, with the same set up as used in chapter 3 for semiconductor nanoparticle thin films, except the target is replaced with a carbon target (pyrolytic graphite - Kurt Lesker part EJTPYRO501A4). The substrates used for nanoparticle collection are carbon coated copper-mesh TEM grids. All UFPLD experiments were carried out with the optics at best focus while keeping the substrates unheated (room temperature).

The next method we investigated for graphene production was directly laser scribing a film of graphite particles. The graphite used was a product called Aerodag G, which is used as a

spray-on graphite lubricant. The solvent is isopropanol and contains a thermoplastic binder. This technique involves an initial step of expanding the interplanar distance of graphite by using a chemical intercalating agent. The reasoning behind using particles is to speed up intercalation, since the distance ions must diffuse into the sample would be minimized. The differentiating factor compared to current methods of producing graphene is that the graphite is not completely oxidized into graphite oxide beforehand, as with using Hummer's method [5], with the laser being used to photoreduce and photexfoliate. Instead, an aqueous acid solution, with a 40:1 ratio of H_2SO_4 and 70 wt. % H_2NO_3, is used to intercalate the graphite for a short amount of time and the ultrafast laser is then used for photoexfoliation at the surface.

The third method we investigated used an ultrafast laser to irradiate the backside of a thin transparent substrate (a microscope coverslip) to transfer material onto a receiving substrate (silicon wafer) [6]. The laser is again focused as a line, at various fluences, on the back of the substrate to offer a swath of material transfer. The film was a layer of Aerodag G, which was allowed to air dry.

4.2 Ultrafast Pulsed Laser Deposition with a Graphite Target

Referring to figure 4.1, the only particles seen in the TEM micrograph were graphitic and no other particles are seen when the laser ablation is performed at a fluence of 3.94 J/cm^2 and an intensity of 2.62 x 10^{13} W/cm^2. This method preferentially produces amorphous carbon.

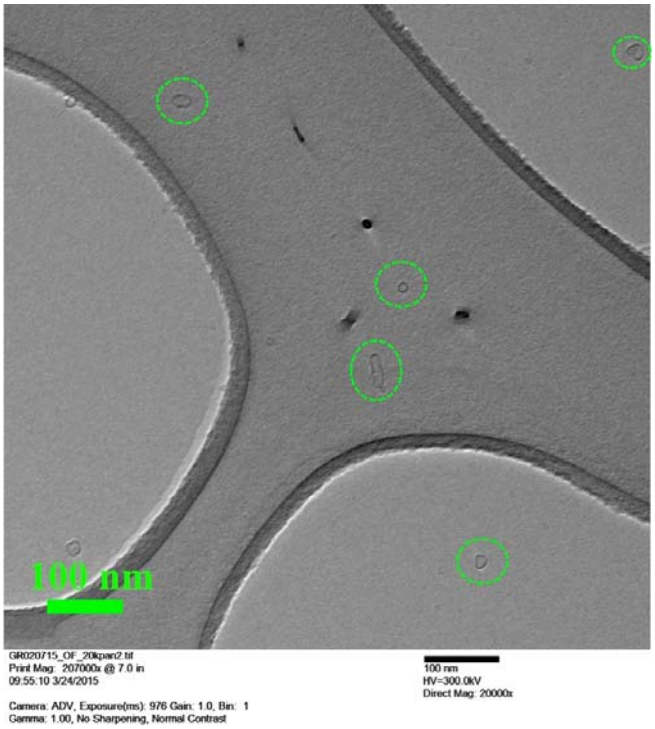

FIGURE 4.1. TEM micrograph of UFPLD graphite, some of the graphitic structures are circled in green

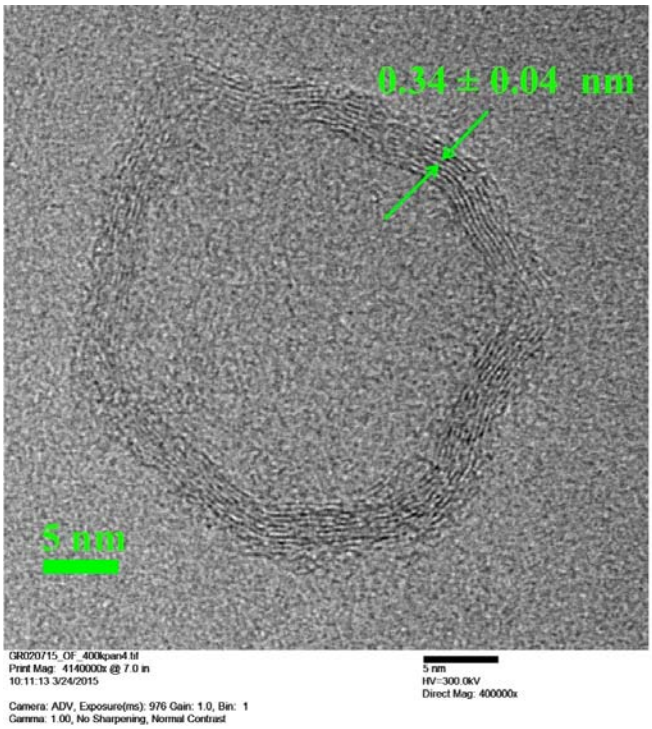

FIGURE 4.2. Zoomed-in TEM micrograph of one of the UFPLD grown graphitic structures are circled in green showing an interplanar distance of 0.34 ± 0.04 nm

Judging by their dark appearance, the TEM grids appeared to be coated but nothing was visible in the TEM. Since the TEM grids are coated with an amorphous carbon film, there was zero contrast, pointing to amorphous carbon coming from the laser ablation plume. When the focusing lens was pulled 4.5 cm out of focus (giving a fluence of 0.57 J/cm^2), the spectrum looked predominately continuous, as seen in figure 4.3. The objects produced at these conditions are what appear to be annular graphitic structures. It is possible that these objects are spherical and only the edges can be seen since the electron beam travels through more carbon at the edges of the projected circle looking down at it. The measured interplanar spacing is 0.34 ± 0.04 nm, comparable to the literature value of 0.335 nm, [7] verifying the objects in figure 4.1 and 4.2 are graphitic carbon nanostructures.

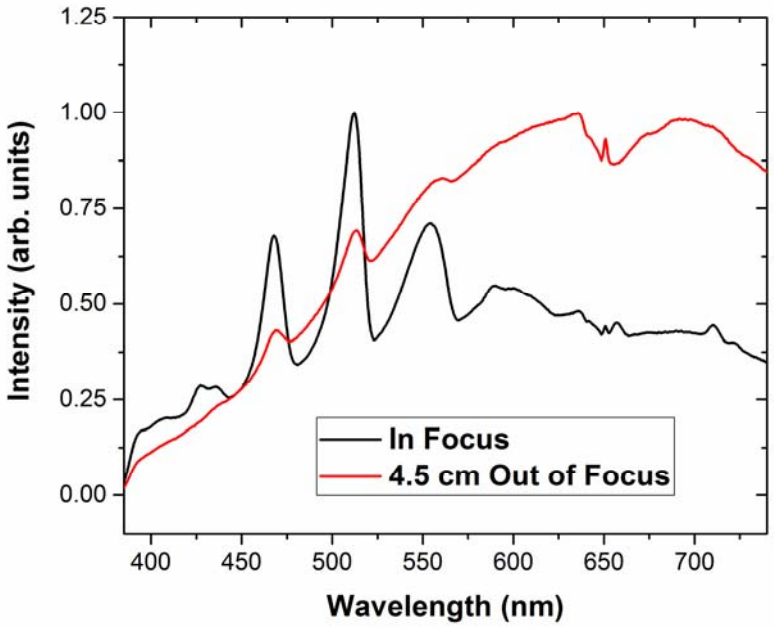

FIGURE 4.3. Ultrafast laser ablation plume spectra of the laser at best focus, a fluence of 3.94 J/cm^2 (black line) and 4.5 cm out of focus, 0.57 J/cm^2 (red line). Most of the observed atomic emission lines correspond to carbon and are tabulated in the table below.

Measured C Peak Position (nm)	Ionic Species NIST	Tabulated Values (nm) NIST
427.4	C(II)	426.726
435.6	C(III)	432.556
467.8	C(III)	466.586
512.2	C(II)	513.294
554.2	-	-
589.8	C(II)	589.159
600.2	C(I)	600.113
657.0	C(II)	657.805
710.2	C(I)	711.318

TABLE 4.1. Measured peak positions of the carbon plume at best focus compared to tabulated values and corresponding emission data from NIST.

Note that one of the peaks, 554.2 nm, from the graphite plume cannot be accounted for, comparing with atomic emission lines from NIST [8]. Looking deeper at the NIST tables, there are other materials that can match some of the atomic emission lines in figure 4.3, such as tungsten, yttrium, and sulfur, except that the resultant ablation products are graphitic and no other nanoparticles of the various materials are found. The ablation target is guaranteed to be 99.999% pure (by the Kurt Lesker Company). There are two models of targets, one unbonded (which was purchased for this experiment) and the other bonded with indium, even if the bonded target was sent by mistake, there are no indium tabulated emission peaks that would closely correspond with the measured spectrum.

One hypothesis is that within the plume (the spectrum is an image of the plume at the target surface), nano-diamond phases are produced at or near the target surface and the 512.2 nm (2.421 eV) peak is photoluminescence (PL) from those diamond phases. Previous work has identified this peak in both natural diamond and Chemical Vapor Deposition (CVD) grown artificial diamond [9, 10]. Though the PL peak is at a higher energy than the laser wavelength (780 nm), multiphoton excitation can occur due to the high intensity of the ultrafast laser. This

type of multiphoton excitation has been seen to excite PL in nanodiamonds with a laser wavelength of 1064 nm and a pulse duration of 10 ns [11].

4.3 Ultrafast Laser Irradiated Graphite (ULIG) - Direct Laser Scribing

The following samples were prepared by spraying Aerodag graphite spray onto glass microscope slides and then letting them air dry for one hour. A solution of nitric acid (HNO_3) added to sulfuric acid (H_2SO_4) with a ratio of 1:40 was used as an intercalating agent. The samples were dipped into a beaker for two seconds followed by a deionized water bath; any exposure longer than three seconds removed the Aerodag from the microscope slide. The samples were allowed to air dry for 24 hours. The sample is placed on a translation stage with a fixed-focus cylindrical lens allowing for a swath of laser energy to be scanned across the sample. All laser scans were done at a translation speed of 0.1 mm/s with a laser repetition rate of 1 kHz. A single sample was used for figures 4.4 – 4.9 with different regions on the same sample irradiated at different fluences. Figure 4.4 is an SEM micrograph showing a region where there is no laser irradiation at two image scales (magnification of x20k and x65k), providing a baseline for comparison.

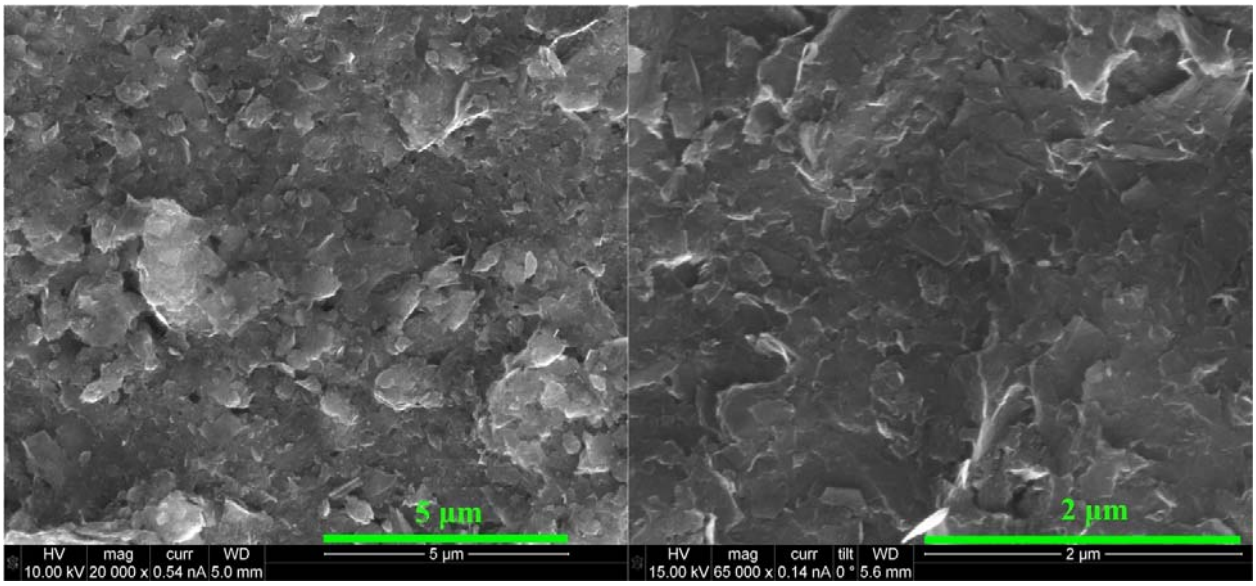

FIGURE 4.4. SEM micrograph of Aerodag graphite spray with no laser treatment.

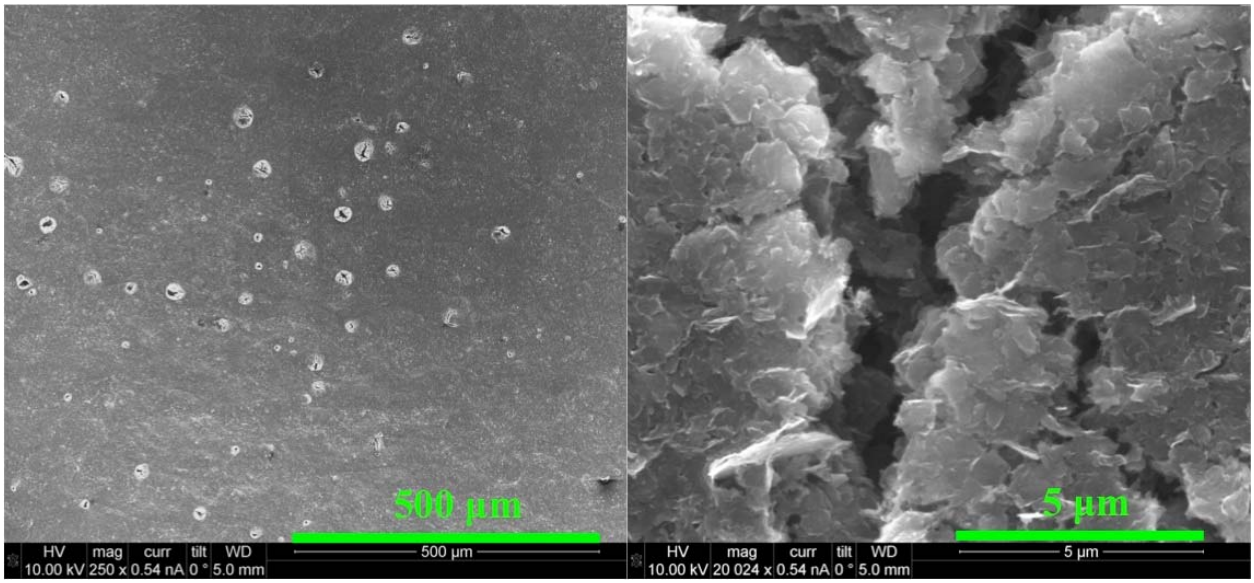

FIGURE 4.5. SEM micrograph of Aerodag graphite spray treated with H_2SO_4/HNO_3 and scanned/irradiated at a fluence of 10 mJ/cm^2, showing blistering (left) and a zoomed-in view of the formed blister (right)

Figure 4.5 is an SEM micrograph of the sample irradiated at 10 mJ/cm^2. Here blistering of the film is evident. This blistering is from trapped gasses that are being heated and explosively emitted. Figures 4.6 and 4.7 are SEM images of samples irradiated at fluences of 14.3 and 21.4

mJ/cm^2 and show similar blistering features as the sample in figure 4.5 except with greater frequency. However, the blistering frequency appears to be the same for these two fluences (see figures 4.6 and 4.7).

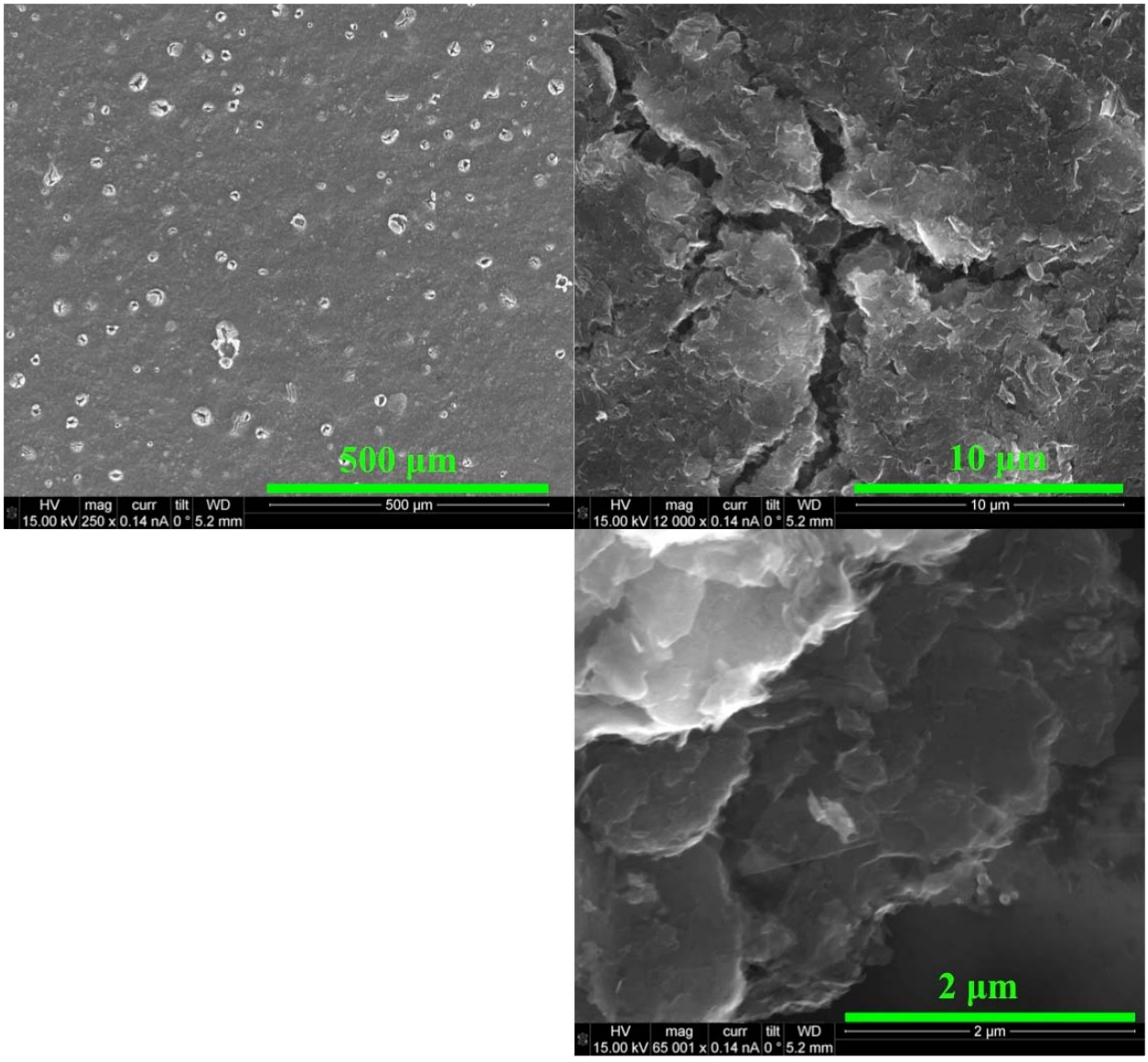

FIGURE 4.6. SEM micrograph Aerodag graphite spray treated with H_2SO_4/HNO_3 and scanned/irradiated at a fluence of 14.3 mJ/cm^2, showing blistering (left); a zoomed-in view of the formed blister (right), and inside edge of the blister (bottom right)

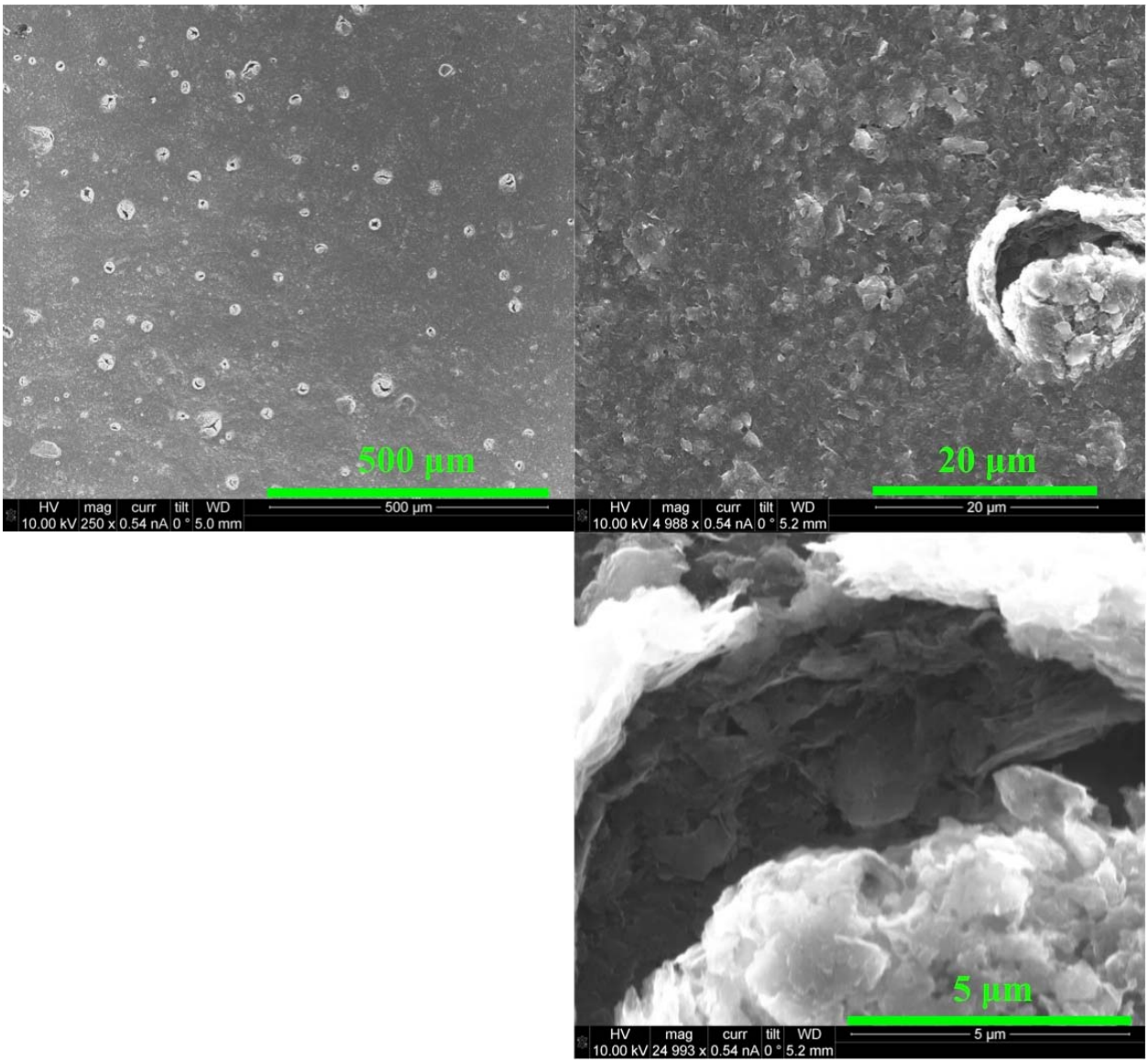

FIGURE 4.7. SEM micrograph of Aerodag graphite spray treated with H_2SO_4/HNO_3 and scanned/irradiated at a fluence of 21.4 mJ/cm^2, showing blistering (left); a zoomed-in view of the formed blister (right), and inside edge of the blister (bottom right).

The samples irradiated with a fluence of 42.9 and 85.7 mJ/cm^2 have dramatically different morphologies, as seen in figures 4.8 and 4.9. At a lower magnification, the overall structures are filamentary. Once zoomed-in, there are features that appear to be semi-transparent sheets and bright lines, which can be attributed to graphene-like structures. The bright line-like objects are thin layers of graphite (or graphene) sheets being viewed edge on, and the sheets of

graphite may become semi-transparent to 15 keV electrons as they get thinner, approaching a few layers of graphene.

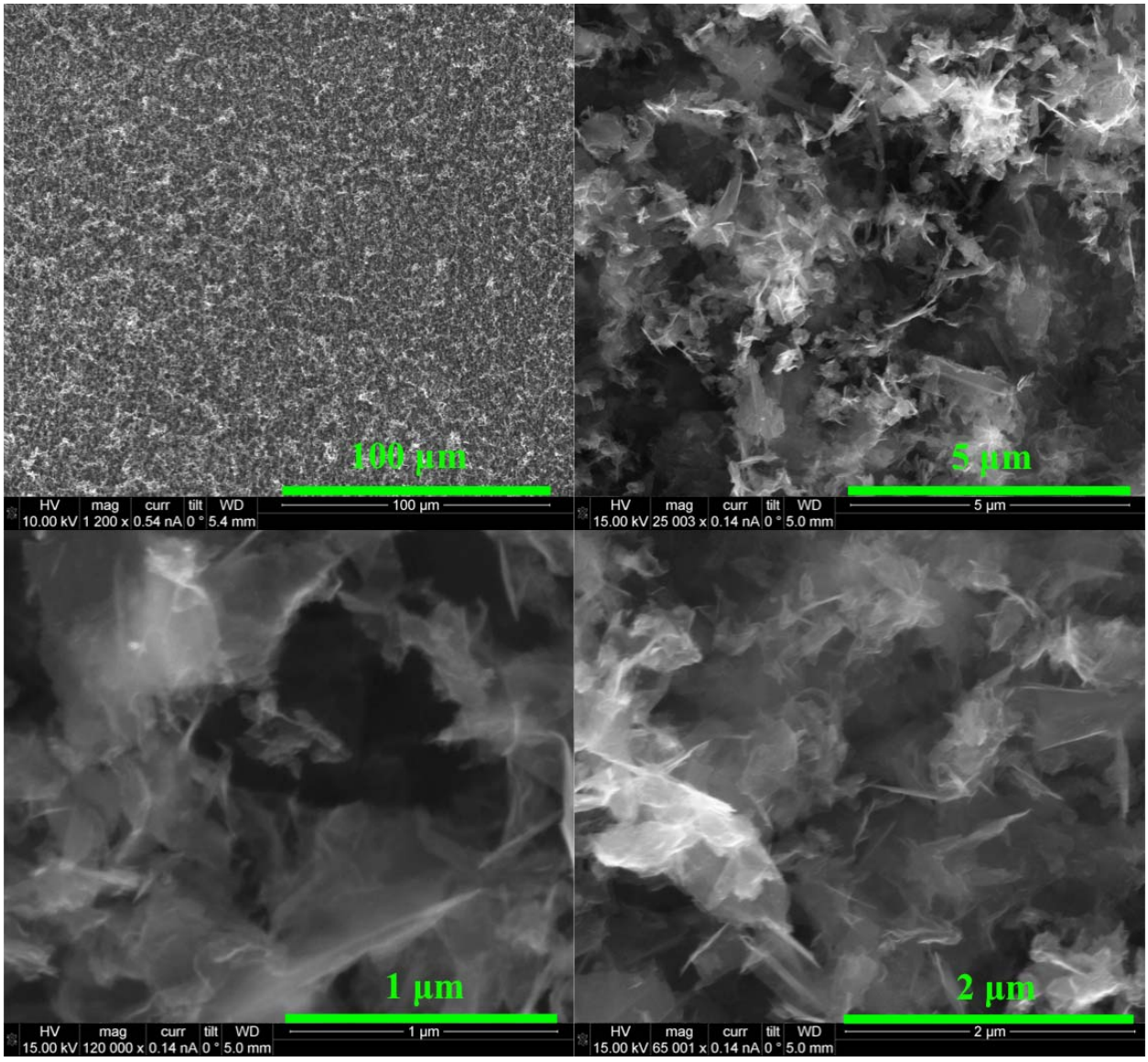

FIGURE 4.8. SEM micrograph of Aerodag graphite spray treated with H_2SO_4/HNO_3 and scanned/irradiated at a fluence of 42.9 mJ/cm^2, showing the morphology at various, increasing image scales (clockwise from the top left)

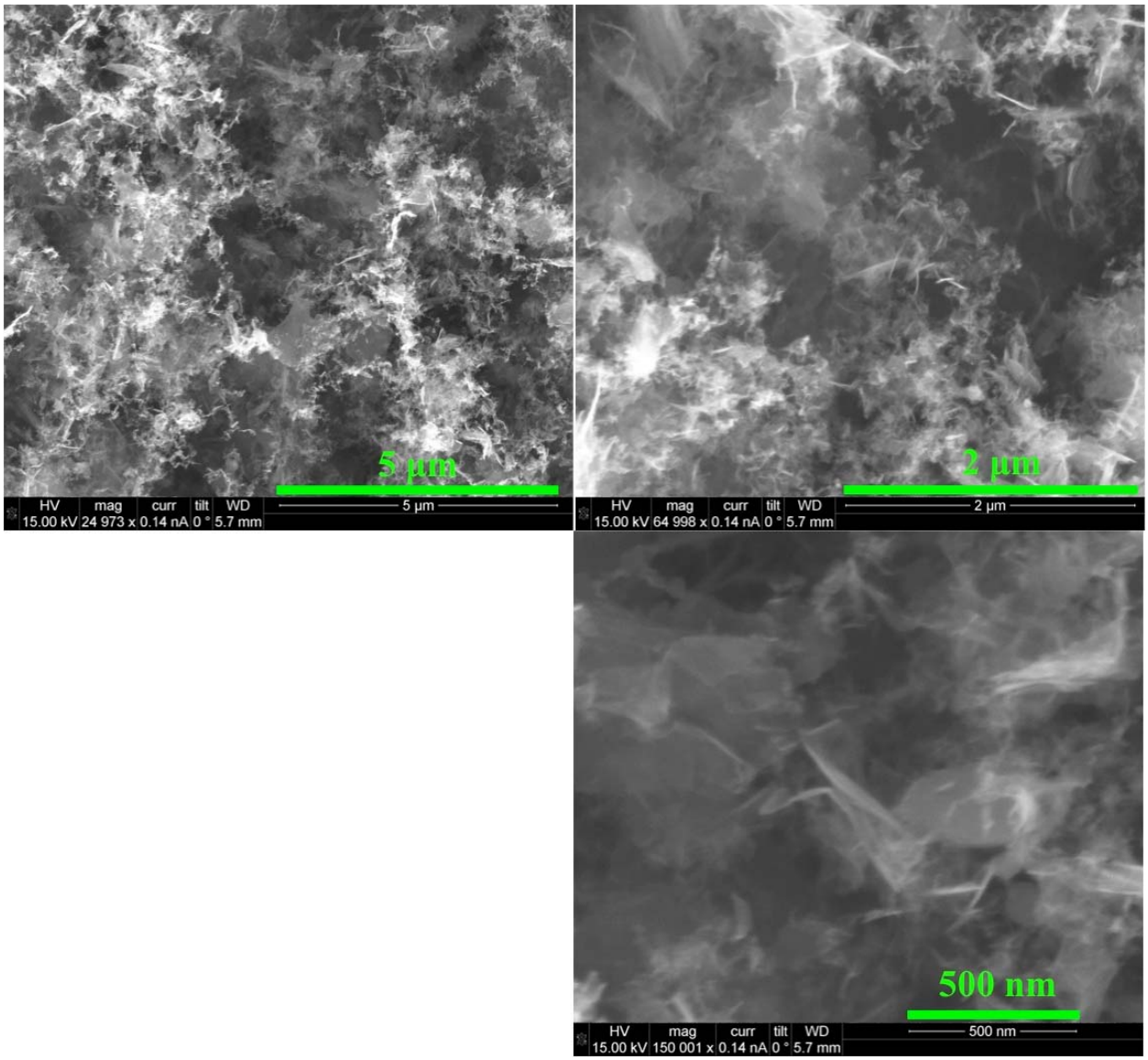

FIGURE 4.9. SEM micrograph of Aerodag graphite spray treated with H_2SO_4/HNO_3 and scanned/irradiated at a fluence of 85.7 mJ/cm^2, showing the morphology at various, increasing image scales (clockwise from the top left)

Fluences higher than those used to prepare the samples shown in figure 4.9 resulted in full ablation of the graphite film, removing all of the material from the substrate. Another trend noticed is the better quality "graphene film" that came from using the moderate fluence of 42.9 mJ/cm^2. This indicates there are different fluence regimes, a higher one that favors more filamentary structures and a lower one that produces more continuous sheet-like structures.

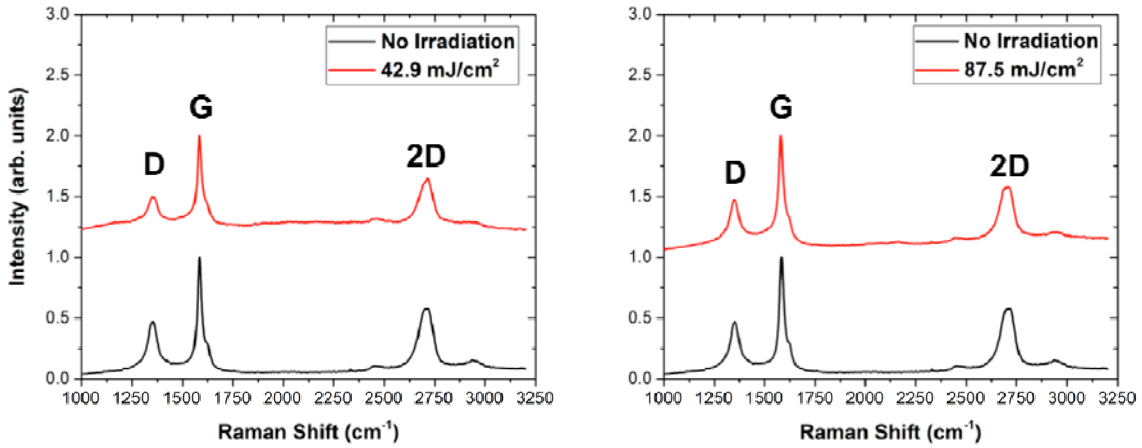

FIGURE 4.10. Raman spectrum comparing samples irradiated at (left) 42.9 mJ/cm^2 and (right) 87.5 mJ/cm^2 with the region experiencing no laser irradiation

The Raman spectra were collected at room temperature with a 532 nm excitation laser for the samples represented in figure 4.8 and 4.9. Each sample is compared to a region where there was no irradiation, to act as a standard for reference which is denoted by the black lines in figure 4.10. Three main peaks are visible, the D, G, and 2D peaks, which occur at around 1350, 1580, and 2700 cm^{-1}. The D band is known as the disorder band, which represents a ring breathing mode. In order to for this mode to be active, there must be adjacent defects in the carbon ring, thus this peak represents disorder in the sp^2 plane. If a sample were one continuous sheet of graphene or graphite with little defects, this peak would be very weak to non-existent. The samples irradiated as well as the control sample exhibit a strong D peak; this is because they are essentially made of graphite particles that are arranged in random orientations. In the case of the irradiated samples, graphite was further broken down into regions with graphene sheets in random orientations. The G band is an in-plane vibrational mode in the graphene sheets and is sensitive to the amount of graphitically bonded layers present. The 2D band is the second order of the D band, resulting from a two phonon lattice process, but is not activated by defects. The

intensity ratio between the 2D band and the G band, I_{2D}/I_G, can give an indication whether or not the sample is made of graphene. In a perfect single layer, the intensity of the 2D band is about a factor of two larger than the G band [12]. The irradiate samples had ratios very similar to the control sample: I_{2D}/I_G(control) = 0.565, I_{2D}/I_G(42.9 mJ/cm^2) = 0.541, and I_{2D}/I_G(85.7 mJ/cm^2). This may be attributed to the amount of graphene is produced with respect to the rest of the graphite film. The material of interest may just be on the very surface while the excitation laser excites the material underneath as well, overwhelming the signal.

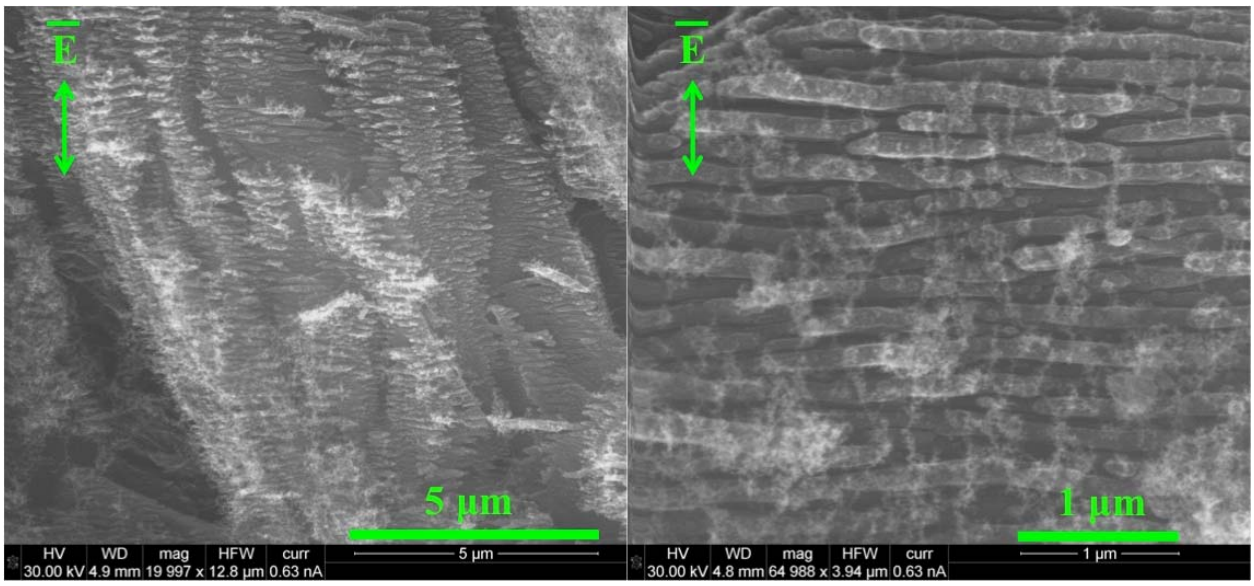

FIGURE 4.11. SEM micrograph of a commercial graphite electrode treated with H_2SO_4/HNO_3 and scanned/irradiated at a fluence of 50 mJ/cm^2, showing evidence of LIPS with a periodicity of 150 ± 22 nm and a width of 140 ± 16 nm

Figure 4.11 shows an SEM micrograph of a commercially made graphite electrode on copper foil, Styrene-Butadiene Rubber (SBR) and Carboxymethyl Cellulose (CMC) binder, and composite graphite (the exact composition information is unavailable due to its proprietary nature). The motivation in using a commercial electrode is to use a more robust system (compared to Aerodag G) to allow for a longer time in the intercalation solution. The initial sample, seen in figure 4.11, was exposed for the same amount of time in the intercalation

solution was the same as previous measurements in this chapter. The graphite particles in the SEM micrograph appear larger than those supplied with Aerodag G and as such appear not to break up but instead exhibit a periodic structure. The fluence was held to 50 mJ/cm^2 at 1 kHz and a scan speed of 0.1 mm/s. The observed laser induced periodic structure (LIPS) is measured to have a periodicity of 150 ± 22 nm and a width of 140 ± 16 nm with the laser polarization perpendicular to the LIPS direction. LIPS has been seen in previous work [13, 14] in various materials and has been seen with graphite using an 800 nm ultrafast Ti:Sapphire laser with 125 fs pulse duration and a repetition rate of 1 kHz (similar laser conditions to what is used in this thesis), giving a periodicity of 170 nm [15]. The conclusion from these measurements is that when using an ultrafast laser to irradiate graphite, it may be advantageous to use smaller particles since the particles can be exfoliated more easily (in the context of making graphene directly by scanning a graphite surface).

4.4 Irradiation from Rear of Graphite-Coated Glass

The next strategy to grow graphene from graphite nanoparticle films is to use an ultrafast laser to irradiate the side of the film opposite to the side facing the receiving substrate (the set up is explained in chapter 2), a graphene printing technique using ultrafast laser-induced forward transfer [6]. Instead of using a continuous thin film and a laser focal-spot, as with previous work, a film of graphite particles (Aerodag G) is coated on a thin piece of optically flat glass, a coverslip (0.13-0.16 mm thick) is irradiated by a focused laser line using cylindrical optics. The coverslip is held close to the substrate by using other coverslips as spacers. The substrate of choice is polished silicon due to its smoothness and conductivity (to prevent charging effects) during SEM imaging. With this technique, no chemical precursors are used. Scanning rates are held constant to 0.1 mm/s, with the only variable being fluence (85.7, 57.1, and 35.7 mJ/cm^2).

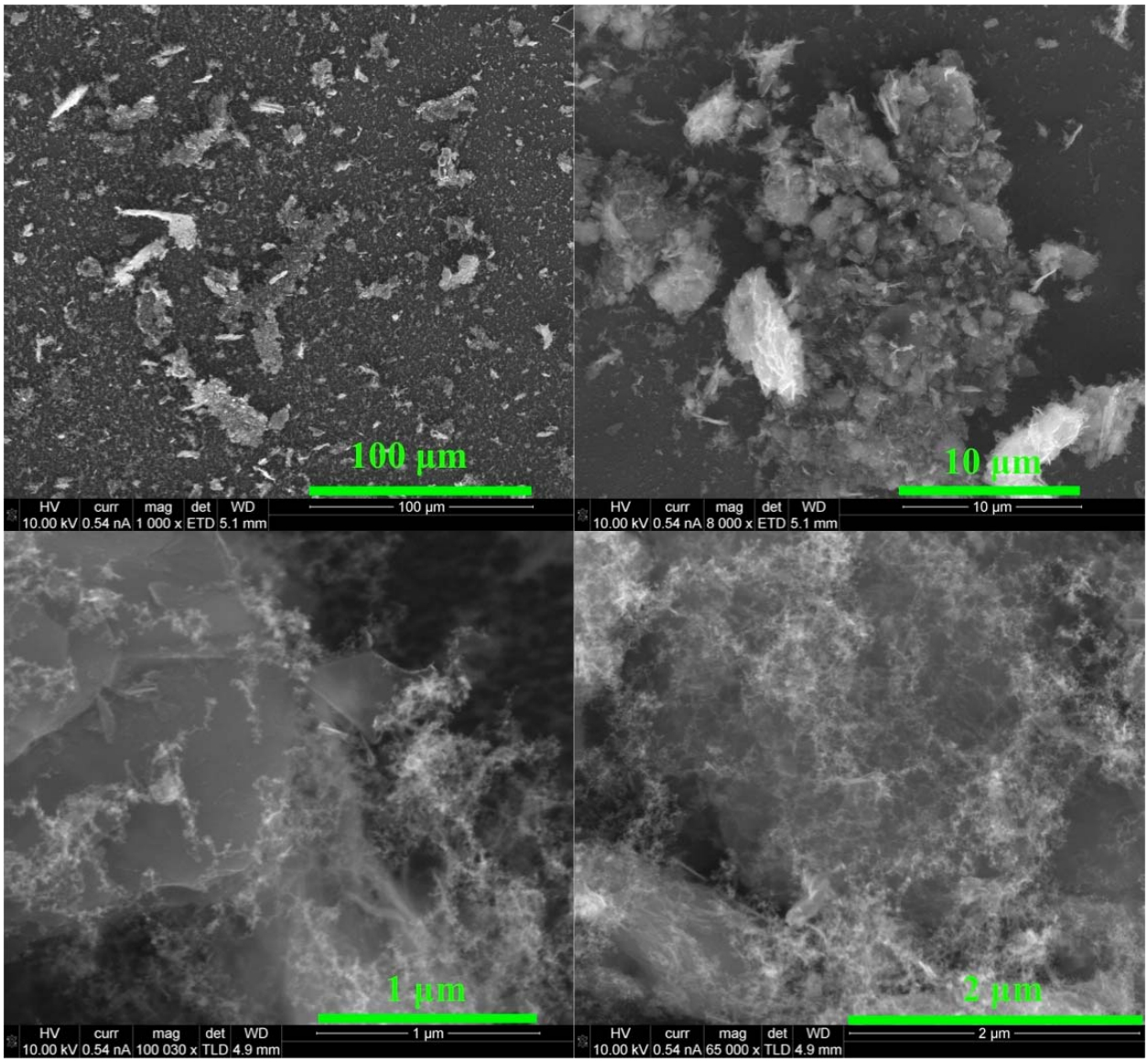

FIGURE 4.12. SEM micrograph of graphite deposited onto a silicon wafer from a coverslip that was coated with graphite and irradiated from behind at a fluence of 85.7 mJ/cm^2 (increasing image scale going clockwise from top left).

Figure 4.12 and 4.13 show the resultant structures deposited onto the silicon substrate at various image scales. The structures are similar to those from direct laser scribing (figure 4.8 and 4.9). Sheets on the order of almost a micron in lateral dimension are transparent to the electron beam are the main structural component, along with filamentary features. At the lower fluence of 57.1 mJ/cm^{2,} filament structure begins to disappear, leaving behind graphene sheets, sheet agglomerates, and graphite nanoparticles.

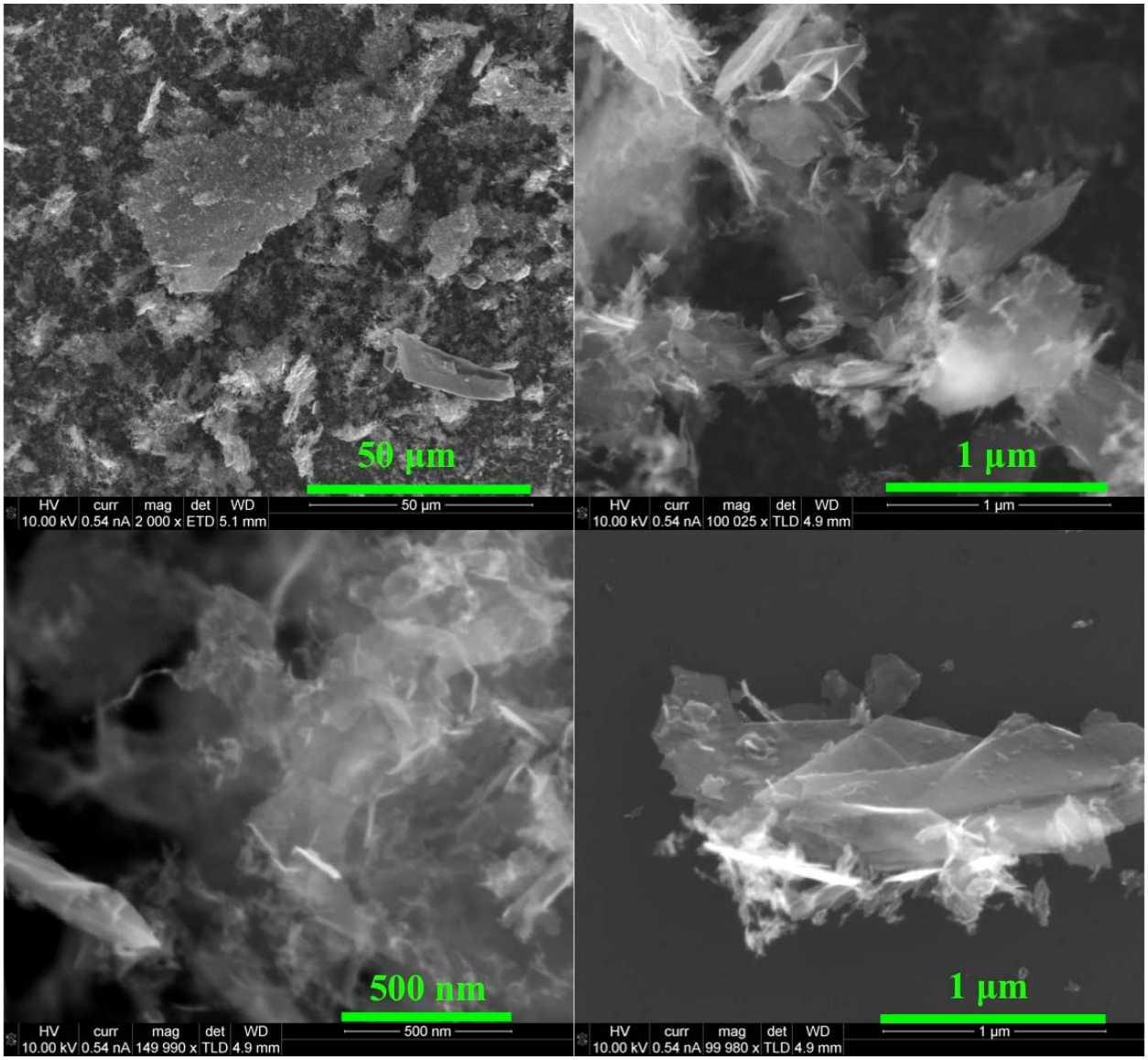

FIGURE 4.13. SEM micrograph of graphite deposited onto a silicon wafer from a coverslip that was coated with graphite and irradiated from behind at a fluence of 57.1 mJ/cm^2 (increasing image scale going clockwise from top left)

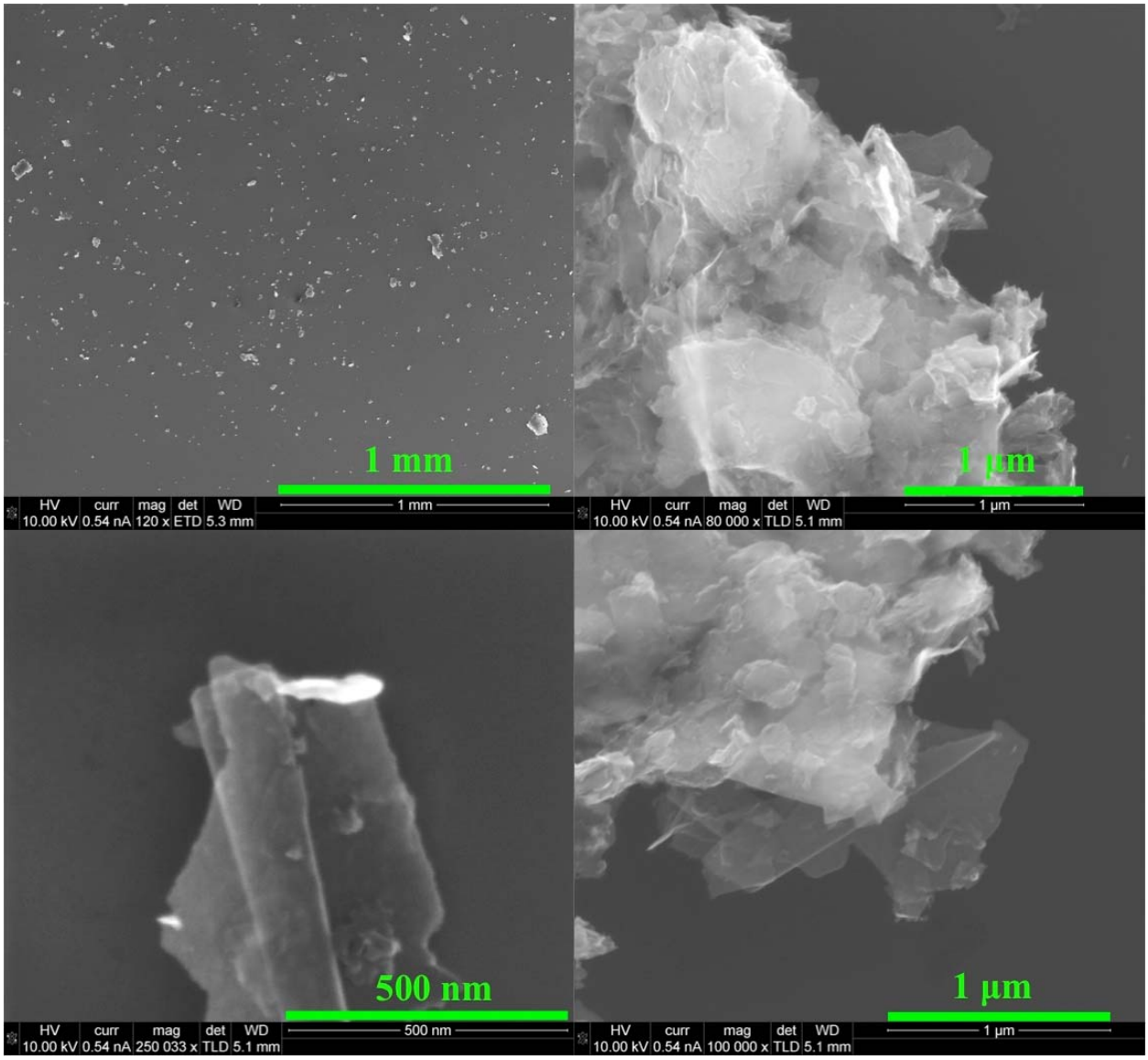

FIGURE 4.14. SEM micrograph of graphite deposited onto a silicon wafer from a coverslip that was coated with graphite and irradiated from behind at a fluence of 35.7 mJ/cm^2 (increasing image scale going clockwise from top left)

When the sample shown in figure 4.14 was finished being prepared, visually there did not appear to be any material on the substrate. However, the SEM shows there are structures that were deposited, but they are very sparse. These were investigated at higher magnification and found to be sheets transparent to the electron beam (indicating graphene-like morphology). Filamentary structures were non-existent. These semi-transparent sheets may be graphene, as the

larger graphitic structures are opaque to the electron beam. As with the direct laser scribing, there is an optimal fluence for the larger sheet structures.

4.5 References

1. El-Kady, M.F., V. Strong, S. Dubin, and R.B. Kaner, *Laser Scribing of High-Performance and Flexible Graphene-Based Electrochemical Capacitors.* Science, 2012. **335**(6074): p. 1326-1330.

2. Trusovas, R., K. Ratautas, G. Račiukaitis, J. Barkauskas, I. Stankevičienė, G. Niaura, and R. Mažeikienė, *Reduction of graphite oxide to graphene with laser irradiation.* Carbon, 2013. **52**: p. 574-582.

3. Sokolov, D.A., K.R. Shepperd, and T.M. Orlando, *Formation of Graphene Features from Direct Laser-Induced Reduction of Graphite Oxide.* Journal of Physical Chemistry Letters, 2010. **1**(18): p. 2633-2636.

4. Miyamoto, Y., H. Zhang, and D. Tománek, *Photoexfoliation of Graphene from Graphite: An Ab Initio Study.* Physical Review Letters, 2010. **104**(20).

5. Hummer, W.S. and R.E. Offema, *Preparation of Graphitic Oxide* Journal of the American Chemical Society, 1958. **80**(6): p. 1339.

6. Murphy, R.D., M.J. Abere, K.J. Schrider, B. Torralva, and S.M. Yalisove, *Nanoparticle size and morphology control using ultrafast laser induced forward transfer of Ni thin films.* Applied Physics Letters, 2013. **103**(9): p. 093113.

7. Boehm, H.P., *Carbon Surface Chemistry*, in *Graphite and Precursors* P. Delhaes, Editor. 2001, Gordon and Breach Science Publishers p. 146.

8. Kramida, A., Y. Ralchenko, and J. Reader, *NIST Atomic Spectra Database (ver. 5.3)*. 2015: National Institute of Standards and Technology.

9. Lim, H., S. Park, H. Cheong, H.-M. Choi, and Y.C. Kim, *Photoluminescence of Natural Diamonds.* Journal of the Korean Physical Society, 2006. **48**(6): p. 1556-1559.

10. Wang, W., M.S. Hall, K.S. Moe, J. Tower, and T.M. Moses, *Latest-Generation CVD-Grown Synthetic Diamonds from Apollo Diamond Inc.* GEMS & GEMOLOGY, 2007. **43**(4): p. 294-312.

11. Glinka, Y.D., K.-W. Lin, H.-C. Chang, and S.H. Lin, *Multiphoton-Excited Luminescence from Diamond Nanoparticles.* The Journal of Physical Chemistry B, 1999. **103**: p. 4251-4263.

12. Wall, M., *The Raman Spectroscopy of Graphene and the Determination of Layer Thickness.* Thermoscientific Application Notes, 2011. **52252**.

13. Li, Y., V.A. Stoica, L. Endicott, G. Wang, H. Sun, K.P. Pipe, C. Uher, and R. Clarke, *Femtosecond laser-induced nanostructure formation in Sb2Te3.* Applied Physics Letters, 2011. **99**(12): p. 121903.

14. Bonse, J., J. Krüger, S. Höhm, and A. Rosenfeld, *Femtosecond laser-induced periodic surface structures.* Journal of Laser Applications, 2012. **24**(4): p. 042006.

15. Huang, M., F. Zhao, Y. Cheng, N. Xu, and Z. Xu, *Mechanisms of ultrafast laser-induced deep-subwavelength gratings on graphite and diamond.* Physical Review B, 2009. **79**(12).

CHAPTER 5

ULIG Application in Lead Acid Battery Cells

5.1 Overview

Lead acid batteries (PbA) are ubiquitous in the automotive sector and as fuel economy and emission standards become increasingly stringent, the technology in cars becomes more advanced in boosting efficiency while reducing emissions. Emerging technologies, such start-stop and microhybrid vehicles, place a heavy demand on current battery systems based on PbA chemistry [1-3]. One of the difficulties of PbA batteries is dynamic charge acceptance, or how well the battery charges at various states of charge (SoC) [4, 5]. Charging performance is emphasized because the level of aggressiveness of fuel saving performance of start-stop technology (where the engine shuts off when the vehicle comes to a stop) is limited to how quickly the battery recharges. Another feature that is used to improve fuel economy is regenerative braking, where the battery can experience pulses of large regenerative currents from braking. The battery must be able to accept this pulse without much energy waste. Inserting carbon additives into the negative electrode has shown to offer improvements in charging performance [6-9]. One architecture is to replace a portion of the negative plate of a PbA battery with a high surface area carbon in order to have an energy storage device that is a hybrid between a PbA battery and a lead oxide (PbO) asymmetrical supercapacitor [10, 11].

The first application of the Ultrafast Irradiated Graphite (ULIG) attempted is improving the charge acceptance of lead acid battery (PbA) battery cells. The cells used for testing are commercial lead acid batteries using an absorbent glass mat separator (AGM) with a capacity of 0.85 Ah at C/20 rate (42.5 mA), where the C rate refers to the current that fully charges/discharges a cell in one hour. The electrolyte is 1.265 s.g. sulfuric acid (commercial battery acid). The negative plates were half coated with carbon, as shown in figure 5.1. The carbons used were a graphite spray coating (Aerodag G) and ULIG, scanned at a rate of 0.1 mm/s with a fluence of 70 mJ/cm^2 using the same experimental set up used in chapter 4.

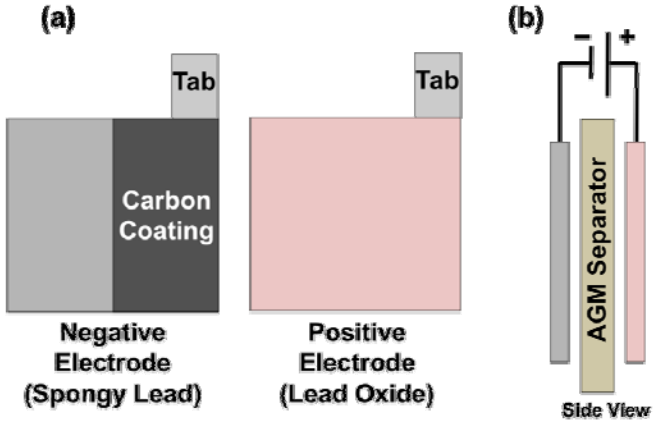

FIGURE 5.1. Schematic of the test cell (a) looking at the coating geometry on the negative plate and (b) a side view of the complete battery cell, consisting of the negative and positive plate with an AGM separator

There are two types of ULIG coatings denoted BULIG and CULIG. BULIG refers to half of the negative plate being coated with ULIG, as seen in figure 5.1, while CULIG refers to the entire surface of the negative electrode facing the separator being coated. The amount of graphite coated on each electrode is 15 ± 5 mg.

Once the cells are coated and assembled, they must go through an initial formation charge as outlined by the manufacturer in the following order (all steps are done with a constant current): charge for 18 hours at 170 mA, discharge for 3 hours at 144.5 mA; charge 2 hours at 85

mA, charge 9 hours at 170 mA, discharge for 3 hours at 212.5 mA; charge for 6 hours at 170 mA, and charge for 6 hours at 85 mA.

5.2 Lead Acid Test Cell Results

The following experiments are considered preliminary and offer motivation to engage in more thorough testing. The SoC is determined by first measuring the amount of charge each cell holds by discharging the cells at a slow constant current until a cutoff voltage is reached (1.75 V) from full charge. With the total charge known, the discharge current (while using the same current the capacity measurements were taken with) can be timed to discharge a certain amount of charge and the SoC is the fraction between how much charge is left (subtracting the total capacity by what is removed) and the total capacity; this is known as coulomb counting. This method is more accurate than using open circuit voltage (V_{oc}) since it can take a significant amount of time for the V_{oc} to equilibrate.

Figures 5.2-6 show a V-I plot (as opposed to I-V). These data are generated by applying a constant current for 20 s and measuring the voltage across the terminals (20 s is short enough to achieve constant voltage conditions). This is repeated for a multitude of currents (both charge and discharge) to generate the V-I plot. The resistance upon charging/discharging is measured from the slope of the linear regression.

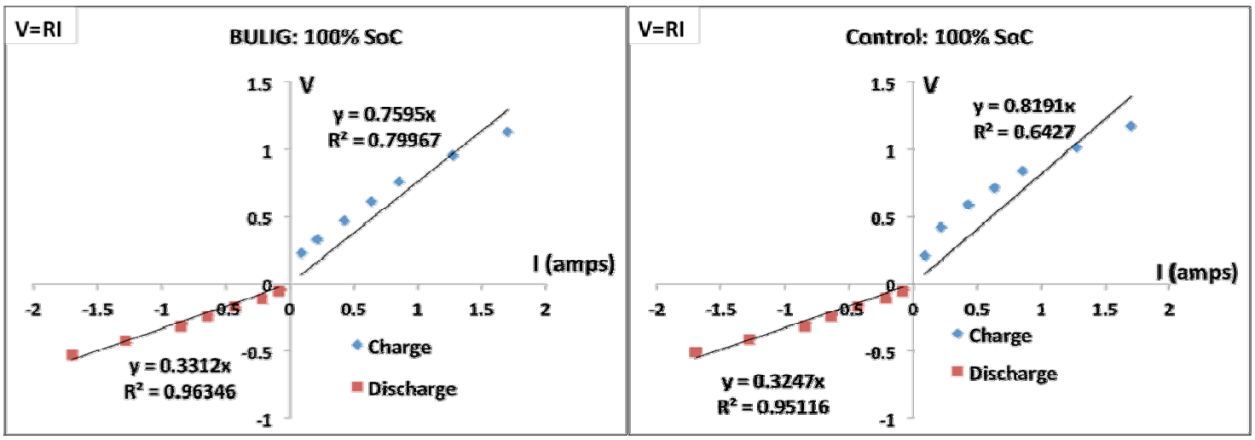

FIGURE 5.2. V-I plots of (left) BULIG PbA cell and (right) control PbA cell at 100% SoC

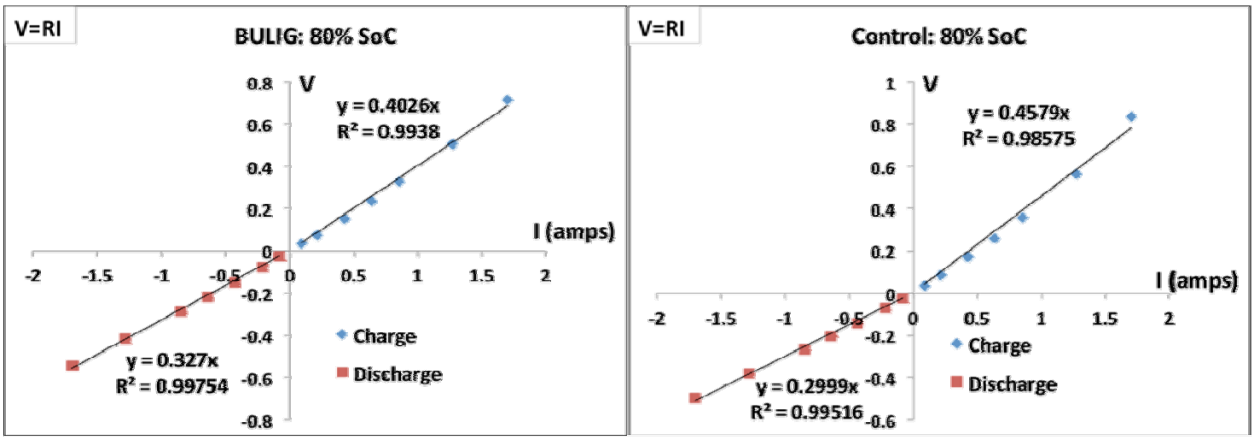

FIGURE 5.3. V-I plots of (left) BULIG PbA cell and (right) control PbA cell at 80% SoC

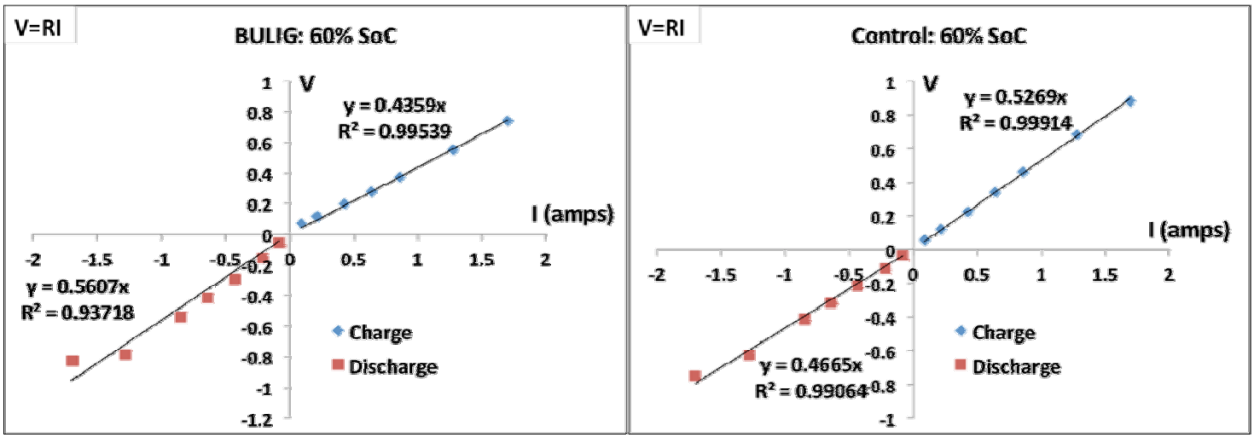

FIGURE 5.4. V-I plots of (left) BULIG PbA cell and (right) control PbA cell at 60% SoC

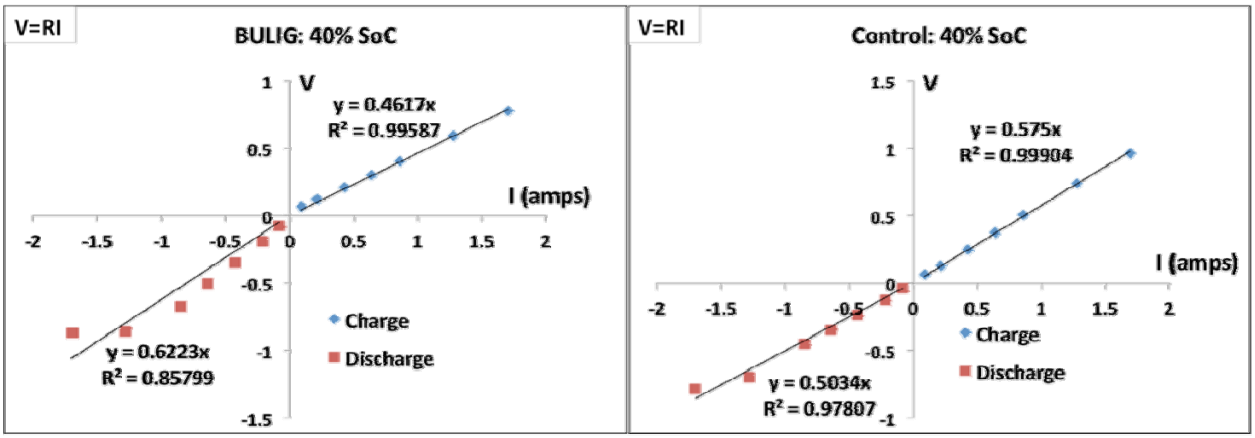

FIGURE 5.5. V-I plots of (left) BULIG PbA cell and (right) control PbA cell at 40% SoC

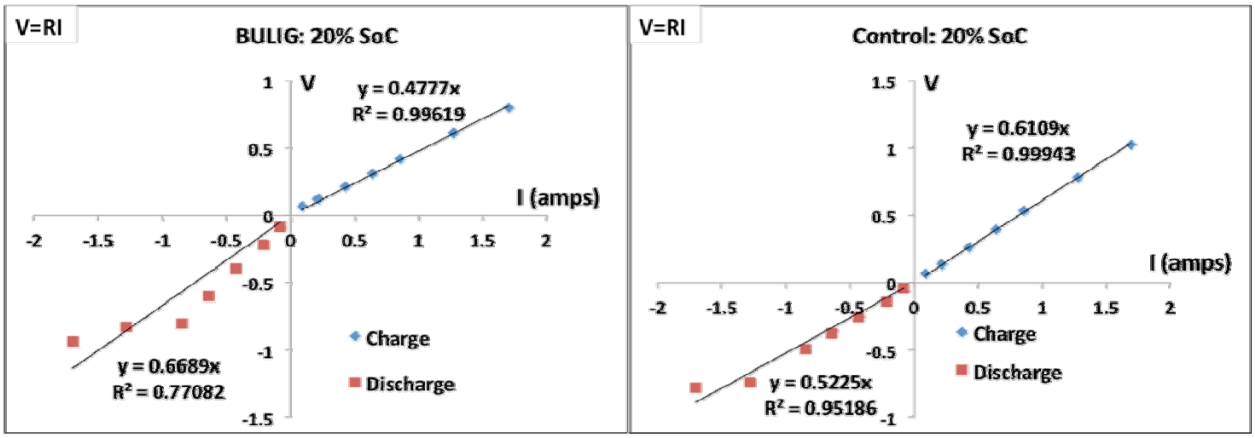

FIGURE 5.6. V-I plots of (left) BULIG PbA cell and (right) control PbA cell at 20% SoC

Typically for PbA, the resistance is lower on the discharge. BULIG coatings have been demonstrated to reduce the resistance on charging, as seen in figure 5.7. The highest resistance is at 100% SoC, which is to be expected since the there is little active material left on the electrodes. The lowest charge resistance appears at 80% SoC. Below 80% SoC, the resistance begins to increase, this is due to sulfation, where the sulfate crystals formed on the electrodes

become too big to easily undergo the reverse redox reaction back to lead and lead oxide. Here is where the gap between the Control and BULIG cell widen, indicating that this improvement may be due to capacitive effects of the ULIG coating.

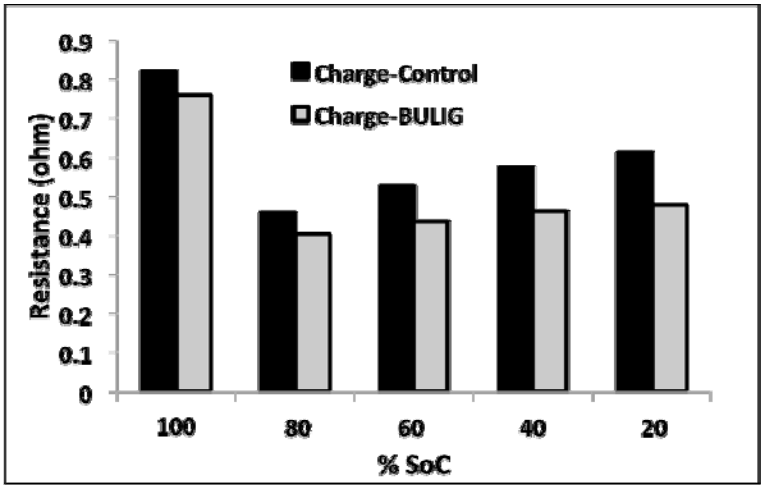

FIGURE 5.7. Comparison of the resistance upon charging between the BULIG and Control cells at various states of charge. The resistance is consistently lower in the coated electrodes.

The next set of battery tests involve fast constant current of 50mA charge/discharge cycles with no rest in between, as seen in figure 5.8, until the cell reaches failure, determined by and end of discharge (EoD) cut off voltage (1.75V). The cell starts at 100% SoC, this probes the charging efficiency of the cells. If the battery cell had perfect charging, it will go on forever since the amount of charge that is discharged is replaced by charging.

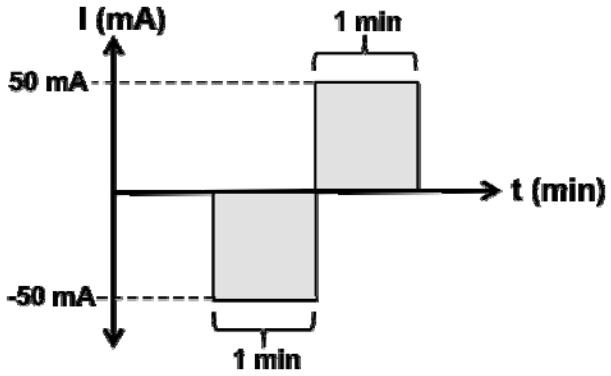

FIGURE 5.8. Test profile for fast charge/discharge, initiated by a one-minute constant current discharge at 50 mA, followed by a constant current charge of 50 mA, this is cycled until the EoD (End of Discharge) voltage reaches the cutoff of 1.75V

Figure 5.9 shows the result of this charge/discharge test with the ULIG coated electrode outperforming both the control and graphite coated cells. The control cell went 6,377 cycles, the graphite coated cell went 7,606, and the ULIG coated cells lasted 10,402 cycles before failure.

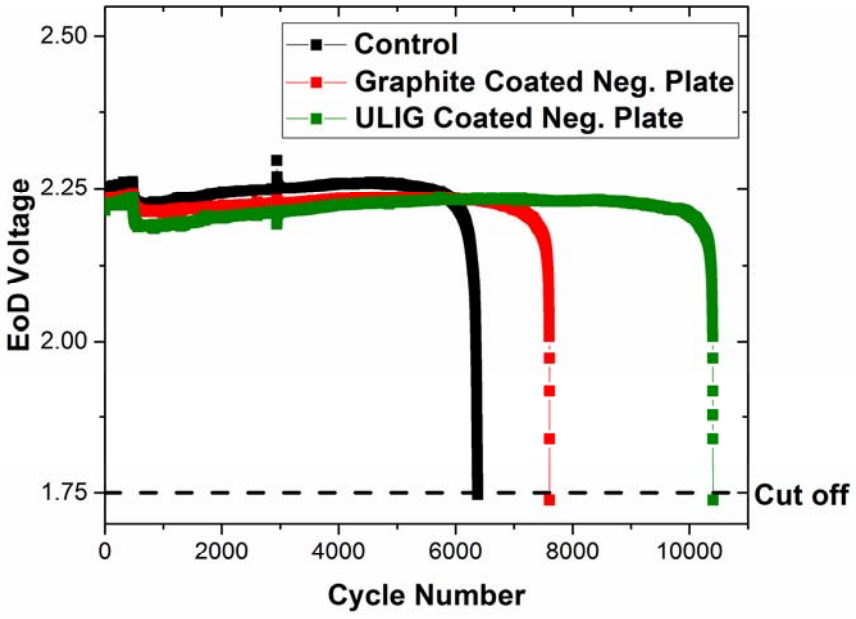

FIGURE 5.9. EoD versus cycle number, the Control cell reached failure first, followed by the graphite coated electrode, the ULIG coated cell outperformed the other cells by a factor of 1.6

Figures 5.10 and 5.11 show discharge plots for the following cells, again cells denoted with the letter "B" have half the plate negative plate coated and those with "C" have one entire side facing the counter electrode coated: control, BULIG, BG (Aerodag G graphite spray), CULIG, and CG. All resultant specific capacities reported from the discharge plots are mAh/g. Figure 5.10 is a study of capacity change as a function of discharge rates, each cell is charged at a constant current of 85 mA until 2.45 V is reached, followed by a constant voltage charge of 2.5 V until the charging current drops to 10 mA. Then the cell is discharged at various rates until a cut off voltage of 1.75 V is reached. In this testing configuration, the graphite coatings had slightly larger overall capacities compared to ULIG and the control.

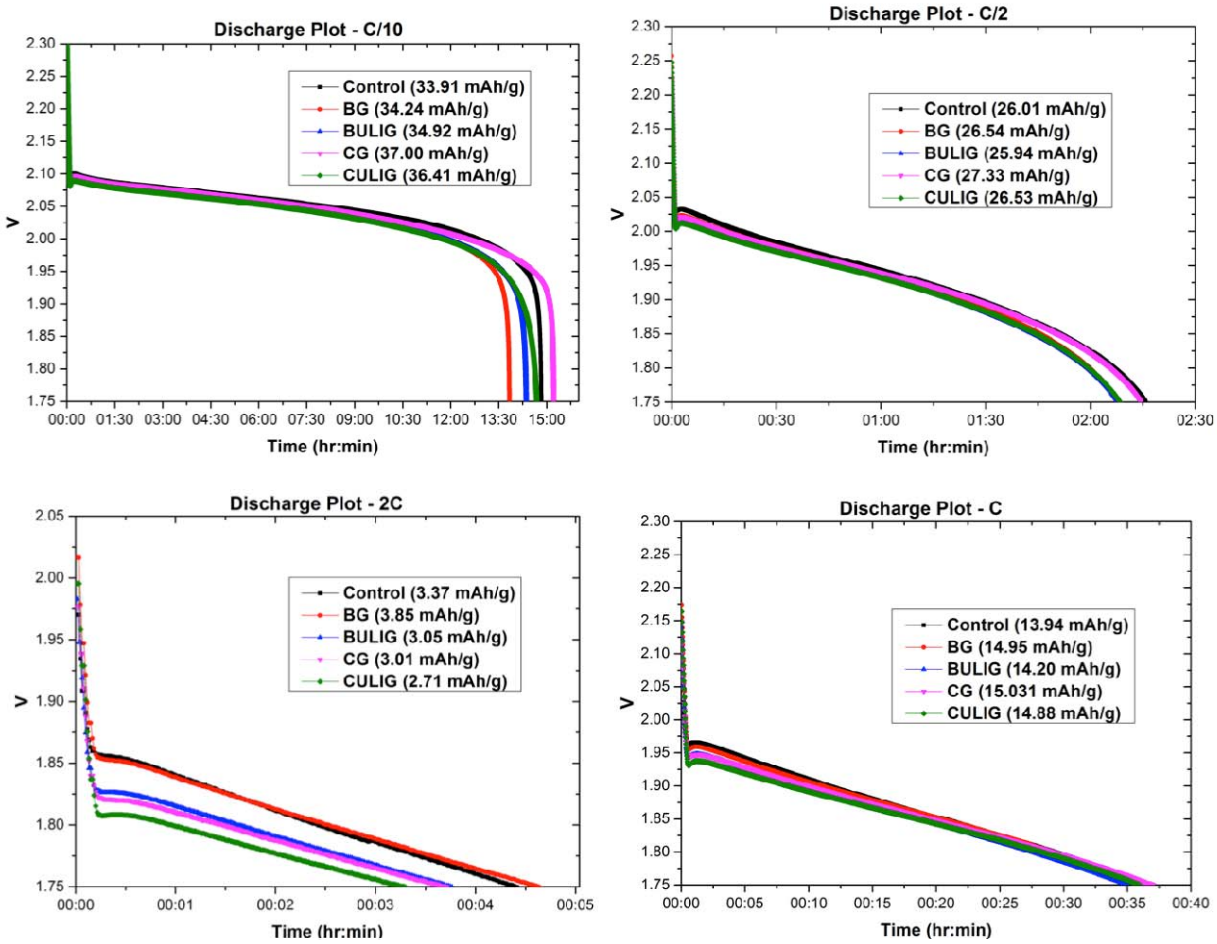

FIGURE 5.10. Discharge plots at various rates (increasing clockwise from the top left) of 85 mA, 425 mA, 850 mA, and 1,700 mA all charged with the same conditions

What figure 10 is showing is how the cell voltage changes with respect to time, with the legend listing out the measured cell capacities. The longer the cell takes to reach its cut off voltage for any given discharge current, the more capacity it has.

Figure 5.11 is a study of how the constant current charge rate affects the cell capacity. Each cell is charged at a constant current at various rates until 2.45 V is reached followed by a constant current discharge rate of 85 mA, which is held constant for all battery cells. The specific capacity decreases with increasing charging rate (listed in the legend), measured by the discharge time, at all charging rates: BULIG consistently had higher capacities at the end of the discharge cycle, indicating better charging performance.

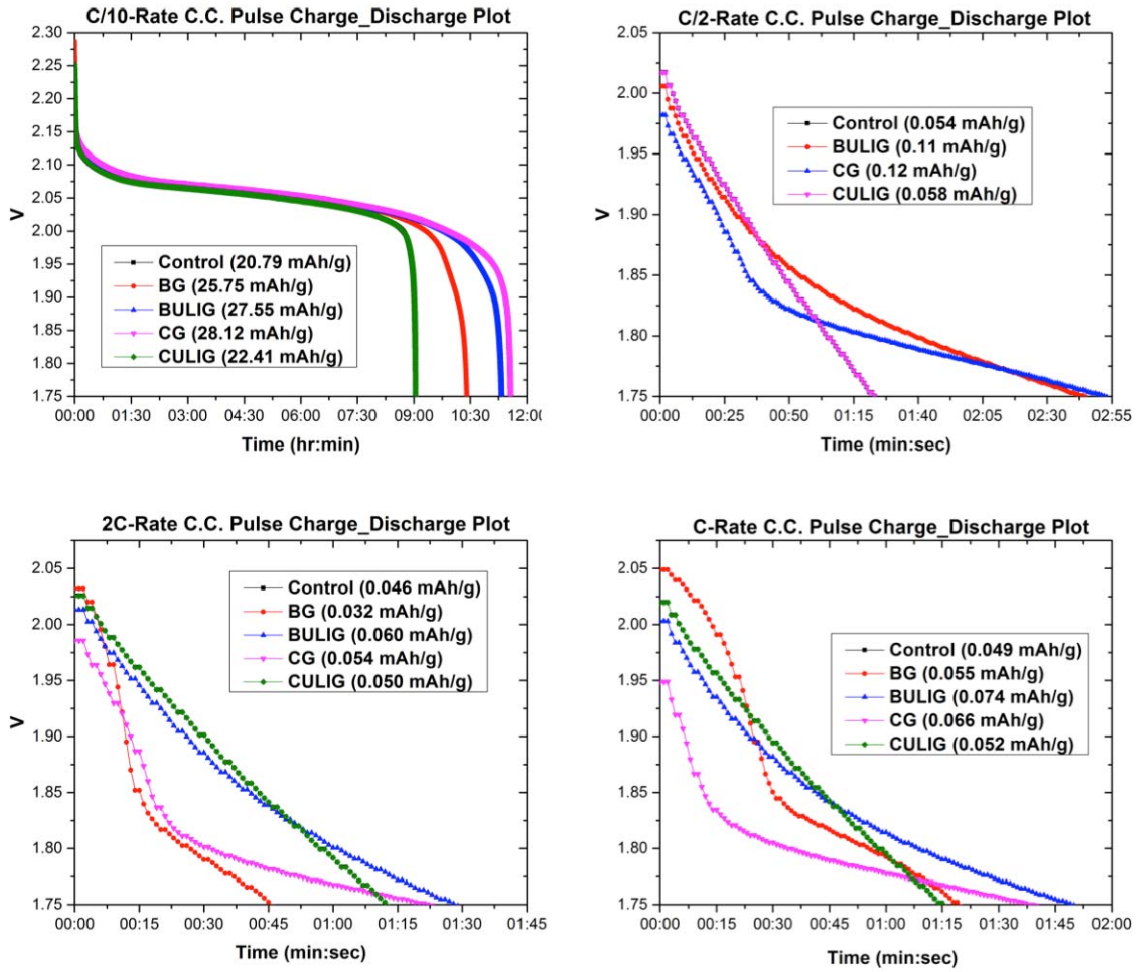

FIGURE 5.11. Discharge plots at a constant discharge current of 85 mA, charged at different constant current rates until 2.45V is reached (increasing clockwise from the top left) of 85 mA, 425 mA, 850 mA, and 1,700 mA

These series of battery tests show the ULIG coating on the negative plate improves the charging performance of the test cells. The first set of results demonstrates the decrease of battery cell resistance upon charging with the use of ULIG. The second test demonstrates superior charge efficiency and lifetime of ULIG coated cells compared to using untreated graphite coatings on the negative electrode and the control cell. The measurements in figure 5.11 show that as charge current increases, ULIG coated electrodes store more energy (23% more than the control at the 2C charge rate). The benefit of ULIG becomes increasingly apparent

as the charging current is increased, which addresses the main difficulty for utilizing the PbA chemistry for future demands.

5.3 References

1. Albers, J., E. Meissner, and S. Shirazi, *Lead-acid batteries in micro-hybrid vehicles.* Journal of Power Sources, 2011. **196**(8): p. 3993-4002.

2. Schaeck, S., et al., *Lead-acid batteries in micro-hybrid applications. Part II. Test proposal.* Journal of Power Sources, 2011. **196**(3): p. 1555-1560.

3. Arjun, A.K., et al., *Micro-Hybrid Power Systems – A Feasibility Study.* Journal of Clean Energy Technologies, 2013: p. 27-32.

4. Moseley, P.T. and D.A.J. Rand, *Partial State-of-Charge Duty: A Challenge but Not a Show-Stopper for Lead-Acid Batteries!*, in *Lead-Acid Batteries and Capacitors, New Designs, and New Applications*, K. Bullock, P.T. Moseley, and B.Y. Liaw, Editors. 2012. p. 3-16.

5. Nakamura, K., et al., *Failure modes of valve-regulated lead/acid batteries.* Journal of Power Sources, 1996. **59**(1-2): p. 153-157.

6. Bullock, K.R., *Carbon reactions and effects on valve-regulated lead-acid (VRLA) battery cycle life in high-rate, partial state-of-charge cycling.* Journal of Power Sources, 2010. **195**(14): p. 4513-4519.

7. Bača, P., et al., *Study of the influence of carbon on the negative lead-acid battery electrodes.* Journal of Power Sources, 2011. **196**(8): p. 3988-3992.

8. Calábek, M., et al., *Significance of carbon additive in negative lead-acid battery electrodes.* Journal of Power Sources, 2006. **158**(2): p. 864-867.

9. Shiomi, M., et al., *Effects of carbon in negative plates on cycle-life performance of valve-regulated lead/acid batteries.* Journal of Power Sources, 1997. **64**(1-2): p. 147-152.

10. Cooper, A., et al., *The UltraBattery—A new battery design for a new beginning in hybrid electric vehicle energy storage.* Journal of Power Sources, 2009. **188**(2): p. 642-649.

11. Lam, L.T. and R. Louey, *Development of ultra-battery for hybrid-electric vehicle applications.* Journal of Power Sources, 2006. **158**(2): p. 1140-1148.

CHAPTER 6

Conclusions and Future Work

We summarize here the main findings of this dissertation, the first detailed study of the application of ultrafast lasers to produce nanoparticles that can be useful for energy harvesting and storage. The importance of the work is its demonstration that the process of making nanoparticles with ultrafast lasers is extremely versatile and can be applied to practically any material, on any substrate. Moreover, the process is scalable to large areas: by scanning the laser with appropriate optics it is possible to coat square meters of materials (e.g., battery electrodes) quickly and inexpensively with nanoparticles. The following summarizes the main results from each part of the study, finally integrating them into an application of importance to advanced battery technology.

6.1 UFPLD of Semiconductor Films

We have shown that there is a fluence dependence on the nanoparticle size and the optical emission spectrum of the plume can be used predict a fluence that favors smaller nanoparticles. At smaller fluences, below around 0.57 J/cm^2, the ablation plume begins to have a continuous spectrum while at higher fluences the spectrum shows more of an atomic emission line character. The ablation plume with a continuous spectrum also showed a dramatic increase in nanoparticle throughput (almost 8x higher with Ge). The black-body spectral distribution reveals that the temperature of the plume is critical to whether the nanoparticles condensed from

the plume are liquid or solid on arrival at the substrate. XRD data shows there may be two separate types of particles, one that deposits as crystalline and the other deposits as amorphous, in which the amorphous character starts to disappear at substrate temperatures of over 250^{o} C due to annealing. This is attributed to molten material that quenches into an amorphous state upon hitting a cold substrate. This is seen at two different fluences (3.94 and 98 J/cm^2) with both ablation plume spectrums having atomic emission lines. This is verified with Raman spectroscopy, where the broad, diffuse peak on the left of the main peak disappears with increasing substrate temperature. It is also noticed that sintering takes place at the higher substrate temperatures, in SEM micrographs, fine structure disappears into the larger agglomerations of nanoparticles. This is verified by seeing reduced phonon confinement (reduced Raman peak shift) in Ge nanoparticles films deposited at higher substrate temperatures. Hall measurements verified that these types of nanoparticle films behave as a single thin film with carrier mobilities higher than other thin film technologies and orders of magnitude larger than colloidal quantum dot (QD) films. This material has promise for QD-based opto-electronics based on its mobility and purity of the process (UFPLD is done in UHV conditions).

Future work entails further characterization and new applications of UFPLD nanoparticle thin films:

- Quantify crystallinity at laser fluences where the ablation plume's spectrum is completely continuous with XRD
- Quantify surface recombination velocity
- Develop a method to encapsulate nanoparticles in flight from the target to the substrate to reduce non-radiative recombination sites and extract photoluminescence of the thin

films to quantify the effective E_g – this may effect the continuity of the thin film, reducing its mobility advantage

- Investigate multiexciton generation
- Test this material as a QD-based photodetector by depositing onto a metal substrate to build a Schottky diode and characterize it's performance
- Build a lithium ion anode by depositing silicon nanoparticles (silicon anodes have 10x the theoretical capacity compared to current graphite anodes) onto a metal current collector using UFPLD and investigate its cycle life (the main difficulty with Si anodes), power density, and energy density
- If the electrode performance is good, investigate integrating the UFPLD process into the thin-film battery synthesis process, where this technology would be most appropriate for

6.2 Ultrafast Laser Irradiated Graphite

This part of the thesis covered ultrafast laser material synthesis using a graphite precursor. The first set of experiments involved irradiating a graphite target using the UFPLD set up to collect material onto a TEM grid. At a high enough fluence (3.94 J/cm^2), amorphous carbon was produced with an unidentified emission peak at 512.2 nm. When the fluence was reduced (0.57 J/cm^2), annular graphitic nanostructures were produced, with the unknown emission peak still present, although at a greatly reduced intensity. The other part of the experiments focused on scanning an ultrafast laser over various regions on graphite particle films on glass, which were shown to produce both filamentary structures and sheets which are semi-transparent to the electron beam in SEM. These transparent sheets resemble layers of graphene that have been exfoliated. An ultrafast laser "printing" configuration was also identified by

coating a thin, transparent substrate with graphite particles and irradiating the back of the film for a forward transfer of material onto a receiving substrate. Future work consists of:

- Investigate and identify the source of 512.2 nm emission peak from the carbon ablation plume in UFPLD
- Investigate more compatible binder recipes where the sample can survive more than a few seconds in the intercalating solution before laser irradiation
- Investigate other graphitic precursors for ULIG, including using commercial expanded graphite to eliminate the intercalation step, reduce the process to just coating the substrate and irradiating.
- Extend Raman studies using an AFM/Raman system to gain Raman information from the small, graphene-like structures seen in the SEM to prevent the signal from being overwhelmed from material below and around these structures.
- Identify the mechanisms and conditions for graphene sheet production versus filament-like structures.
- Identify which nanostructure is more advantageous for energy storage.
- Investigate the link between the mechanism that causes LIPS and photoexfoliation using an ultrafast laser.
- Investigate depositing graphene by using a continuous film of graphite on the thin substrate for rear irradiation.
- Repeat experiments with an ultrafast laser with a shorter pulse duration of 45 fs.

6.3 ULIG Application for lead-acid battery cells

By coating carbon on half of the negative plate of a PbA cell, we demonstrated that the fast charging performance could be significantly improved compared to an uncoated battery cell (control). The types of carbons compared are graphite spray coating (Aerodag G) and ULIG. There is an increase in charging performance with ULIG over the graphite coating. This improvement is from the supercapacitive effects of the ULIG coating which caused the cell to act as both a battery and a supercapacitor. This is significant for PbA technology with the rise of various automobile fuel-saving technologies that puts more stress on its battery systems. By improving the charging capability of a PbA battery, it can be used in place of more expensive, less robust battery chemistries. Recommended future work consist of honing in on specific properties of using ULIG coatings to better understand its effects on energy storage:

- Perform a more fundamental study, characterize a supercapacitor made with ULIG using cyclic voltammetry, impedance spectroscopy, and charge/discharge cycling with various electrolytes
- Characterize an asymmetrical supercapacitor consisting of a lead oxide positive electrode and a ULIG negative electrode.
- Investigate possible physical mechanisms for why the end of discharge voltage suddenly falls below the cutoff voltage, as opposed to gradually, at cell failure. In particular, it would be interesting to model this behavior as a structural phase transition during the redox reaction.